The Astrophysical Journal, 936:92 (39pp), 2022 September 1 https://doi.org/10.3847/1538-4357/ac7f9d

Extragalactic Magnetism with SOFIA (SALSA Legacy Program). IV. Program Overview and First Results on the Polarization Fraction*

Enrique Lopez-Rodriguez[1], Sui Ann Mao[2], Rainer Beck[2], Alejandro S. Borlaff[3], Evangelia Ntormousi[4,5], Konstantinos Tassis[5,6], Daniel A. Dale[7], Julia Roman-Duval[8], Kandaswamy Subramanian[9], Sergio Martin-Alvarez[10], Pamela M. Marcum[3], Susan E. Clark[1], William T. Reach[11], Doyal A. Harper[12], and Ellen G. Zweibel[13,14]
[1] Kavli Institute for Particle Astrophysics & Cosmology (KIPAC), Stanford University, Stanford, CA 94305, USA; elopezrodriguez@stanford.edu
[2] Max-Planck-Institut für Radioastronomie, Auf dem Hügel 69, D-53121 Bonn, Germany
[3] NASA Ames Research Center, Moffett Field, CA 94035, USA
[4] Scuola Notmale Superiore di Pisa, Piazza dei Cavalieri 7, I-56126 Pisa, Italy
[5] Institute of Astrophysics, Foundation for Research and Technology-Hellas, Vasilika Vouton, GR-70013 Heraklion, Greece
[6] Department of Physics & ITCP, University of Crete, GR-70013, Heraklion, Greece
[7] Department of Physics & Astronomy, University of Wyoming, Laramie, WY, USA
[8] Space Telescope Science Institute, 3700 San Martin Drive, Baltimore, MD 21218, USA
[9] Inter-University Centre for Astronomy and Astrophysics, Post Bag 4, Ganeshkhind, Pune 411007, India
[10] Institute of Astronomy and Kavli Institute for Cosmology, University of Cambridge, Madingley Road, Cambridge CB3 0HA, UK
[11] Universities Space Research Association, NASA Ames Research Center, Moffett Field, CA 94035, USA
[12] Department of Astronomy and Astrophysics, University of Chicago, Chicago, IL 60637, USA
[13] Department of Astronomy, University of Wisconsin–Madison, 475 North Charter Street, Madison, WI 53706, USA
[14] Department of Physics, University of Wisconsin–Madison, 1150 University Avenue, Madison, WI 53706, USA
Received 2022 May 2; revised 2022 July 6; accepted 2022 July 6; published 2022 September 5

Abstract

We present the first data release of the Survey on extragALactic magnetiSm with SOFIA (SALSA Legacy Program) with a set of 14 nearby (<20 Mpc) galaxies with resolved imaging polarimetric observations using HAWC+ from 53 to 214 μm at a resolution of 5″–18″ (90 pc–1 kpc). We introduce the definitions of and background on extragalactic magnetism and present the scientific motivation and sample selection of the program. Here we focus on the general trends in the emissive polarization fraction. Far-infrared polarimetric observations trace the thermal polarized emission of magnetically aligned dust grains across the galaxy disks with polarization fractions of $P = 0\%$–15% in the cold, $T_{\rm d} = [19,\ 48]$ K, and dense, $\log_{10}(N_{\rm HI+H_2}[{\rm cm}^{-2}]) = [19.96, 22.91]$, interstellar medium. The spiral galaxies show a median $\langle P_{154\ \mu{\rm m}}\rangle = 3.3\% \pm 0.9\%$ across the disks. We report the first polarized spectrum of starburst galaxies showing a minimum within 89–154 μm. The falling 53–154 μm polarized spectrum may be due to a decrease in the dust grain alignment efficiency produced by variations in dust temperatures along the line of sight in the galactic outflow. We find that the starburst galaxies and the star-forming regions within normal galaxies have the lowest polarization fractions. We find that 50% (seven out of 14) of the galaxies require a broken power law in the $P - N_{\rm HI+H_2}$ and $P - T_{\rm d}$ relations with three different trends. Group 1 has a relative increase of anisotropic random B-fields produced by compression or shear of B-fields in the galactic outflows, starburst rings, and inner bars of galaxies, and groups 2 and 3 have a relative increase of isotropic random B-fields driven by star-forming regions in the spiral arms and/or an increase of dust grain alignment efficiency caused by shock-driven regions or evolutionary stages of a galaxy.

Unified Astronomy Thesaurus concepts: Polarimetry (1278); Far infrared astronomy (529); Starburst galaxies (1570); Active galactic nuclei (16); Spiral galaxies (1560); Interstellar medium (847); Interstellar dust (836); Extragalactic magnetic fields (507); Star formation (1569)

1. Introduction

Recent far-infrared (FIR; 50–220 μm) and submillimeter (850 μm) imaging polarimetric observations have opened a new window of exploration for extragalactic magnetism. The orientation of the magnetic fields (B-fields) has been measured in the dense and cold regions of the interstellar medium (ISM) of nearby galaxies by means of magnetically aligned dust grains (Lopez-Rodriguez et al. 2018; Jones et al. 2019; Jones et al. 2020; Lopez-Rodriguez et al. 2020; Borlaff et al. 2021; Lopez-Rodriguez et al. 2021a, 2021b; Lopez-Rodriguez 2021; Pattle et al. 2021). These results have been obtained using the High-Angular Wideband Camera Plus (HAWC+; Vaillancourt et al. 2007; Dowell et al. 2010; Harper et al. 2018) on board the 2.7 m Stratospheric Observatory For Infrared Astronomy (SOFIA) and POL-2 on the James Clerk Maxwell Telescope.

This manuscript presents the Survey on extragALactic magnetiSm with SOFIA (SALSA) Legacy Program (PI: E. Lopez-Rodriguez & S. A. Mao). SALSA aims to construct a comprehensive empirical picture of the B-field structure in the multiphase ISM as a function of the gas dynamics of several types of galaxies from hundred parsec to kiloparsec scales. This SOFIA Legacy Program relies on a multiwavelength approach to trace the strength and morphology of the B-fields using FIR and radio polarimetric observations. These observations are combined with neutral and molecular emission line observations, tracing the gas dynamics in the disk of galaxies. Star

* SALSA provides a software repository at https://github.com/galmagfields/hawc and publicly available data at http://galmagfields.com/.

formation tracers are also used to study the effect of star-forming regions on the galaxy's B-field. Early results (Borlaff et al. 2021; Lopez-Rodriguez et al. 2021a, 2021b; Lopez-Rodriguez 2021) of this program have successfully demonstrated this multiwavelength approach to characterize the B-field in the multiphase ISM of several galaxy types (i.e., mergers, spirals, and starburst galaxies). Here we present a brief background on extragalactic magnetism, describe the definitions of the B-fields in galaxies, and raise open questions regarding the role of B-fields in galaxy evolution (Section 2). Section 3 presents the scientific goals, observing strategy, and galaxy sample of the program. Section 4 presents the first results of the data release focused on the polarization fraction. We discuss the trends of the polarization fraction as a function of the relative contribution of the ordered and random B-fields, the polarized spectrum of starburst galaxies, the effect of galaxy inclination on the polarization fraction, and a comparison with the Planck results on the Milky Way in Section 5. Our conclusions are presented in Section 6.

2. Background

2.1. Radio Observational Signatures of Magnetic Fields in Galaxies

Most of our knowledge about B-fields in galaxies has been established using radio polarimetric observations in the 3–20 cm wavelength range (see, e.g., Beck & Wielebinski 2013, and updates, for a review). This wavelength range traces the B-fields via synchrotron emission and Faraday rotation measurements arising from the warm and diffuse phase of the ISM. These remarkable efforts have demonstrated the ubiquity of B-fields from galactic to intergalactic scales and opened the question of the origin and evolution of the B-fields in galaxies across cosmic time.

Several decades of observations have shown that all spiral galaxies have large-scale ordered B-fields with an average strength of $\sim 5 \pm 2\ \mu$G (Beck et al. 2019). The total B-field strength, measured by synchrotron total intensity and assuming equipartition between the total B-field and total cosmic-ray electron density, is estimated to be $\sim 17 \pm 14\ \mu$G (Fletcher 2010; Beck et al. 2019). In face-on spiral galaxies, the most prominent B-field morphology is a kiloparsec-scale spiral pattern where the polarized emission is mostly spatially coincident with the interarm regions and strongest at the inner edges of arms (e.g., Han et al. 1999; Fletcher et al. 2011; Beck 2007, 2015). This result may be explained by the fact that B-fields in the arms are more turbulent when compared to those in the interarm regions. In edge-on spiral galaxies, the B-field morphology is observed to have a component parallel to the midplane of the disk and another component with an X-shaped structure extending several kiloparsecs above and below the disk (Hummel et al. 1988, 1991; Krause et al. 2020). Larger radio halos containing B-fields and cosmic rays are found in galaxies with higher star formation rate surface densities (Wiegert et al. 2015). The physical origin of the X-shaped B-field in the halos of spiral galaxies is still unclear.

Some dwarf and irregular galaxies have been observed to have ordered B-fields with similar strengths to those in spiral galaxies and on scales comparable to the galaxy size (Chyży et al. 2000, 2003; Kepley et al. 2010). These ordered B-fields have even been observed in galaxies without spiral arms (e.g., NGC 4736; Chyży & Buta 2008). Ordered spiral B-field patterns have also been observed in the Large (Klein et al. 1993; Mao et al. 2012) and Small (Mao et al. 2008; Livingston et al. 2022) Magellanic Clouds.

Starburst galaxies have the strongest measured B-field strengths of $\geqslant 50\ \mu$G (Adebahr et al. 2013; Lacki & Beck 2013; Adebahr et al. 2017) with ordered B-fields along the plane of the galaxy and an X shape away from the disk (Heesen et al. 2011; Adebahr et al. 2013, 2017). The starburst ring in the central 1 kpc of NGC 1097 has the strongest B-field strength, $\geqslant 60\ \mu$G, in a barred galaxy (Tabatabaei et al. 2018) with an ordered spiral B-field morphology toward the center of the galaxy (Beck et al. 1999, 2005).

In interacting galaxies, large-scale B-fields have been found to (a) be partially ordered and tracing tidal tails and (b) have stretched spiral arms with stronger total B-field strengths than in noninteracting spiral galaxies (Chyży & Beck 2004; Drzazga et al. 2011; Basu et al. 2017). Interacting galaxies in the Virgo Cluster show asymmetric polarized intensities (PIs) in the outer edges of the galactic disks due to interaction with the cluster environment (Vollmer et al. 2007). Galaxy clusters at $z \sim 0.6$–0.9 show similar B-field strengths to those in the Virgo Cluster (Di Gennaro et al. 2021). Galaxies up to $z \sim 2$ have been observed to have coherent B-fields with strengths similar to those in the local universe (Bernet et al. 2008; Mao et al. 2017). As the largest structures of the universe, filamentary structures connect the galaxies forming the cosmic web, which is thought to be permeated by gas and B-fields. At these scales, recent radio observations using the LOw-Frequency ARray (LOFAR) have obtained upper-limit constraints on the median intergalactic B-field of $\leqslant 0.25\ \mu$G at scales of 10 Mpc (Locatelli et al. 2021).

2.2. Optical and Near-infrared Observational Signatures of Magnetic Fields in Galaxies

Studies of interstellar polarization at optical and near-infrared (NIR; 1–2 μm) wavelengths can reveal (a) the B-field geometry as a result of magnetically aligned elongated dust grains by radiative alignment torques (RATs; Hoang & Lazarian 2016; for a review see Andersson et al. 2015; for a summary see Section 3.1) and (b) the scattering properties of dust and/or electrons. Both polarization mechanisms have distinguishable polarization signatures. For absorptive polarization, the polarization fraction, P, is expected to be of a few percent with a position angle (PA) of polarization parallel to the orientation of the local B-field. For scattering off the dust and electrons, the polarization fraction is expected to be up to tens of percent, and the PA of polarization is perpendicular to the last direction of flight of the radiation to our line of sight (LOS). Scattering processes produce an azimuthal (centrosymmetric) pattern in the PA of polarization centered on the object radiating the ISM.

Pioneering work by Elvius (1962) and Elvius & Hall (1964) using optical polarimetric observations of nearby spiral and starburst galaxies showed a diversity of polarization mechanisms and physical components. Some edge-on spiral galaxies (e.g., Centaurus A and NGC 4631) show PAs of polarization parallel to the dust lane. Elvius & Hall (1964) interpreted these results as absorptive polarization arising from magnetically aligned dust grains. These authors invoked a large-scale B-field parallel to the galaxy's disks following the velocity field of the galaxy. Further optical (see, e.g., Berry 1985; Scarrott et al. 1996; Scarrott 1996, for a review) and NIR (Jones 2000)

polarization observations of several edge-on spiral galaxies found a PA of polarization parallel to the disks of galaxies. These results confirmed the interpretation of a large-scale B-field parallel to the dust lane. However, dust scattering was also found to be the dominant polarization mechanism at optical wavelengths in several other edge-on galaxies (Fendt et al. 1996).

For the starburst galaxy M82, Elvius (1962) measured strong polarization fractions, $P \geqslant 16\%$, in regions up to $\sim$2 kpc above and below the disk. The PA of polarization was measured to have an axisymmetric pattern centered at the core of the galaxy. This polarization pattern is also measured at the outskirts, $\geqslant 2$ kpc, of the galaxy's disk. In addition, low polarization fractions, $P \leqslant 2\%$, and a PA of polarization parallel to the disk were found within the central $\sim$1.5 kpc of the galaxy. The polarization in the outskirts of the galaxy was interpreted as scattering off the dust grains directly radiated by the central starburst. The polarization at the core of the galaxy may be interpreted as the galactic B-field in the disk arising from absorptive polarization of magnetically aligned dust grains. Further 1.65 and 2 μm observations confirmed the contribution of a large-scale B-field across the galaxy's disk and dust scattering above and below the disk of the starburst galaxy M82 (Jones 2000). This result was found after the scattering pattern was removed by subtracting an azimuthal pattern centered at the starburst. Another starburst galaxy, NGC 1808 (Scarrott et al. 1993), shows azimuthal patterns in the PA of polarization, which indicates that dust scattering is the dominant mechanism at optical wavelengths.

For face-on spiral galaxies, optical polarimetric observations of M51 (Scarrott et al. 1987) and NGC 6946 (Fendt et al. 1998) using 4 m class telescopes show similar patterns in the PA of polarization to those measured at radio wavelengths (Klein et al. 1982; Beck et al. 1987; Beck 2007; Fletcher et al. 2011). Specifically, M51 shows $P \sim 2\%$ and up to 5% in NGC 6946 with a pattern of the PA of polarization that is mostly azimuthal and centered at the galaxy's core. King (1986) performed optical polarimetric observations of NGC 7331 and also found a dominant asymmetric pattern along the major axis of the galaxy. Absorptive polarization may be observed in the eastern outskirts of NGC 7331. These observations were performed without a filter covering the 0.45–1.0 μm wavelength range with a peak at 0.85 μm. Specifically, the observations were performed using the full wavelength response of the CCD; thus, the final measured polarization can be a mix of multiple polarization mechanisms (i.e., dust/electron scattering and dichroic absorption). Using 1.6 μm imaging polarization observations of M51, Pavel & Clemens (2012) measured an upper limit of $\sim$0.05% in the polarization fraction across the full galaxy's disk. The scattering cross section declines much faster, $\propto \lambda^{-4}$, than absorption, $\propto \lambda^{-1}$, between 0.55 and 1.65 μm (Jones & Whittet 2015). These observations support dust scattering as the most likely polarization mechanism at optical and NIR wavelengths.

Given the contamination of dust scattering at optical and NIR wavelengths, the search for B-fields in galaxies is very complex. Data analysis techniques, such as those developed by Jones (2000), that aim to remove the azimuthal PA of polarization in M82 may minimize the dust scattering pattern at optical and NIR wavelengths. However, the resultant polarization pattern, expected to arise from absorptive polarization, may be jeopardized by a residual contribution from the highly polarized scattering mechanism. The results of the B-field orientation and strength in galaxies using these residuals need to be interpreted with caution. Deeper polarimetric observations at optical and NIR wavelengths are still required to disentangle the contribution of dust scattering and absorptive polarization to measure the contribution, if any, of B-fields in galaxies.

2.3. Observational Definitions of Magnetic Fields in Galaxies

Before we continue with the origin and role of B-fields in galaxy evolution, we must define the B-field components in galaxies from an observational framework. Here we follow the common nomenclature used in galaxies described by Beck et al. (2019). Following these definitions, the total synchrotron emission traces the total B-field component in the plane of the sky (POS), which depends on the total B-field strength and the cosmic-ray electron density. The total B-field can be separated into a regular (or coherent) component and a random component. The random B-field can be a turbulent one with a Kolmogorov power spectrum and a driving scale of 50–100 pc or a tangled regular B-field that reveals a different power spectrum with larger spatial scales (Gent et al. 2021). Present-day observations with a spatial resolution of a few hundred parsecs cannot distinguish between turbulent B-fields and tangled regular B-fields. A well-defined B-field direction within the beam size of the observations is described as a regular B-field. These regular B-fields can be traced using Faraday rotation measures, which are sensitive to the direction of the B-field along the LOS.

The random B-fields may have spatial reversals within the beam of the observations, which can be isotropic or anisotropic. The directions of the isotropic random B-fields have the same dispersion in all spatial dimensions. If an averaged B-field orientation remains after several reversals within the beam of the observations, then the B-fields are known as anisotropic random B-fields. Polarized synchrotron emission traces the ordered B-fields in the POS, which depends on the strength and geometry of the B-fields and cosmic-ray electron density. The anisotropic random and regular B-fields both contribute to the polarization and are referred to as ordered B-fields. Thus, the polarized synchrotron emission increases when the averaged anisotropic random B-field increases. Unpolarized synchrotron emission can be identified with isotropic random B-fields within the beam of the observations. The PA of polarization, corrected for Faraday rotation, traces the B-field orientation in the POS with a $180^\circ \times n$ ambiguity.

We use these definitions to describe the B-fields traced by FIR polarimetric observations in Section 3.1. Note the different nomenclature in the literature when describing B-fields in galaxies and the Milky Way, where our defined ordered B-fields are labeled as anisotropic random fields, tangled fields, striated, or ordered random (Jaffe 2019).

2.4. The Galactic Dynamo Theory

How B-fields have evolved from primordial seeds into their present-day configuration in galaxies remains an open question in astrophysics. The leading theory is based on dynamos that rely on the turbulent nature of the plasma flows, the so-called turbulent dynamos (Subramanian 1998; Brandenburg & Subramanian 2005). Turbulent dynamos are classified as either mean-field or fluctuation dynamos. The regular B-fields are thought to be generated by the mean-field dynamo that relies on

differential rotation of the galactic disk and turbulent helical motions to amplify and order a "seed" B-field. The turbulent B-fields are thought to be generated by turbulent gas motions at scales smaller than the energy-carrying eddies (Brandenburg & Subramanian 2005), driven by supernova explosions with coherence turbulent scales of $l \sim 50$–100 pc (Ruzmaikin et al. 1988; Brandenburg & Subramanian 2005; Haverkorn et al. 2008; Shukurov & Subramanian 2021). The correlation length of the turbulent or random B-fields is comparable to or smaller than the coherent turbulent scale, l. The fluctuation dynamos are also named small-scale dynamos, while the mean-field dynamos are also referred to as large-scale dynamos. This depends on whether the B-field scale is well below or above the turbulent scale, respectively. In general, the dynamo action can work as follows: the turbulent motions driven by supernova explosions tangle B-fields in the ISM, causing a transfer of turbulent magnetic and kinetic energy to smaller scales, at which they are converted into heat (i.e., turbulent diffusion). The same turbulent motions can also amplify the B-fields via electromagnetic induction (Zeldovich et al. 1990).

How these dynamo processes can explain the wide range of observational features (Sections 2.1 and 2.2) remains poorly understood. For example, Van Eck et al. (2015; and, more recently, Beck et al. 2019) compared the B-field strengths and morphology with the properties of the ISM for 20 nearby galaxies. They found that the total B-field strength is correlated with the star formation rate, $B_{\rm tot} \propto {\rm SFR}^{0.34\pm0.04}$. These results confirm the theoretical prediction of $B_{\rm tot} \propto {\rm SFR}^{1/3}$ (Schleicher & Beck 2013; Schober et al. 2016). These models were computed for a galaxy dominated by turbulence driven by supernova explosions and where the energy of the turbulent B-field is a fixed fraction of the turbulent energy. In addition, the ratio between the regular and ordered B-fields is found to increase radially in most galaxies. This result implies that the relative contribution of the fluctuation dynamo becomes less efficient than the mean-field dynamo with the galactocentric radius.

Furthermore, the magnetic pitch angle, $\Psi_{\rm B}$, provides information about the large-scale B-field that can be used to refine dynamo models. From theory, the $\Psi_{\rm B}$ involves the ratio of the radial, B_r, and azimuthal, B_ϕ, components of the B-field, such as $\Psi_{\rm B} = \arctan(B_r/B_\phi)$ (Krasheninnikova et al. 1989). From observations, the $\Psi_{\rm B}$ is defined as the angle between the B-field orientation and the tangent to the local circumference at a given distance from the galaxy's center. The $\Psi_{\rm B}$ can be estimated using the inferred B-field orientation from radio polarimetric observations and corrected by Faraday rotation. Beck et al. (2019) compiled the magnetic and optical arm pitch angles of 19 galaxies and found that, for the most well-studied spiral galaxies, the magnetic pitch angle is mostly constant within the central ∼5–10 kpc with values in the range of 20°–35°. They also found that the pitch angles of regular B-fields vary from those of the ordered B-fields, which may indicate a higher relative presence of the fluctuation dynamo in the pitch angle of the ordered B-fields. Interestingly, the magnetic pitch angle seems to be systematically offset by 5°–10° when compared with the molecular (CO) spiral arms (Van Eck et al. 2015). Note that this systematic offset is derived using a logarithmic spiral function fitted to the CO spiral arms and a multimode logarithmic spiral B-field fitted to the magnetic arms. Then, a median pitch angle value of the entire galaxy is estimated and compared between tracers. A wavelet-based analysis of the spiral pattern in the galaxy M83 revealed that the average pitch angle of the ordered magnetic field is about 20° larger than that of the material spiral arms (Frick et al. 2016). A homogeneous analysis of the pitch angles as a function of the galactocentric radius and galaxy structures is required to refine these results.

The PI can be used as a proxy of the large-scale ordered B-field. Using this relation, Tabatabaei et al. (2016) found that the large-scale ordered B-field strength is proportional to the rotational speed of 26 nearby galaxies. This result may be due to a potential coupling between the large-scale B-field and the dynamical mass of galaxies. This result leads to the argument that the large-scale B-field is enhanced and ordered due to gas compression and local shear in the disks of galaxies and hence dominated by anisotropic random fields. Finally, Chyży et al. (2017) applied a principal component analysis to several properties of the B-field and ISM using a sample of 55 nearby galaxies (i.e., low-mass dwarfs, Magellanic types, spirals, and starbursts). They also found that the B-field strength is tightly related to the surface density of the star formation rate, but it is also related to the gas density. Weak relationships are found between the B-field strength and the dynamic mass of galaxies and their rotation velocity. These results suggest that the B-field generation is related to the local star formation activity, which involves the action of fluctuation dynamos.

Although theoretical predictions and observations have been compared, the turbulent dynamo is still poorly constrained. To understand turbulent dynamos in galaxies, we are required to measure the strength and morphology of B-fields in the multiphase ISM of several galaxy types across their evolution. However, the angular resolution of the observations is typically larger than the coherence length of the turbulence in nearby galaxies. Thus, direct comparisons between observations and realistic magnetohydrodynamical (MHD) simulations are required to characterize the physical mechanisms producing the aforementioned observational results.

2.5. Magnetic Fields in Galaxy Evolution

Despite the origin of a seed B-field at the early stage of the universe during its accelerated expansion (e.g., Widrow 2002; Subramanian 2019), B-fields had to be amplified across cosmic time to explain the present-day B-fields in galaxies. In the cosmic web, B-fields may be amplified by fluctuation dynamos driven by accretion shocks. This mechanism transfers gravitational collapse into turbulent magnetic energy (e.g., Ryu et al. 2008) and may explain the measured B-field in cosmic filaments and galaxy clusters (Vazza et al. 2014, 2018). Following the hierarchical structure of galaxy formation by the standard ΛCDM cosmological model, dwarf galaxies may be one of the first galaxies to form in the universe. Dwarf galaxies have more turbulent gas and slower rotations than nearby spiral galaxies. However, the measured B-fields in local dwarf galaxies have strengths and kiloparsec-scale structures similar to spiral galaxies (Chyży et al. 2000, 2003; Kepley et al. 2010; Chyży et al. 2016). The B-fields in dwarf galaxies are puzzling, but they are crucial to understanding the evolution and amplification of B-fields during the early stages of the universe.

Minor and major mergers are thought to be a main mechanism for galaxy growth during the early stages of the universe (e.g., Kereš et al. 2009). These mergers affect the ISM of the galaxies, perturbing their B-fields. Studies of 16 interacting systems have shown that (a) the mean ordered

B-field strength, 14 ± 5 μG, is stronger than in noninteracting galaxies ($\sim 5 \pm 2$ μG); (b) the ratio of the ordered to random B-fields is lower than in noninteracting galaxies; and (c) the ordered B-fields are strong along the tidal tails of the interacting galaxies (Chyży & Beck 2004; Drzazga et al. 2011). A recent study (Lopez-Rodriguez 2021) of Centaurus A, a remnant galaxy of a major merger between an elliptical and a spiral galaxy, has shown a highly perturbed B-field along the warped disk of the galaxy. The observed B-field is thought to be dominated by the fluctuation dynamo at scales $\leqslant$120 pc. This result indicates that the measured B-field is the perturbed large-scale B-field of the original spiral galaxy after the merger. These results show that B-fields may be amplified by the enhancement of turbulent motions in the mergers driven by galaxy interaction. These strong B-fields may quench star formation (Tabatabaei et al. 2018) and drive the gas flows in tidal tails. However, it remains unclear how the B-fields are amplified and when the B-field dissipates in mergers.

Mergers can trigger starburst activity (e.g., Elbaz & Cesarsky 2003; Tacconi et al. 2010; Pearson et al. 2019), where the already amplified B-field from mergers can be further enhanced via turbulent dynamos due to supernova explosions (Schober et al. 2013). Indeed, the strongest B-fields, 50–300 μG, are found at the core of starburst galaxies with their ordered B-fields following the galactic outflows (e.g., Thompson et al. 2006; Heesen et al. 2011; Adebahr et al. 2013, 2017; Lopez-Rodriguez et al. 2021a). The B-field strengths of 0.5–18 mG are measured in starbursts using the Zeeman effect in the OH megamasers (Robishaw et al. 2008). Furthermore, the tight FIR–radio correlation applies to redshifts of at least $z \sim 3$ (Murphy 2009). This result requires that the turbulent B-field and star formation are linked during the peak of star formation at $z \sim 1$ (Heavens et al. 2004; Seymour et al. 2008). The strong and ordered B-fields found in starbursts have effects on galaxy evolution. Galactic outflows can drag the B-fields from the galaxy's disk away to the intergalactic medium (IGM), which is then permeated by B-fields (e.g., Bertone et al. 2006; Samui et al. 2018; Pakmor et al. 2020; Martin-Alvarez et al. 2021; Lopez-Rodriguez et al. 2021a). Galaxy formation simulations also find temporary merger-induced amplification and attribute this amplification to a combination of compressional and merger-driven turbulence (Kotarba et al. 2011; Martin-Alvarez et al. 2018; Whittingham et al. 2021). These simulations also find some resolution-dependent B-field dissipation once the merging process concludes. A variety of mechanisms (e.g., winds, B-fields, cosmic rays, and diffusion losses) are interconnected and still under investigation (e.g., Lacki et al. 2010; Birnboim et al. 2015).

The subsequent story of galaxy evolution from poststarburst (Caldwell et al. 1999) to quiescent galaxies starts with a strong and ordered B-field. These B-fields are in close equipartition with the turbulent kinetic energy in the galactic outflows (Thompson et al. 2006; Lopez-Rodriguez et al. 2021a), which makes the B-fields dynamically important during and after the starburst activity. Large reservoirs of turbulent molecular gas and quenched star formation have been found in poststarburst galaxies (e.g., Falgarone et al. 2017; Wild et al. 2020; Suess et al. 2022; French et al. 2022). Strong B-fields have been found to be responsible for reducing star formation rates in molecular clouds (Mouschovias et al. 2006; Pattle et al. 2022) and modifying the ISM by forming filamentary structures (Hennebelle & Inutsuka 2019). Furthermore, strong B-fields in the starburst ring of NGC 1097 have been found to quench the formation of massive stars (Tabatabaei et al. 2018). These results may indicate that strong B-fields in poststarburst galaxies may quench star formation by keeping the molecular gas from gravitationally collapsing to form massive stars in the galaxy after the cease of starburst activity. To characterize the effect of B-fields on the reservoirs of molecular gas and the subsequent star formation activity, it is required to perform studies of the ordered B-fields in poststarburst galaxies.

The evolutionary stage toward quiescent galaxies is the longest timescale to order B-fields in the present-day spiral galaxies. The observed ordered B-fields in nearby galaxies may be explained by an interplay between mean-field dynamos driven by differential rotation (and helical turbulence) in galaxies, fluctuation dynamos driven by feedback-driven mechanisms (from stellar and/or active galaxies), and/or magnetorotational instability-driven dynamos (Kitchatinov & Rüdiger 2004; Wang & Abel 2009; Arshakian et al. 2009; Rieder & Teyssier 2016; Bambic et al. 2018; Martin-Alvarez et al. 2018; Ntormousi 2018; Ntormousi et al. 2020). Recent efforts using MHD simulations have shown that the structure of a galactic disk can be modified when B-fields are included. For example, smaller disks and higher accretion flows toward their cores are found if strong primordial B-field strengths are assumed in MHD simulations (Martin-Alvarez et al. 2020). More disk-dominated and massive black holes are found if B-fields are added in Milky Way–mass galaxies (van de Voort et al. 2021). However, the exact physical processes of B-field amplification to reach the present-day B-field measurements remain an open question.

To sum up, B-fields are amplified from seed values as a consequence of galaxy formation and turbulence-driven dynamos. Galaxy evolution strongly depends on the physics of the ISM. In addition, the ISM is permeated by B-fields, in which magnetic energy is in close equipartition with the kinetic energy. The B-fields can be dynamically important at several stages of galaxy evolution. These B-fields generated via MHD dynamos can affect gas flows in the ISM and drive gas inward toward the galaxy's center and outward toward the IGM via galactic outflows. Thus, B-fields remain an important, but still largely ignored, element for understanding the evolution of galaxies across cosmic time.

3. Overview of the Legacy Program

We present the galaxy sample, observing strategy, and scientific goals of the program.

3.1. Measuring Magnetic Fields Using FIR Polarimetry

The results from this project rely on the fact that the dust grains are magnetically aligned with the local B-field. We summarize the fundamentals of dust grain magnetic alignment theory. Then, we provide the observational signatures to study the B-fields in galaxies using FIR polarimetric observations.

Theories of dust grain alignment mechanisms have been in active development since the first discovery of the polarization signature of aligned elongated dust grains in the ISM by Hiltner (1949) and Hall & Mikesell (1949). The RAT theory is the leading theory describing dust grain alignment (e.g., Andersson et al. 2015; Hoang & Lazarian 2016). The RAT theory can be summarized as follows. Starlight radiation transfers angular

momentum to the dust grains in the ISM. The dust grains absorb more radiation along one of their axes due to their asymmetric geometrical nature and end up spinning along the axis with the greatest moment of inertia (i.e., the minor axis of the dust grain). Since most dust grains are paramagnetic, they acquire a magnetic moment experiencing the fast Larmor precession. After a relaxation time, the dust grains will be precessing along the orientation of the local B-field. The final configuration is one where the long axis of the dust grains is perpendicular to the orientation of the local B-field.

The absorptive polarization has a PA of polarization parallel to the local B-field, while the emissive polarization has a PA of polarization perpendicular to the local B-field. This mechanism is known as B-RATs, and it is the most common property for interpreting polarimetric observations tracing the absorptive/emissive polarization in the IR and submillimeter wavelength range. Indeed, the induced polarization from dust grain alignment by RATs has been extensively used to interpret observations of the ISM in our Galaxy (Andersson et al. 2015, for a review) and other galaxies (e.g., Elvius 1962; Elvius & Hall 1964; Jones 2000; Lopez-Rodriguez et al. 2018; Jones et al. 2019; Lopez-Rodriguez et al. 2020; Jones et al. 2020; Lopez-Rodriguez et al. 2021a; Lopez-Rodriguez 2021; Borlaff et al. 2021; Pattle et al. 2021).

Polarized thermal FIR emission arising from magnetically aligned dust grains traces the ordered B-fields in the POS. The inferred B-field orientation from the HAWC+ observations is computed after the measured polarization angle (i.e., E-vector) is rotated by 90°. Note that the angle of the measured B-field has a 180° ambiguity due to the fact that FIR polarization is insensitive to the B-field direction. Thus, we only measure the B-field orientations on the POS using FIR polarimetric observations. In addition, the measured B-field orientation is the weighted-averaged column density along the LOS and on the POS within the several hundred parsec size of the resolution elements of the observations. The angular resolutions of HAWC+ are in the range of 5″–18″, which corresponds to spatial scales of ∼500 pc for a typical nearby galaxy at ∼10 Mpc and an angular resolution of 10″. The total FIR emission of galaxies has a typical vertical height of 0.1–0.6 kpc (Verstappen et al. 2013). Furthermore, the FIR polarimetry is not directly sensitive to the B-field strength, and the spatial resolution of the observations, a few hundred parsecs, is larger than the turbulent scales, $l \sim 50$–100 (Section 2.4), driven by supernova explosions in galaxies. Thus, the B-field strength cannot be estimated using the current set of observations, except for the rare occasion of M82 at 53 μm, where Lopez-Rodriguez et al. (2021a) modified the Davis–Chandrasekhar–Fermi method (Davis & Greenstein 1951; Chandrasekhar & Fermi 1953) to account for the large-scale galactic outflow.

The total intensity is sensitive to the dust grain column density and dust temperature. The polarization fraction is sensitive to the turbulent and/or tangled (i.e., random) B-fields along the LOS, B-field orientation with the POS, dust grain column density, and dust temperature. For a "perfect" condition, where the B-field orientation is parallel to the POS and there is no variation in either tangled B-fields, turbulence, or inclination effects, the polarization fraction is constant for an ordered B-field (i.e., maximum dust grain alignment efficiency). The polarization fraction decreases when the averaged anisotropic random B-field decreases and turbulence, tangled B-fields, and inclination effects increase (i.e., Chen et al. 2019; King et al. 2019). The FIR polarization fraction also decreases when the angle of the B-field with respect to the POS increases (Section 5.3). Unpolarized thermal emission can be attributed to isotropic B-fields and/or a B-field oriented perpendicular to the POS.

3.2. Science Goals

The science goals driving SALSA are motivated by the characterization of the B-fields in the multiphase ISM of galaxies. As mentioned in Section 2, our knowledge of extragalactic magnetism has been purely based on radio polarimetric observations tracing the B-fields in the warm and diffuse ISM. SALSA provides a new ingredient by doing what only HAWC+/SOFIA can do: measuring the B-fields in the dense and cold ISM of galaxies. Since the gas dynamics and star formation activity are the main drivers of the amplification and evolution of B-fields, our analysis is supported with observations of neutral and molecular gas, as well as star formation activity tracers. The sample selection (Section 3.3) was designed to address the following core goals.

1. *Characterize the dependence of the large-scale ordered B-fields on the probed ISM phase and provide measurements for galactic dynamo theories.*

   Spiral structures in galaxies can be described as density perturbations propagating in a multiphase ISM and multicomponent stellar disk (see Shu 2016, for a review). Several theories have been suggested to explain the formation of large-scale spiral arms: (a) as dynamic transients, where the spiral arms can change during a galaxy's lifetime (e.g., Sellwood & Carlberg 1984; Elmegreen & Thomasson 1993; Michikoshi & Kokubo 2016); (b) as constant density waves, where the spiral arms are stationary patterns that last most of the galaxy's lifetime (e.g., Bertin et al. 1989; Shu 2016); and/or (c) as the result of tidal encounters (e.g., Toomre & Toomre 1972; Elmegreen et al. 1991; Pettitt et al. 2017). Density wave theory predicts that stars form in the arms as gas moves into a wave that is compressed by its gravitational potential. Under this scheme, the pitch angle should be different for different tracers of star formation (e.g., molecular clouds, H II regions, and newly formed stars) because they appear at different phases of a wave. The pitch angle at optical/NIR wavelengths is expected to trace already-born stars. The FIR wavelengths trace spiral density waves colocated with newly born stars where the radiation arises from thermal emission from dust grains. Radio wavelengths trace synchrotron emission from a volume-averaged electron density region along the halo and disk of the galaxy. Despite the fact that unique or combined theories can describe the evolution of spiral galaxies, these theories have to predict the large-scale ordered B-fields found in all spiral galaxies using polarimetric observations (e.g., Beck & Wielebinski 2013; Beck et al. 2019).

   The B-fields should be compressed and sheared by the action of these density waves, adding another observable tracer to the previous photometric ones. Constant offsets within the full disk between photometric and polarimetric tracers are expected for a density wave and were indeed observed in M51 (Patrikeev et al. 2006). Galaxy dynamo theories also have to predict the

differences between the morphological spiral arms traced by neutral and molecular gas and the large-scale ordered spiral B-fields traced by radio polarimetric observations (Van Eck et al. 2015; Beck et al. 2019). The HAWC+ polarimetric observations of NGC 1068 at 89 μm showed the first detection of an ∼3 kpc large-scale ordered spiral B-field structure (Lopez-Rodriguez et al. 2020). The B-fields were traced by means of thermal polarized emission arising from magnetically aligned dust grains. The measured ordered B-field morphology was characterized by a two-dimensional logarithmic spiral B-field model with a pitch angle of $16.9^{+2.7\circ}_{-2.8}$ and a disk inclination of $48^\circ \pm 2^\circ$. The matter sampled by the estimated 89 μm magnetic pitch angle follows the starbursting regions with a pitch angle of 15° using H_α along the spiral arms (Emsellem et al. 2006). The magnetic pitch angle shows an offset from that of the molecular gas with a pitch angle of 7°–10° (Planesas et al. 1991). These results show a constant offset between the FIR and radio magnetic arms and the molecular gas arms using an average pitch angle across the galaxy's disk.

The wavelet-based analysis in M83 showed that one gaseous arm is displaced from the magnetic arm, while the other magnetic arm overlaps with the associated gaseous arm (Frick et al. 2016). This result was interpreted as the interaction between a galactic dynamo and a transient spiral arm. More recently, Borlaff et al. (2021) measured that the ordered large-scale B-fields in M51 do not necessarily have the same morphology using FIR, radio, CO, and H I tracers. Specifically, the spiral arms are wrapped tighter at H I and CO than at FIR and radio wavelengths. These authors performed a study of the radial profiles of the spiral arms as a function of the galactocentric radius. The results showed that the 154 μm ordered large-scale B-field is wrapped tighter at the outer parts, $r > 5$ kpc, of the galaxy than those traced by radio polarimetric observations. This result has been interpreted as a consequence of galaxy interaction and/or star formation activity in the outskirts of M51. Furthermore, several modes of an axisymmetric B-field toward the galactic center of NGC 1097 were measured using FIR and radio polarimetric observations (Lopez-Rodriguez et al. 2021b). Specifically, a constant B-field traced at 89 μm was measured to be associated with the contact regions between the bar and the starburst ring within the central 1 kpc of NGC 1097. A superposition of spiral B-fields at 3 and 6 cm was measured outside and within the starburst ring. These results deviate from the constant density wave theory in terms of how the spiral arms behave as a function of the galactocentric radius and the specific tracer used to describe the spiral arms. Other physical mechanisms, such as transient arms and/or galaxy interaction, may need to be taken into account to explain these measurements. However, only a handful of spiral galaxies have been studied thus far.

In general, density wave theories do not include angular momentum transfer through the action of B-fields. However, a galaxy like NGC 1097 suggests that B-fields drive inflows on kiloparsec scales via MHD dynamos, and galaxies like M51 and M83 suggest that magnetic pitch angles change with the galactocentric distance due to galaxy interaction and/or star formation activity. It is mandatory to review the relative contribution of gravitational and magnetic forces in the global buildup of spiral arms. We need a comprehensive spiral density wave theory that includes these two forces.

One of the goals of SALSA is to provide the B-field structure along the ongoing star-forming regions traced by FIR thermal polarized emission arising from magnetically aligned dust grains. These results are complementary to the B-field structures traced by radio polarimetric observations where the polarized emission is mostly spatially located with the interarm regions and is strongest at the inner edges of the arms (Section 2.1). In combination with neutral and molecular gas observations, SALSA aims to trace the B-field and morphological structures of the spiral arms and interarm regions as a function of the multiphase ISM and gas dynamics in the disks of spiral galaxies. This study provides empirical inputs for dynamo models that can be used to obtain a conclusive theory of the evolution of spiral galaxies.

2. *Quantify the relative contributions of the mean-field and fluctuation dynamos across a range of galaxy types and dynamical states.*

Present-day B-fields in galaxies are a consequence of turbulence-driven dynamos (Section 2.4). However, the relative contribution of the fluctuation and mean-field dynamos and the physical conditions in the galaxy at which B-fields are amplified and dissipated are still under study. The current angular resolutions of the observations in radio and FIR, 5″–20″ (⩾100 pc), are too large to resolve the fluctuation dynamo (i.e., coherence length of the turbulence) in nearby galaxies. Our measurements rely on the relative contribution of the fluctuation and mean-field dynamo across the several structures within the disks of galaxies.

Krause et al. (2020) detected polarized synchrotron emission of 35 edge-on galaxies with vertical scale heights in the range of 1–6 kpc. The large-scale B-fields are dominated by an X-shaped morphology above and below the galaxy's disk with a mostly unpolarized disk due to strong Faraday rotation. The thermal FIR total emission along the vertical scale height of edge-on galaxies has been measured to be in the range of 0.1–0.6 kpc at 100–160 μm (Verstappen et al. 2013). The FIR thermal emission arises from dust grains heated by star-forming regions in the galaxy's disks. As an example, the thermal FIR polarized emission of the edge-on spiral galaxy NGC 891 has a vertical height of ⩽0.5 kpc (Jones et al. 2020). Thus, radio polarimetric observations trace the B-fields as a weighted average of the electron column density along the LOS across several kiloparsecs above and below the galaxy's disk. The radio polarimetric observations suffer from Faraday rotation. The FIR polarized emission traces the weighted-average column density B-field in the midplane of the galaxy and does not suffer Faraday rotation. Continuing with the example of NGC 891, the vertical height of the molecular gas, ^{12}CO(1–0) and ^{12}CO(3–2), is ∼0.4 kpc (Hughes et al. 2014), while the warm ionized gas extends up to

~2 kpc beyond the disk (Rand et al. 1990; Reach et al. 2020). The bulk of the star-forming regions and molecular gas is located close to the midplane of the galaxy, as well as the bulk of the thermal FIR emission. Thus, FIR polarimetric observations are a powerful tool for studying the effect of the gas kinetic energy in the ISM and star-forming regions on the relative contribution of the turbulence-driven dynamos across the galaxy's disk.

Using HAWC+ polarimetric observations of the face-on spiral galaxy M51, Borlaff et al. (2021) showed that the arms have a relative increase of small-scale turbulent B-fields in regions with increasing column density and ^{12}CO(1–0) velocity dispersion. The column density and velocity dispersion of the molecular gas were used as proxies of the turbulent kinetic energy of the gas in the ISM across the disk. In addition, these authors found that (a) the polarized synchrotron emission is strongly correlated with star formation rate except in the FIR, and (b) the polarized fraction decreases faster at FIR than at radio wavelengths with the star formation rate. These results imply an increase of the fluctuation dynamo in the star-forming regions, specifically, an increase of isotropic turbulent B-fields traced by FIR and anisotropic turbulent B-fields traced by radio.

For the merger remnant Centaurus A, Lopez-Rodriguez (2021) showed that the measured B-field in the warped disk is dominated by the fluctuation dynamo. This result was based on the decrease of the polarization fraction with (a) increasing column density, used as a proxy for the turbulent and/or tangled B-fields along the LOS; (b) increasing ^{12}CO(1–0) velocity dispersion, used as a proxy of the turbulent kinetic energy of the molecular gas; and (c) increasing dust temperature, used as a proxy of the radiation field in the ISM. In addition, the measured angular dispersions between the beam of the observations were larger than those associated with the individual uncertainties of the measured polarization angles. The measured PAs of polarization across the warped disk of Centaurus A were also not fully explained by a three-dimensional model of an ordered B-field. These early results have shown the potential of using FIR polarimetric observations to estimate the contribution of the fluctuation dynamo in the disks of galaxies.

SALSA aims to provide a statistical sample of nearby galaxies with resolved FIR polarimetric observations. These observations can be used to analyze the effects of star formation and tidal interactions on the turbulent dynamos across the disks of galaxies and galaxy types. These results may need further realistic MHD simulations to disentangle the dominant physical mechanism associated with the small-scale turbulent B-field below the resolution elements of our observations (e.g., Pakmor et al. 2014; Ntormousi 2018; Martin-Alvarez et al. 2018; Steinwandel et al. 2019; Ntormousi et al. 2020; Martin-Alvarez et al. 2022).

3. *Measure the effect of galactic outflows on the galactic B-field in starburst galaxies and quantify how the B-field is transported to the circumgalactic medium (CGM).*

Starburst galaxies may be important contributors to the magnetization of the IGM in the early universe (e.g., Kronberg et al. 1999; Bertone et al. 2006). Starbursts can amplify the galactic B-field and drag it away, magnetizing the CGM by means of fluctuation dynamos driven by supernovae (Section 2.5). Nearby starburst galaxies are excellent astrophysical laboratories due to the presence of enhanced star formation and the associated galactic outflows that may be magnetizing and enriching the IGM with new elements formed in the star-forming regions. These structures can be resolved with current optical/NIR, FIR, and radio polarimetric observations.

Optical polarimetric observations are highly contaminated by dust and electron scattering, making it very complicated to characterize the signature of magnetically aligned dust grains in starbursts (Section 2.2). Radio polarimetric observations of M82 show a dominant magnetized bar along the galaxy's disk (Heesen et al. 2011; Adebahr et al. 2013, 2017). However, these observations suffer from strong Faraday rotation, and only hints of the helical B-fields along the outflow were detected.

Preliminary HAWC+ results at 53 μm showed that the B-field structure traced by magnetically aligned dust grains is perpendicular to the disk and parallel to the galactic outflow in M82 (Jones et al. 2019). A further detailed analysis of these data found that the turbulent kinetic and magnetic energy are in close equipartition within the central ~2 kpc along the galactic outflow (Lopez-Rodriguez et al. 2021b). The B-fields in the galactic outflow of M82 remain "open" up to 10 kpc scales above and below the galactic disk. These results indicate that the B-fields in the galactic outflow of M82 are frozen into the ionized outflowing medium and driven away kinetically. In addition, small-scale turbulent B-fields arising from a bow shock are present within the outflow. These observations show that FIR polarimetric observations can trace and characterize the physical mechanisms of the B-field along the galactic outflow in starbursts.

SALSA aims to perform a multiwavelength analysis of the nearest and brightest starburst galaxies. These new observations can be used to measure the effect of the galactic outflow properties (i.e., mass and ejected energy), dust properties (i.e., density, alignment efficiency, and temperature), and CGM properties (i.e., tidal tails, gas velocity, and composition) on the galaxy's B-field. These results are crucial to understanding the mechanisms of B-field amplification driven by supernovae and magnetization of the CGM, where nearby starbursts can be used as analogs of galaxies at the peak of star formation at $z \sim 1$–2.

4. *Measure the B-field structures of interacting galaxies.*

Some of the fundamental questions in galaxy evolution can be distilled to: what happens when galaxies collide and merge? What is the effect of this interaction on star-forming regions? Major and minor merging events may perturb the B-field and enhance it by fluctuation dynamos (Sections 2.1 and 2.5). If the B-field is compressed, it will lead to strong radio polarized emission (Arshakian et al. 2009). Here we are interested in characterizing how the ordered B-fields of galaxies are distorted due to the interaction and merger of galaxies

Table 1
Galaxy Sample

Galaxy	Distance[1] (Mpc)	Scale (pc arcsec^{-1})	Type[a] (deg)	Inclination (i)[2] (deg)	Tilt (PA)[2] (deg)	References
(1)	(2)	(3)	(4)	(5)	(6)	(7)
Centaurus A	3.42	16.42	S0pec/Sy2/RG	83 ± 6	114 ± 4	[1] Ferrarese et al. (2007); [2] Quillen et al. (2010)
Circinus	4.20	20.17	SA(s)b/Sy2	40 ± 10	205 ± 10	[1] Tully et al. (2009); [2] Jones et al. (1999)
M51	8.58	41.21	Sa	22.5 ± 5	-7 ± 3	[1] McQuinn et al. (2017); [2] Colombo et al. (2014)
M82	3.85	18.49	I0/Sbrst	76 ± 1	64 ± 1	[1] Vacca et al. (2015); [2] Mayya et al. (2005)
M83	4.66	22.38	SAB(s)c	25 ± 5	226 ± 5	[1] Tully et al. (2013); [2] Crosthwaite et al. (2002)
NGC 253	3.50	16.81	SAB(s)c/Sbrst	78.3 ± 1.0	52 ± 1	[1] Radburn-Smith et al. (2011); [2] Lucero et al. (2015)
NGC 1068	14.40	69.16	(R)SA(rs)b/Sy2	40 ± 3	286 ± 5	[1] Bland-Hawthorn et al. (1997); [b] Brinks et al. (1997)
NGC 1097	19.10	92.21	SB(s)b/Sy1	41.7 ± 0.6	133.0 ± 0.1	[1] Willick et al. (1997); [2] Hsieh et al. (2011)
NGC 2146	17.20	82.61	SB(s)ab/Sbrst	63 ± 2	140 ± 2	[1] Tully (1988); [2] Tarchi et al. (2004)
NGC 3627	8.90	42.75	SAB(s)b	52 ± 1	176 ± 1	[1] Kennicutt et al. (2003); [2] Kuno et al. (2007)
NGC 3628	10.95	52.60	Sb pec	91.6 ± 2.0	90 ± 2	[1,2]Shinn & Seon (2015)
NGC 4038	22	105.67	SB(s)m pec	59 ± 10	55 ± 10	[1] Schweizer et al. (2008); [2] Amram et al. (1992)
NGC 4631	7.6	36.51	SB(s)d	89 ± 1	85 ± 1	[1] Seth et al. (2005); [2] Mora-Partiarroyo et al. (2019)
NGC 4736	5.3	25.46	SA(r)ab	36 ± 7	292 ± 2	[1] Kennicutt et al. (2003); [2] Dicaire et al. (2008)
NGC 4826	5.60	26.89	(R)SA(rs)ab	65 ± 5	125 ± 5	[1] Kennicutt et al. (2003); [2] Braun et al. (1994)
NGC 6946	6.80	32.66	Sc	38.4 ± 3.0	239 ± 1	[1] Karachentsev et al. (2000); [2] Daigle et al. (2006)
NGC 7331	15.7	75.40	SA(s)b	78.1 ± 2.7	165 ± 1.2	[1] Kennicutt et al. (2003); [2] Daigle et al. (2006)

Note. The columns are as follows: (1) galaxy name, (2) galaxy distance in megaparsecs, (3) physical scale in parsecs per arcsecond, (4) galaxy type, (5) inclination of the galaxy in degrees, (6) PA of the long axis of the galaxy in the POS, (7) references associated with the distance, inclination, and tilt angles, denoted with superscripts 1, 2, and 2, respectively.
[a] Galaxy type from the NASA/IPAC Extragalactic Database (NED; https://ned.ipac.caltech.edu/).

and their influence on star formation activity. Given the analysis of spiral galaxies and starbursts in this project (goals 1–3), SALSA provides the foundational framework to characterize more complex galaxies.

As mentioned in Section 2.5, the measured turbulent B-field in Centaurus A can be interpreted as the disturbed large-scale ordered B-field of the spiral galaxy after the major merger (Lopez-Rodriguez 2021). Unfortunately, radio polarimetric observations of the entire galaxy are not available, as most of the analysis at radio wavelengths has been focused on the active galactic nucleus. Thus, FIR polarimetric observations provide a new window to characterize the B-fields in the dense ISM of highly turbulent galactic disks. In addition, the differences in the B-field between FIR and radio wavelengths in M51 (Borlaff et al. 2021) can be a consequence of the interaction between M51a and M51b. Further observations of other interacting systems are required to understand their effect on the B-field morphology.

Merging galaxies are typically too faint for the HAWC+ sensitivities or too close to each other for the angular resolutions (5″–18″) of HAWC+. Based on the selection criteria explained in Section 3.3, the Antennae galaxy is the only merging galaxy that can be measured with HAWC+. This galaxy is well studied, bright, and the nearest merger with extensive archival data. Radio polarimetric observations of the Antennae galaxy have been used to estimate the B-field strength in the diffuse ISM (Chyży & Beck 2004). However, the densest regions of the merger are depolarized. Thus, FIR polarimetric observations are needed. SALSA will measure the B-field structure in the areas of interaction between both galaxies in the Antennae system. These observations can be used to characterize the B-fields with ongoing star formation along the gas streams between the merging galaxies.

3.3. Galaxy Sample

Our galaxy sample represents the most accessible and technically feasible galaxies in the nearby (<20 Mpc) universe to be observed with HAWC+. These galaxies are observed within a maximum on-source time of 7 hr for each object and each band to optimize and be compatible with the flight planning with other HAWC+ proposals within the multiyear period of this SOFIA Legacy Program. The full program was maximized to be within the 200 hr of execution time offered per SOFIA Legacy Program. Within this time, we selected a flux-limited galaxy sample of bright and nearby galaxies of several representative galaxy types to accomplish the scientific goals described in Section 3.2. Table 1 shows the properties of the galaxy sample. The selection criteria were based on the following.

1. The available data in the literature that support the physical interpretation of the HAWC+ observations. The available data include observations from the Very Large Array (VLA)/Effelsberg, Herschel, Hubble Space Telescope (HST), and Atacama Large Millimeter/submillimeter Array (ALMA).
2. The HAWC+ sensitivity to observing extended polarized emission within ∼2–10 kpc diameter in ⩽7 hr of observations.
3. Having several representative galaxy types that can be used to characterize the B-fields from spiral galaxies to more complex galaxies (i.e., interaction, starbursts, and active galactic nuclei).
4. Having complementary FIR polarimetric observations of the brightest galaxies already observed from previous

Table 2
HAWC+ Configuration

Band	λ_c (μm)	$\Delta\lambda$ (μm)	Pixel Scale (arcsec)	Beam Size (arcsec)	Polarimetry FOV (arcmin)
(1)	(2)	(3)	(4)	(5)	(6)
A	53	8.7	2.55	4.85	1.4×1.7
C	89	17	4.02	7.8	2.1×2.7
D	154	34	6.90	13.6	3.7×4.6
E	214	44	9.37	18.2	4.2×6.2

Note. The columns are as follows: (1) band name, (2) central wavelength of the band in microns, (3) FWHM bandwidth in microns, (4) pixel scale of the band in arcseconds, (5) FWHM in arcseconds, and (6) FOV for polarimetric observations in arcminutes.

HAWC+ programs. These new observations can be used to perform multiwavelength analysis.

The galaxy sample was originally selected from the Atlas of Galaxies[15] led by Maja Kierdorf and Rainer Beck at the Max Planck Institute for Radio Astronomy in Bonn, Germany. These galaxies are bright, nearby, and well studied using radio polarimetric observations (i.e., VLA and Effelsberg) with broad wavelength coverage from 3 to 23 cm with angular resolutions of 8″–20″. The radio polarimetric observations have similar angular resolutions as those from HAWC+ (Table 2).

Herschel data are used to (a) estimate the feasibility of the observations with HAWC+ in the 53–214 μm wavelength range and (b) compute the column density and dust temperature across the galaxy disk by using 70–250 μm PACS and SPIRE observations. Those galaxies without available data in the Herschel Archive[16] were removed from the galaxy sample.

Since one of the goals of this project is to characterize the B-field orientation with the underlying gas dynamics of the ISM, we selected galaxies with available neutral and molecular gas observations at similar or better angular resolution as those from HAWC+. ALMA observations provide the kinematics of the molecular gas, CO(1–0) and CO(2–1), of the galaxy disks. Objects with ALMA observations from the Physics at High Angular resolution in Nearby GalaxieS (PHANGS) project[17] (Leroy et al. 2021) and Nobeyama observations from the CO multi-line imaging of nearby galaxies (COMING) project (Sorai et al. 2019) were selected. Spiral galaxies without H I data from The H I Nearby Galaxy Survey (THINGS;[18] Walter et al. 2008) were removed from the sample. In addition, ultraviolet (UV) emission can be used as a proxy for star formation activity. Galaxies without available UV imaging observations (i.e., HST/WFC3/F438W) from the HST Archive[19] were removed from the sample.

Given the total surface brightness of the galaxies using the Herschel observations, we finally selected galaxies that can be observed within $\leqslant$7 hr on-source time with the sensitivity criteria described below. The 7 hr on-source time limit is based on how the observations are scheduled by SOFIA flight planning. The 7 hr limit allows SOFIA to obtain the full observations of a galaxy within two flights, with an observing time leg of 3.5 hr each. The maximum leg of a single flight is ~4 hr, as SOFIA has to return to the same base, i.e., Palmdale in California, at the end of the flight. An optimal flight has two science legs of 3.5 hr and a single leg of 0.5 hr for calibrations, yielding a total time of 8 hr of science observations per flight. Using this scheme, a minimum of two galaxies can be scheduled for observations within the same flight. Note that the aircraft has to return to the same base, so each of the 3.5 hr science legs point to opposite parts of the sky. In addition, given that the galaxies are uniformly distributed in the sky, this program is ideal for flight planning compatible with over-subscribed regions like the Galactic center. This approach helps flight planners who schedule SOFIA flights.

The individual integration times for the imaging polarimetric mode were obtained using the SOFIA Instrument Time Estimator (SITE[20]) at 53, 89, 154, and 214 μm using the chop-nod (C2N) polarimetric technique. To obtain statistically significant polarimetric measurements of the diffuse polarized emission across the host galaxy, a minimum signal-to-noise ratio (S/N) of 4 in the polarization fraction is assumed. We assumed an expected polarization fraction of ~3% at the lowest-level total surface brightness of each galaxy, yielding an uncertainty polarization fraction of $\leqslant$0.75% across the final polarization map. Based on HAWC+ observations of M82 (Jones et al. 2019), NGC 1068 (Lopez-Rodriguez et al. 2020), and Centaurus A (Lopez-Rodriguez 2021), the host galaxy typically shows levels of polarization fraction of $\geqslant$3%. We took a conservative approach for the estimation of the lowest-level total surface brightness expected to be observed. The lowest total surface brightnesses that accomplish the above requirements are 0.053 Jy arcsec^{-2} at 53 μm, 0.016 Jy arcsec^{-2} at 89 μm, 0.005 Jy arcsec^{-2} at 154 μm, and 0.0029 Jy arcsec^{-2} at 214 μm. Objects in the Atlas of Galaxies with Herschel observations whose extended emission with a diameter of 2 kpc is lower than the surface brightness quoted above were removed from the final sample of this project.

The final sample (Table 1) is comprised of 17 bright and nearby ($\leqslant$20 Mpc) galaxies with a total execution time of 155.70 hr. We requested observations of 15 galaxies, as high-quality observations of the other two galaxies (i.e., M51 and Circinus) are already available. Of these 15 galaxies, nine are new, and we propose deeper and multiwavelength polarimetric observations of six galaxies to obtain high-quality data products to analyze the polarization spectra of the galaxies. In general, the large angular resolution, 18.″2 FWHM, achieved at 214 μm is insufficient to resolve the galactic structure in most of our targets. Thus, 214 μm was not requested, except for the starburst galaxies M82 and NGC 2146.

3.4. Observing Strategy

All of the observations in this program were performed using the newly implemented on-the-fly-mapping (OTFMAP) polarization mode with HAWC+. In Paper III (Lopez-Rodriguez et al. 2022), we described the data processing and presented the pipeline steps to obtain homogeneously reduced high-level data products of the galaxies in our sample. In summary, the OTFMAP observing strategy moves the telescope following a

[15] The Atlas of Galaxies observed with radio polarimetric observations can be found at https://atlas-of-galaxies.mpifr-bonn.mpg.de/introduction.
[16] The Herschel Archive can be found at http://archives.esac.esa.int/hsa/whsa/.
[17] The PHANGS project can be found at https://sites.google.com/view/phangs/home.
[18] THINGS project: https://www2.mpia-hd.mpg.de/THINGS/Data.html.
[19] The HST Archive can be found at https://archive.stsci.edu/missions-and-data/hst.
[20] SITE can be found at https://dcs.arc.nasa.gov/proposalDevelopment/SITE/index.jsp.

parametric curve (i.e., Lissajous curve) at a constant mapping speed within a specific scan size. For all observations, the objects are always within the field of view (FOV) of the HAWC+ array in any given band. This configuration maximizes the on-source time of the object. Table 2 shows the HAWC+ configuration per band used in this program. The most interesting result is that by using the OTFMAP polarization mode, we improved the observing overheads by a factor 2.34 and the sensitivity by a factor of 1.80 when compared to the commonly used C2N polarization mode. The OTFMAP is a significant optimization of the polarimetric mode of HAWC+, as it ultimately reduces the cost of operations of SOFIA by increasing the science collected per hour of observation up to an overall factor of 2.49. All observations of galaxies except for M51 were and will be performed using the OTFMAP polarimetric mode of HAWC+ (Paper III).

The final data products contain the Stokes *IQU*, polarization fraction (*P*), PA of polarization, and PI and its associated uncertainties with a pixel scale equal to the detector pixel scale (i.e., Nyquist sample) in any given band. The polarization fraction has been debiased and corrected by instrumental polarization and polarization efficiency. The released files have the same format as shown in Table 2 of Gordon et al. (2018). We point the reader to Paper III for a full description of the observing strategy and data reduction of the data release. All data sets are available on the Legacy Program website.[21]

Note that at the time of writing the original SOFIA Legacy Program proposal, the OTFMAP polarization mode was under commissioning as part of an engineering time proposal for HAWC+. With the expectation that the OTFMAP polarization mode would improve the sensitivity of the polarimetric observations, the estimated on-source times were a conservative estimation for each galaxy. As part of the Legacy Program, we characterized the OTFMAP polarization mode for objects with an extension within the FOV of the array in any given band of HAWC+ (Paper III). As shown in Paper III, the OTFMAP polarization mode overperforms the C2N polarimetric mode. The delivered data products have better image and polarimetric quality than those that would have been originally requested using the C2N polarization mode.

Table 3
Status of Released Galaxy Sample

Galaxy	Band	Requested Time[b]	Observed Time[b]	Completed[a]
	(μm)	(hr)	(hr)	
(1)	(2)	(3)	(4)	(5)
Centaurus A	89	⋯	0.89	⋯
Circinus	53	⋯	0.11	⋯
	89	⋯	0.89	⋯
	214	⋯	0.29	⋯
M51	154	⋯	2.78	⋯
M82	53	2.00	1.60	✓
	89	2.00	1.65	✓
	154	2.00	1.99	✓
	214	2.00	1.13	✓
M83	154	6.80	6.60	✓
NGC 253	89	3.00	1.00	33%
	154	5.00	0.89	18%
NGC 1068	53	3.07	1.06	35%
	89	7.07	2.00	28%
NGC 1097	53	⋯	1.87	⋯
	154	⋯	0.27	⋯
NGC 2146	53	3.00	1.60	53%
	89	3.00	2.02	67%
	154	3.00	2.40	80%
	214	3.00	2.33	✓
NGC 3627	154	6.80	4.53	67%
NGC 4736	154	6.80	2.22	33%
NGC 4826	89	6.80	1.22	18%
NGC 6946	154	6.80	7.20	✓
NGC 7331	154	6.80	6.10	✓

Notes. The columns are as follows: (1) galaxy name, (2) central wavelength of the band in microns, (3) requested on-source time in hours, (4) observed on-source time in hours, and (5) completed fraction per object per band.
[a] The observations are considered as completed (i.e., ✓) when (a) completion is >85% or (b) a desired S/N was reached. The observations from other SOFIA programs are shown with ellipses.
[b] On-source times. The observing overheads are 1.08 for the OTFMAP observations (Section 3.4) and 2.59 for the C2N observations of M51 (Borlaff et al. 2021). The observations from other SOFIA programs are shown with ellipses.

4. First Results

This first data release comprises 33% (51.34 out of 155.70 hr) of the awarded total exposure time of the SOFIA Legacy Program taken from 2020 January to 2021 November (Lopez-Rodriguez et al. 2022, Paper III). Table 3 shows the current status of the released observations. We recently published the results of M51 (Borlaff et al. 2021, Paper I) and NGC 1097 (Lopez-Rodriguez et al. 2021b, Paper II). Here we present the new data products associated with this data release with the goal of quantifying general trends in the polarization fraction of the galaxies in our sample. The characterization of the B-field orientation is presented in Paper V of the series.

4.1. Polarization Fraction of Galaxies

Figure 1 shows the polarization maps of the galaxies. For all galaxies, the color scale shows the surface brightness of the HAWC+ observations with overlaid polarization measurements. The length of the polarization fraction measurements is proportional to $\sqrt{P}$ (for visualization purposes), where a legend of 5% is shown for reference. The polarization measurements with $\mathrm{PI}/\sigma_{\mathrm{PI}} \geqslant 3.0$ and $P \leqslant 20\%$ were selected for all galaxies with varying I/σ_I criteria, as shown in Appendix A, where σ_{PI} and σ_I are the uncertainties per pixel of the polarized flux density and Stokes *I*, respectively. The maximum polarization fraction of $P = 20\%$ is given by the maximum polarization fraction, 19.8%, measured by Planck observations (Planck Collaboration et al. 2015). The polarization maps with a length proportional to the polarization fraction and the coordinate system of individual galaxies are shown in Appendix A (Figures 11–24). Figure 2 shows the histograms of the polarization fraction in bins of 1% for all individual polarization measurements per galaxy per band.

We estimate the median of the polarization fraction measurements, $\langle P^{\mathrm{hist}} \rangle$, per galaxy and per band as

$$\langle P^{\mathrm{hist}} \rangle = \frac{\sqrt{\langle Q^2 + U^2 - \sigma_Q \sigma_U \rangle}}{\langle I \rangle} \quad (1)$$

for all individual measurements shown in Figure 1, where $\langle I \rangle$ is the median of the Stokes *I*, and σ_Q and σ_U are the uncertainties

[21] SALSA data products are available at http://galmagfields.com/#data-section.

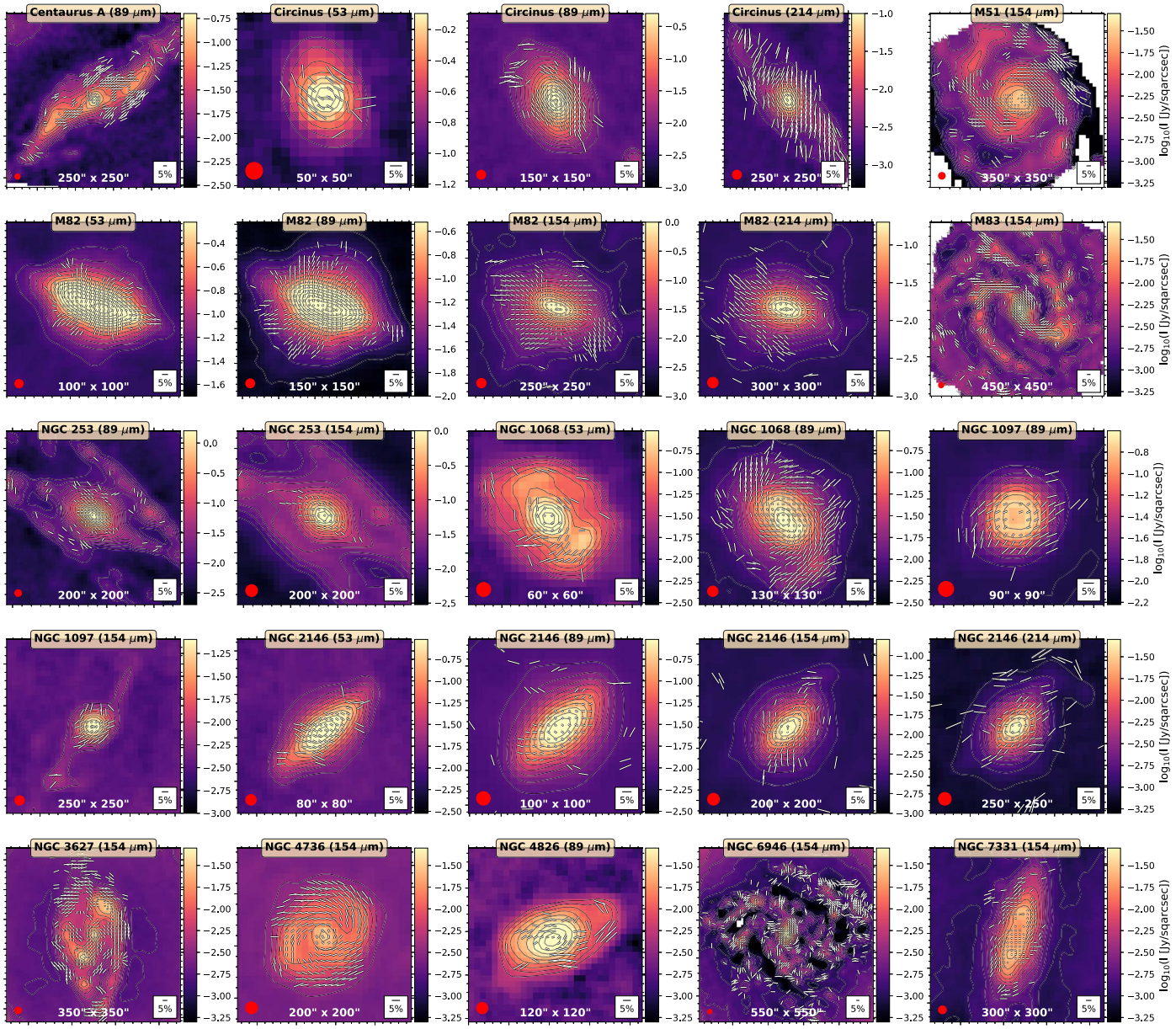

Figure 1. Polarization maps of galaxies. The surface brightness (color scale) is in logarithmic scale with contours starting at 5σ and increasing in steps of $2^n\sigma$, with $n = 5, 5.5, 6, ...$ The polarization fraction measurements (white lines) increase as $\sqrt{P}$ (for visualization purposes), with a legend of 5% shown at the bottom right of each panel. The polarization measurements with $\mathrm{PI}/\sigma_{\mathrm{PI}} \geqslant 3.0$, $P \leqslant 20\%$ were selected. We also performed quality cuts at several levels of I/σ_I as shown in Appendix A. The FOV and beam size (red circle) are shown at the bottom middle and left of each panel, respectively. Appendix A shows the polarization fraction measurements in linear scale with the coordinates of each galaxy over the total and polarized surface brightness.

per pixel of the Stokes QU. The 1σ uncertainty is estimated as the standard deviation of the histogram (Figure 2).

Since the expected polarization fraction from an unresolved galaxy may be scientifically useful, we estimate the integrated polarization fraction per galaxy and per band. To account for the vector quantity of the polarization measurements, we estimate the integrated polarization fraction, $\langle P^{\mathrm{int}} \rangle$, of each galaxy as

$$\langle P^{\mathrm{int}} \rangle = \frac{\sqrt{\langle Q \rangle^2 + \langle U \rangle^2 - \mathrm{bias}}}{\langle I \rangle}, \quad (2)$$

where $\langle I \rangle$, $\langle Q \rangle$, and $\langle U \rangle$ are the median of the Stokes IQU for pixels with $I/\sigma_I \geqslant 20$, and the bias is the standard error of the median using the uncertainties of the Stokes QU, σ_Q and σ_U, for these pixels. The $\langle P^{\mathrm{hist}} \rangle$ and $\langle P^{\mathrm{int}} \rangle$ are shown in Figure 3, and the tabulated data can be found in Appendix B (Table 5).

For all galaxies, we find that the individual measurements of the polarization fraction range from 0% to 15% (Figure 2). The galaxies with the lowest median polarization fraction measurements are the starburst galaxies M82, NGC 253, and NGC 2146 (Figure 2 and Table 5). The highest polarization fraction measurements are found in the interarms and outskirts of spiral galaxies. The spiral galaxies have the lowest polarization fractions colocated with star-forming regions across the galaxy's disk.

We use our 50–220 μm polarimetric observations to compute the polarized spectra of galaxies. Figure 4 shows the polarized spectra of all galaxy types, as well as spiral and starburst galaxies separately. Table 4 shows the estimated

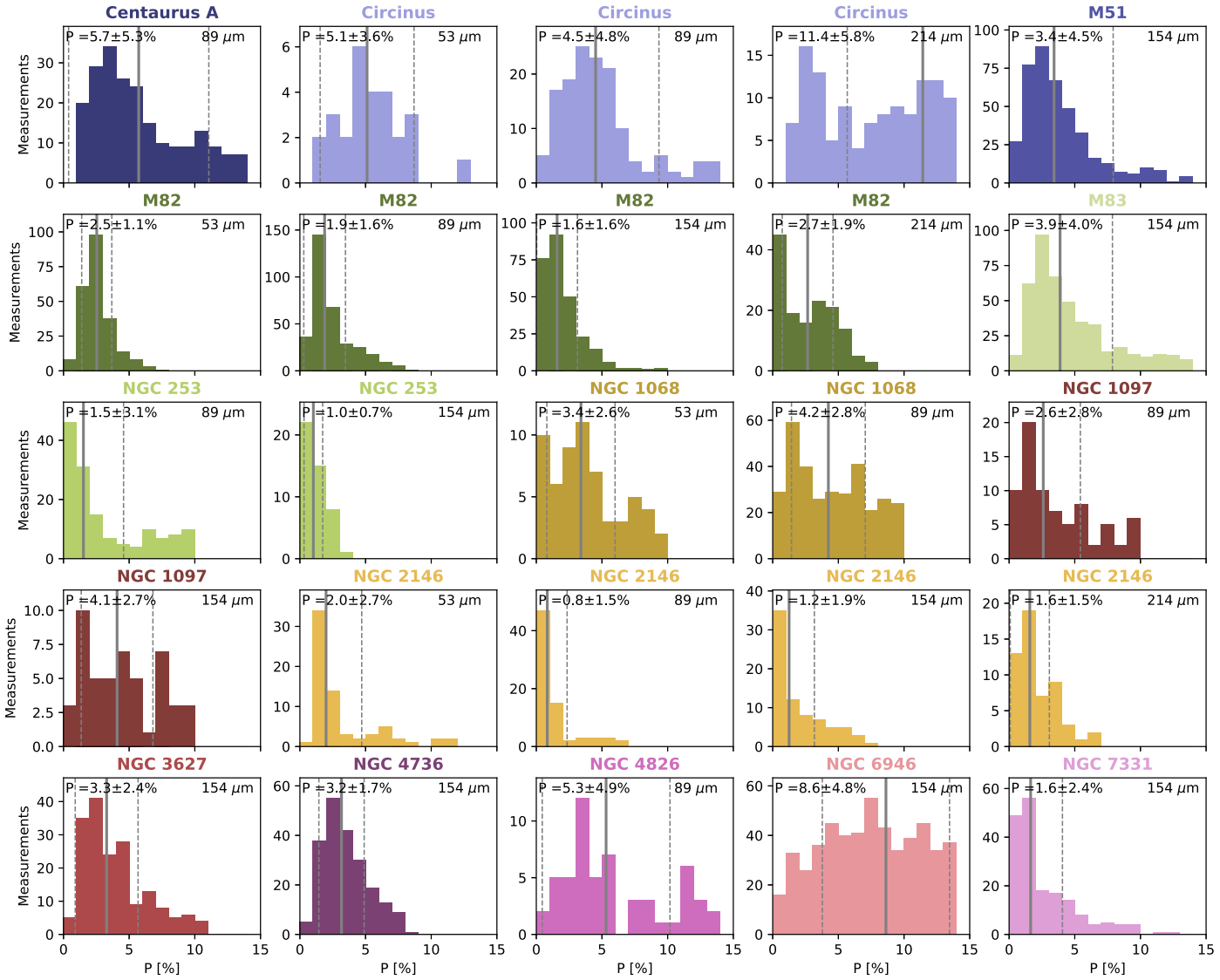

Figure 2. Histograms of the polarization fractions per galaxy per band. The histograms employ 1% bins, each galaxy is shown in a unique color, and the median $\langle P^{\rm hist}\rangle$ (gray solid line; Equation (1)) and 1σ uncertainty (gray dashed line) are shown. The median values displayed in the top right corners are also provided in Table 5.

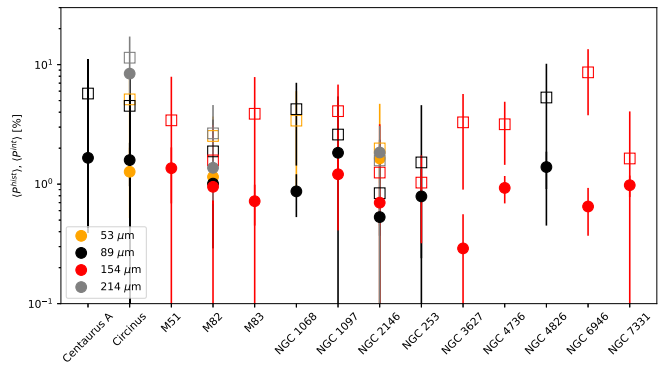

Figure 3. Median and integrated polarization fractions of galaxies. Polarization fractions from individual measurements, $\langle P^{\rm hist}\rangle$ (open squares; Equation (1)), and the integrated Stokes IQU, $\langle P^{\rm int}\rangle$ (filled circles; Equation (2)), are shown. Tabulated values are shown in Table 5.

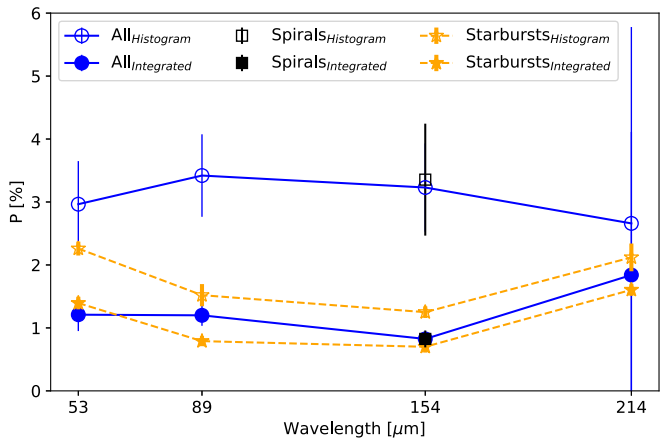

Figure 4. Polarized spectra of galaxies. Shown are the polarization fraction as a function of the wavelength in the range of 50–220 μm for all galaxies (blue circles with solid line), spirals (black squares), and starbursts (orange stars with dashed line) in our sample. The median polarization fraction from the individual measurements (open symbols) across the galaxy and the integrated polarization fraction from the Stokes IQU (filled symbols) are shown. See the legend for a description and Table 4 for measurements.

polarization fractions per galaxy group and wavelength. We estimate the median of individual polarization fraction measurements for all galaxy types to be fairly constant, $\langle P^{\rm hist}_{\rm all,50-220\mu m}\rangle = 3.1 \pm 0.3\%$, across the 50–220 μm

Table 4
Median and Integrated Polarization Fraction per Band of the Full Galaxy Sample and Spiral and Starburst Galaxies

Band (μm) (1)	Galaxy Type (2)	$\langle P^{\rm hist}\rangle$ (%) (3)	$\langle P^{\rm int}\rangle$ (%) (4)
53	All	2.9 ± 0.7	1.3 ± 0.1
	Starbursts[a]	2.3 ± 0.1	1.4 ± 0.1
89	All	3.4 ± 0.7	1.2 ± 0.2
	Starbursts	1.5 ± 0.2	0.8 ± 0.1
154	All	3.3 ± 0.7	0.9 ± 0.1
	Spirals[b]	3.3 ± 0.9	0.8 ± 0.1
	Starbursts	1.3 ± 0.1	0.7 ± 0.1
214	All	2.7 ± 3.1	1.8 ± 2.3
	Starbursts	2.1 ± 0.2	1.6 ± 0.1

Notes. The columns are as follows: (1) central wavelength of the band in microns, (2) galaxy type, (3) median polarization fraction based on individual measurements, and (4) integrated polarization fraction within the full disk of galaxies.
[a] Polarization fraction for the starburst galaxies M82, NGC 253, and NGC 2146.
[b] Polarization fraction for the spiral galaxies M51, M83, NGC 3627, NGC 4736, NGC 6946, and NGC 7331.

wavelength range (Figure 4, blue open circles with solid line; Table 4). The $\langle P^{\rm hist}_{\rm all,50-220\mu m}\rangle$ was estimated using the median of the Stokes *IQU* at each wavelength. The largest uncertainty is found at 214 μm and driven by the small galaxy sample (three galaxies: Circinus, M82, and NGC 2146). Large polarization fractions, $\geqslant$8%, are measured along the bar of Circinus (Figure 1), while M82 and NGC 2146 show $\langle P^{\rm hist}\rangle = 1.6\%$ and 2.7% at 214 μm, respectively (Figure 2; Table 5). The median integrated polarization fraction for all galaxy types also remains constant $\langle P^{\rm int}_{\rm all,50-220\mu m}\rangle = 1.3 \pm 0.2\%$ across the 50–220 μm wavelength range (Figure 4, blue filled circles with solid line; Table 4). The $\langle P^{\rm int}_{\rm all,50-220\mu m}\rangle$ was estimated using the median of the Stokes *IQU* at each wavelength.

We separate the sample in the starburst galaxies (M82, NGC 253, and NGC 2146) at all wavelengths and the spiral galaxies (M51, M83, NGC 3627, NGC 4736, NGC 6946, and NGC 7331) at 154 μm. Then, we estimate the median of the individual polarization fractions, $\langle P^{\rm hist}\rangle$, and the integrated polarization fraction across the full disk of the galaxies, $\langle P^{\rm int}\rangle$ (Table 4).

For starburst galaxies, we find that the polarized spectrum varies as a function of wavelength with a minimum located in the range of 89–154 μm (Figure 4, orange dashed line). The variation of the polarization spectra of starbursts is measured for both $\langle P^{\rm hist}_{\rm starburst}\rangle$ within the range of [1.3, 2.3]% and $\langle P^{\rm int}_{\rm starburst}\rangle$ within the range of [0.7, 1.6]%. This result represents the first polarized spectrum of starburst galaxies in the FIR wavelength range. We discuss this result in Section 5.2.

The spiral galaxies have a median polarization fraction of $\langle P^{\rm hist}_{\rm spirals,154\mu m}\rangle = 3.3 \pm 0.9\%$ (Figure 4, black square dot at 154 μm). This value is more than a factor of 2 larger than the median polarization fraction of starbursts, $\langle P^{\rm hist}_{\rm starburst,154\mu m}\rangle = 1.3 \pm 0.1\%$, at 154 μm. This result causes the 50–220 μm polarized spectrum to appear flat when accounting for all galaxy types (Figure 4, blue open circles with solid line). This is an effect of how $\langle P^{\rm hist}\rangle$ is measured. When the polarization fraction is measured using the integrated intensities of the Stokes *IQU* within the disk, the integrated polarization fraction of spiral galaxies is measured to be $\langle P^{\rm int}_{\rm spirals,154\mu m}\rangle = 0.8 \pm 0.1\%$ at 154 μm. This value is comparable to the integrated polarization fraction, $\langle P^{\rm int}_{\rm starburst,154\mu m}\rangle = 0.7 \pm 0.1\%$ at 154 μm, of the starburst galaxies (Figure 4 and Table 4). The main reason for the decrease in polarization fraction from $\langle P^{\rm hist}_{\rm spirals,154\mu m}\rangle$ to $\langle P^{\rm int}_{\rm spirals,154\mu m}\rangle$ is the vector-like nature of the polarization measurements. The net polarization fraction tends to nullify the integrated polarization fraction due to (a) the spiral pattern measured in spiral galaxies and (b) the several polarization components (i.e., outflow and disk) measured in starburst galaxies.

4.2. Polarization Fraction and Column Density Relation

The polarization fraction in galaxies has been found to decrease with the total surface brightness at FIR wavelengths and column density, $N_{\rm H}$ (Jones et al. 2019; Lopez-Rodriguez et al. 2020; Jones et al. 2020; Lopez-Rodriguez et al. 2021a, 2021b; Lopez-Rodriguez 2021; Borlaff et al. 2021). The $P \propto N_{\rm H}^{\alpha}$ relation arises from the separation of ordered and random (i.e., turbulent and/or tangled) B-fields in the ISM (e.g., Jones et al. 1992; Planck Collaboration et al. 2016). For the maximally aligned dust grains, P is constant with $N_{\rm H}$, i.e., $P \propto N_{\rm H}^{0}$. Any variation of the B-field orientation results in a decrease of the polarization fraction with column density. If the B-field orientation varies completely randomly along the LOS, then $P \propto N_{\rm H}^{-0.5}$. For any combination of random and ordered B-fields, the slope is between these two. The P can decrease faster than -0.5 (e.g., King et al. 2019) due to (a) a decrease of dust grain alignment efficiency toward denser regions, (b) tangled B-fields along the LOS, and/or (c) an increase in turbulence at scales smaller than the beam of the observations. Thus, the $P - N_{\rm H}$ relation can be used as a proxy to estimate the random B-fields in the ISM.

Figure 5 serves as an illustration of the several physical mechanisms (turbulence, tangled B-fields, dust grain alignment efficiency, and isotropic random B-fields) responsible for the dependence between the polarization fraction and the column density. This figure shows the summary of the main results of this work, and we will refer the reader to Figure 5 in this and the following sections.

We use the column density, $N_{\rm HI+H_2}$, estimated using the fitting of a modified blackbody function to the 70–250 μm Herschel images. Appendix A describes the details of the estimation of the column density, and we show the maps with overlaid polarization measurements. We use the dependence with $N_{\rm HI+H_2}$, as it provides a physical quantification of the ISM and can be compared with the results of the Milky Way and other galaxies. Figure 6 shows the total and polarized surface brightness and polarization fraction as a function of the column density, $N_{\rm HI+H_2}$, for a subsample of the galaxies at 154 μm. The rest of the plots are shown in Appendix C (Figures 25–27). For all galaxies, we use the same polarization measurements shown in Section 4.1.

The $P - N_{\rm HI+H_2}$ plots show a more complex relation than a single power law. To characterize the $P - N_{\rm HI+H_2}$ relations, we use a broken power law with two power-law indexes at a cutoff

column density such as

$$P(N_{\rm HI+H_2}) = P_0 \begin{cases} \left(\frac{N_{\rm HI+H_2}}{N^{\rm c}_{\rm HI+H_2}}\right)^{\alpha_1} & N_{\rm HI+H_2} \leqslant N^{\rm c}_{\rm HI+H_2} \\ \left(\frac{N_{\rm HI+H_2}}{N^{\rm c}_{\rm HI+H_2}}\right)^{\alpha_2} & N_{\rm HI+H_2} > N^{\rm c}_{\rm HI+H_2} \end{cases}, \quad (3)$$

where P_0 is the scale factor, $N^{\rm c}_{\rm HI+H_2}$ is the cutoff of the broken power law, and α_1 and α_2 are the power-law indexes before and after the break, respectively. Note that several galaxies (e.g., M82 at 53 μm, M83 at 154 μm, and NGC 1068 at 89 μm) show more complex trends than a broken power law; however, a detailed analysis of each galaxy will be the subject of future projects. Here we focus on the general trends of the full galaxy sample.

We have four free model parameters: P_0, $N^{\rm c}_{\rm HI+H_2}$, α_1, and α_2. We perform a Markov Chain Monte Carlo (MCMC) approach using the differential evolution metropolis sampling step in the PYTHON code PYMC3 (Salvatier et al. 2016). The prior distributions are set to flat within the range of $P_0 = [0, 15]\%$, $N^{\rm c}_{\rm HI+H_2} = [N^{\rm min}_{\rm HI+H_2}, N^{\rm max}_{\rm HI+H_2}]$ cm^{-2}, where $N^{\rm min}_{\rm HI+H_2}$ and $N^{\rm max}_{\rm HI+H_2}$ are the minimum and maximum column density values of each galaxy in any given band, $\alpha_1 = [-1, 0]$ and $\alpha_2 = [-1, 0]$. We run the code using five chains with 10,000 steps and an extra 5000 burn-in per chain, which provides 50,000 steps for the full MCMC code useful for data analysis. The best inferred model with the associated 1σ uncertainty is plotted for a subset of our sample in Figure 6 and for each source in Appendix C (Figures 25–27). Figure 7 shows α_1 for all galaxies and α_2 and cutoff column densities, $N^{\rm c}_{\rm HI+H_2}$, for galaxies with a broken power law. The tabulated values can be found in Appendix B (Table 6).

For all galaxies, the polarization fraction varies across the column density range of $\log_{10}(N_{\rm HI+H_2}[{\rm cm}^{-2}]) = [19.96, 22.91]$. The highest polarization fractions, $\geqslant$10%, are found at the lowest column density ranges, $\log_{10}(N_{\rm HI+H_2}[{\rm cm}^{-2}]) \leqslant 21$. We find three main groups based on the fitting results of the $P - N_{\rm HI+H_2}$ relations (Figure 5). We describe the characteristics of each group below.

Group 1 is characterized by a flatter power law, $\alpha_2 > \alpha_1$, after the cutoff column density. Galaxies in this group are Circinus at 214 μm, M83 at 154 μm, and M82 at all bands. We estimate α_1 in the range of $[-0.99, -0.65]$ with a median of -0.91 ± 0.12, α_2 in the range of $[-0.51, -0.13]$ with a median of -0.33 ± 0.11, and a cutoff column density, $\log_{10} N^{\rm c}_{\rm HI+H_2}[{\rm cm}^{-2}]$, in the range of [21.09, 22.04] with a median of 21.59 ± 0.31 (Figures 5 and 7). Figures 6 and 25 show that the flatter α_2 is due to a faster increase of the PI compared to the total intensity after the cutoff column density. For a visualization of the spatial region associated with both power laws, the cutoff column density, $N^{\rm c}_{\rm HI+H2}$, is displayed over the column density maps in Appendix A. We find that the second power law is required for the central starburst M82, the inner bar, and the inflection regions between the inner bar and the spiral arms of M83, and the starburst ring of Circinus.

Group 2 is characterized by a steeper power law, $\alpha_2 < \alpha_1$, after the cutoff column density. Galaxies in this group are M51, NGC 4736, NGC 6946, and NGC 7331 at 154 μm and NGC 1097 at 89 and 154 μm. We estimate α_1 in the range of $[-0.49, -0.06]$ with a median of -0.39 ± 0.14, α_2 in the range of $[-1.0, -0.88]$ with a median of -0.99 ± 0.04, and a cutoff column density, $\log_{10} N^{\rm c}_{\rm HI+H_2}[{\rm cm}^{-2}]$, in the range of [20.61, 21.33] with a median of 20.86 ± 0.29 (Figures 5 and 7). Figures 6 and 26 show that the steeper α_2 is due to the faster increase of the total intensity compared to the PI after the cutoff column density. We find that a second power law is required for the central regions of galaxies associated with the galaxy's core and star-forming regions across the galaxy's disk (figures in Appendix A).

Group 3 is characterized by a single power law. Galaxies in this group are shown in Figures 5 and 27. We estimate α_1 in the range of $[-1.0, -0.43]$ with a median of -0.93 ± 0.17. The single power law is characterized by the increase of the total intensity while the polarized flux remains constant compared to the full range of column densities. However, we find several galaxies where the polarized flux varies at a similar rate as the total intensity, which keeps a single power law in $P - N_{\rm HI+H_2}$. These galaxies are Circinus, NGC 1068 at 89 μm, NGC 253 at 89 and 154 μm, and NGC 2146 at 53 and 89 μm. This change in PI occurs at the central star-forming regions of these galaxies. Figure 5 shows this behavior as a dashed green line in the$I - N_{\rm HI+H_2}$ and PI $- N_{\rm HI+H_2}$.

The physical mechanisms responsible for the trends described in each group are discussed in Section 5.1.

4.3. Polarization Fraction and Dust Temperature Relation

Draine & Weingartner (1996) computed that the dust temperature, $T_{\rm d}$, can be estimated as a function of the energy density of the radiation field, $u_{\rm rad}$, such as $T_{\rm d} \propto (u_{\rm rad}/u_{\rm ISM})^{1/(4+\beta)}$ K, where $u_{\rm ISM}$ is the radiation field in the ISM of the Milky Way, and β is the emissivity index. We took $\beta = 1.60$ (Appendix A), which yields $4 + \beta = 5.60$. Thus, we can use $T_{\rm d}$ as a proxy of the strength of the energy density of the radiation field producing the thermal emission from dust in the disk of galaxies. Specifically, we are interested in measuring the effect of the radiation field on the polarization efficiency within the disk of galaxies. We analyze the relation between the polarization fraction and the dust temperature, $P - T_{\rm d}$. Appendix A describes the details of the estimation of the dust temperature and shows the polarization maps over the dust temperature for the galaxies in our sample. Figure 5 shows the general trends found in the galaxy sample. Figure 6 shows the total and polarized surface brightness and polarization fraction as a function of the dust temperature of a representative galaxy at 154 μm in each group (the full sample is shown in Appendix C).

To characterize the $P - T_{\rm d}$ relations, we use a broken power law with two power-law indexes,

$$P(T_{\rm d}) = P_0^{T_{\rm d}} \begin{cases} \left(\frac{T_{\rm d}}{T^{\rm c}_{\rm d}}\right)^{\alpha_1^{T_{\rm d}}} & T_{\rm d} \leqslant T^{\rm c}_{\rm d} \\ \left(\frac{T_{\rm d}}{T^{\rm c}_{\rm d}}\right)^{\alpha_2^{T_{\rm d}}} & T_{\rm d} > T^{\rm c}_{\rm d} \end{cases}, \quad (4)$$

where $P_0^{T_{\rm d}}$ is the scale factor, $T^{\rm c}_{\rm d}$ is the cutoff dust temperature of the broken power law, and $\alpha_1^{T_{\rm d}}$ and $\alpha_2^{T_{\rm d}}$ are the power-law indexes before and after the cutoff, respectively. We have four free model parameters, $P_0^{T_{\rm d}}$, $T^{\rm c}_{\rm d}$, $\alpha_1^{T_{\rm d}}$, and $\alpha_2^{T_{\rm d}}$, that we fit using the same procedure described in Section 4.2 for the column density. Figure 8 shows $\alpha_1^{T_{\rm d}}$ for all galaxies and $\alpha_2^{T_{\rm d}}$ and cutoff

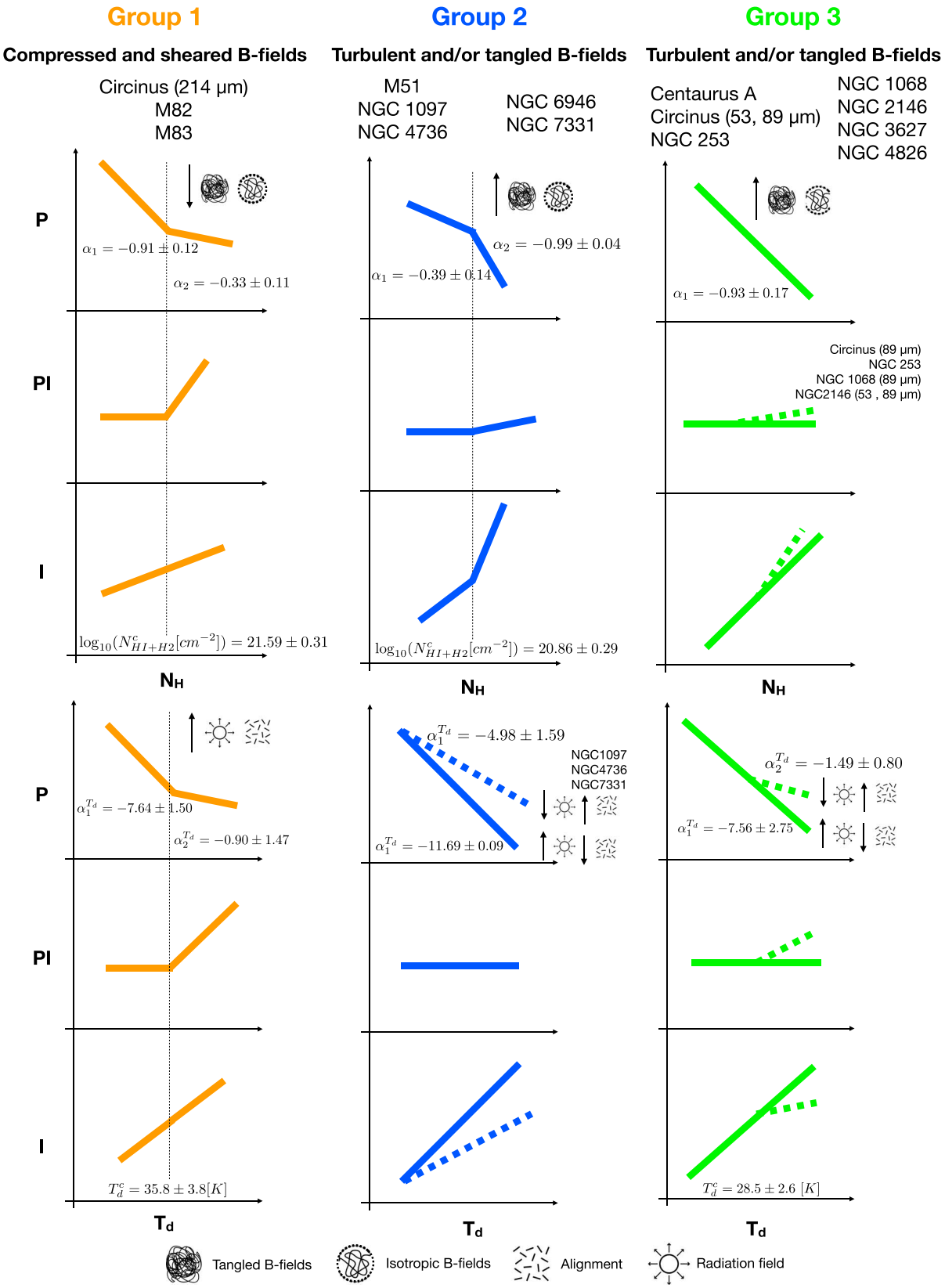

Figure 5. Summary of the trends in P, PI, and I as a function of column density, $N_{\rm H}$, and dust temperature, $T_{\rm d}$, and the physical mechanisms affecting their slopes. Three groups are identified, 1 (orange), 2 (blue), and 3 (green), with their associated galaxies shown at the top of each group. For each group, the $P - N_{\rm H}$ (first row), PI $- N_{\rm H}$ (second row), $I - N_{\rm H}$ (third row), $P - T_{\rm d}$ (fourth row), PI $- T_{\rm d}$ (fifth row), and $I - T_{\rm d}$ (sixth row) relations are shown. The median values of the power-law indexes and cutoff column density and dust temperature are shown in the $P - N_{\rm H}$ and $P - T_{\rm d}$ relations. The physical mechanisms producing the trends are shown for each group (legend at the bottom). These trends are based on the data shown in Appendix C (Figures 25–27) and described in Sections 4.2, 4.3, and 5.1.

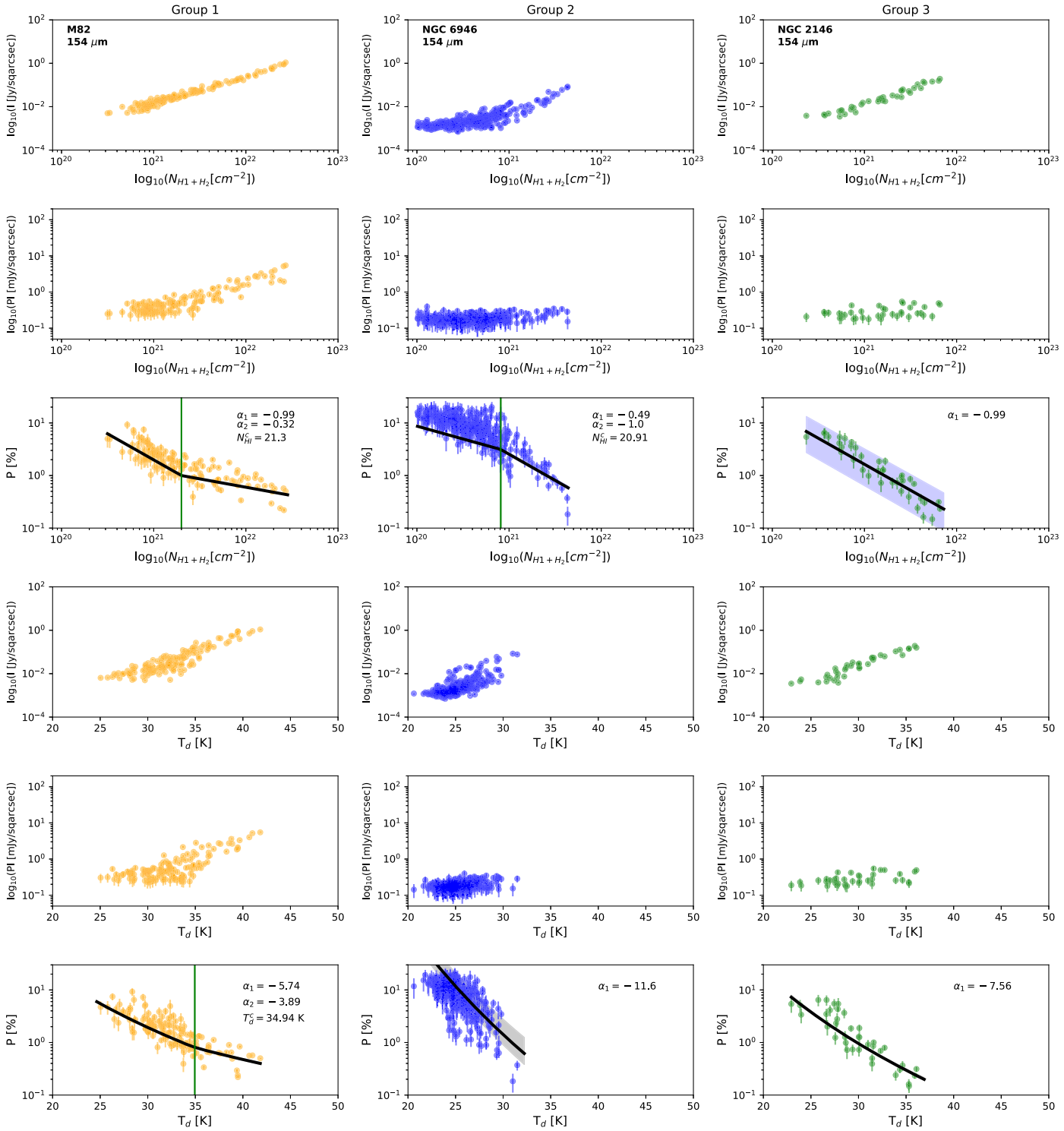

Figure 6. Example of the variations of P, PI, and I with $N_{\rm HI+H_2}$ and $T_{\rm d}$ for the three groups shown in Figure 5. The representative galaxies M82 for group 1 (left), NGC 6949 for group 2 (middle), and NGC 2146 for group 3 (right) are shown. The relations for all galaxies are shown in Appendix C (Figures 25–27). These trends are discussed in Sections 4.2, 4.3, and 5.1.

dust temperature,$T_{\rm d}^{\rm c}$, for galaxies with a broken power law. The tabulated values can be found in Appendix B (Table 6).

For all galaxies, we find that the polarization fraction varies across the dust temperature range of $T_{\rm d} = [19,\ 48]$ K. In general, we find that the polarization fraction decreases with increasing dust temperature. We find that the highest polarization fractions, $\geqslant$10%, are found at the lowest dust temperature ranges, $T_{\rm d} \leqslant 30$ K. The highest dust temperatures are colocated with the star-forming regions and have the lowest polarization fractions, <1%. We find the following trends for the $P - T_{\rm d}$ plots and discuss them together with the $P - N_{\rm HI+H2}$ relations in Section 5.1.

Group 1 is characterized by a flatter power law, $\alpha_2^{T_{\rm d}} > \alpha_1^{T_{\rm d}}$, after the cutoff dust temperature. We estimate $\alpha_1^{T_{\rm d}}$ in the range

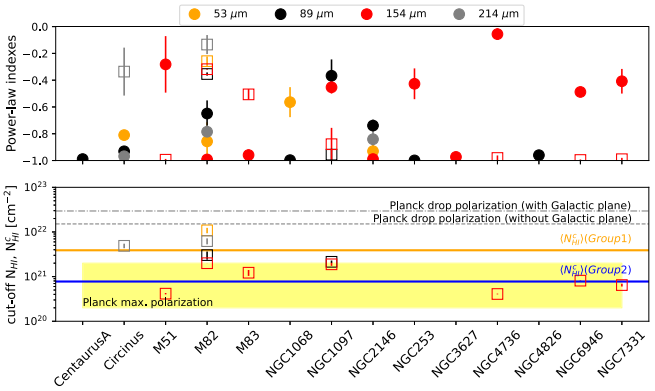

Figure 7. Power-law indexes (top) and cutoff column densities (bottom) for all galaxies based on the fitting of the $P - N_{\rm HI+H_2}$ relations. Top panel: first power-law, α_1 (filled circles), and second power-law, α_2 (open squares). Indexes at 53 (orange), 89 (black), 154 (red), and 214 (gray) μm are shown. Bottom panel: cutoff column densities, $N^{\rm c}_{\rm HI+H_2}$ (open squares), for galaxies with a broken power law. The median cutoff column densities of $\log_{10}(N^{\rm c}_{\rm HI+H_2}\,[{\rm cm}^{-2}]) = 21.59 \pm 0.31$ (orange solid line) and 20.86 ± 0.29 (blue solid line) for groups 1 and 2, respectively, are shown. The range of column densities (yellow shaded region) for the maximum polarization fraction and the column densities of $\log_{10}(N_{\rm H}\,[{\rm cm}^{-2}]) = 22.18$ (gray dashed line) and 22.47 (gray dashed–dotted line) associated with a sharp drop in the polarization fraction with and without the Galactic plane of the Milky Way observed by Planck (Planck Collaboration et al. 2015) are shown.

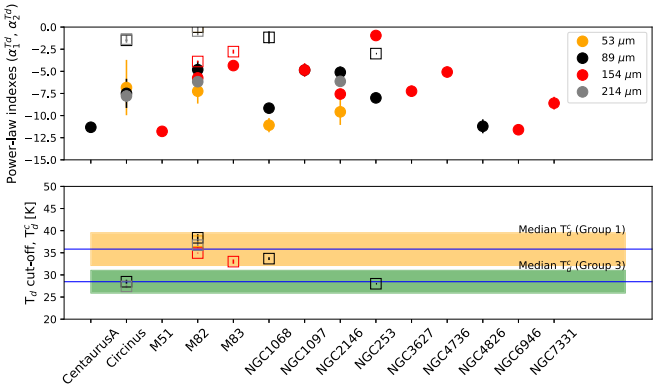

Figure 8. Power-law indexes (top) and cutoff dust temperatures (bottom) for all galaxies based on the fitting of the $P - T_{\rm d}$ relations. Top panel: first power-law, $\alpha_1^{T_{\rm d}}$ (filled circles), and second power-law, $\alpha_2^{T_{\rm d}}$ (squares), indexes at 53 (orange), 89 (black), 154 (red), and 214 (gray) μm. Bottom panel: cutoff dust temperatures, $T^{\rm c}_{\rm d}$ (squares), for galaxies and wavelengths with a broken power law. The median cutoff dust temperatures of $T^{\rm c}_{\rm d} = 35.8 \pm 3.8$ (orange) and 28.5 ± 2.6 K (green) and 1σ uncertainty (shaded region) for groups 1 and 3, respectively, are shown.

of $[-7.78, -4.35]$ with a median of -7.64 ± 1.50, $\alpha_2^{T_{\rm d}}$ in the range of $[-3.89, -0.01]$ with a median of -0.90 ± 1.47, and a median $T^{\rm c}_{\rm d} = 35.8 \pm 3.8$ K in the range of [27.4, 38.4] K (Figure 8). Figures 5 and 25 show that a flatter $\alpha_2^{T_{\rm d}}$ is due to the faster increase of the PI compared to the total intensity after the cutoff dust temperature. We find that the second power law is required for the regions associated with starburst regions and low polarization fractions, $P_0^{T_{\rm d}} \leqslant 1\%$ (Appendix A).

Group 2 is characterized by a single power law. We estimate $\alpha_1^{T_{\rm d}}$ in the range of $[-11.78, -4.85]$ with two different subgroups based on their slopes (Figure 5 and 26). Objects M51 and NGC 6946 have a steeper slope, $\alpha_1^{T_{\rm d}} = -11.69 \pm 0.09$, than NGC 1097, NGC 4736, and NGC 4826, $\alpha_1^{T_{\rm d}} = -4.98 \pm 1.59$. The single power law is characterized by the increase of total intensity, while the polarized flux remains constant across the full range of dust temperatures.

Group 3 is also characterized by single power law with a median of $\alpha_1^{T_{\rm d}} = -7.56 \pm 2.75$ in the range of $[-11.32, -0.95]$. The exceptions are Circinus, NGC 253, and NGC 1068 at 89 μm. These galaxies have a broken power law with a median $\alpha_2^{T_{\rm d}} = -1.49 \pm 0.80$ in the range of $[-3.0, -1.16]$ and a median $T^{\rm c}_{\rm d} = 28.5 \pm 2.6$ K in the range of [28.0, 33.7] K. We find that the second power law is associated with the central $\sim$1 kpc of the galaxies cospatial with star-forming regions in Circinus and NGC 253 and the hot environment surrounding the active galactic nucleus of NGC 1068.

The physical mechanisms responsible for the trends described for each group are discussed in Section 5.1.

5. Discussion

5.1. Relative Contribution of the Ordered and Random B-fields

We have identified three groups based on the $P - N_{\rm HI+H_2}$ relation (Section 4.2). In general, we found a decrease in polarization fraction with increasing column density. As described in Section 3.1, a maximum polarization is measured in the absence of tangled B-fields along the LOS, turbulence, and/or inclination effects. Under these "perfect" conditions, the polarization fraction should be expected to be constant with column density due to a dominant ordered B-field within the beam of the observations. Assuming that the galaxy disk is at a constant inclination and no other inclination effects are important, a decrease in polarization fraction with increasing column density is attributed to an increase in turbulent and/or tangled B-fields along the LOS (i.e., random B-fields) within the beam of the observations. The inclination effects on the polarization fraction are discussed in Section 5.3. We use the $P - N_{\rm HI+H_2}$ plots as a proxy for the relative contribution of the random-to-ordered B-fields within the beam of the observations.

We found a similar slope of $\sim$0.9 for low column densities, $N_{\rm HI+H_2} < N^{\rm c}_{\rm HI+H_2}$, in galaxies with a broken power law in group 1; at high column densities, $N_{\rm HI+H_2} > N^{\rm c}_{\rm HI+H_2}$, in galaxies with a broken power law in group 2; and at all column densities, $\log_{10}(N_{\rm HI+H_2}\,[{\rm cm}^{-2}]) = [19.96, 22.91]$, in galaxies with a single power law (group 3).

Using the $P - T_{\rm d}$ relation, we find that $\alpha_1^{T_{\rm d}} \sim -7$, within the uncertainties, for the three groups identified in this galaxy sample. For the galaxies with a broken power law, we find that $\alpha_2^{T_{\rm d}} \sim -1$, within the uncertainties, independently of the group. These results indicate that the $P - T_{\rm d}$ relation is not sensitive to the physical conditions of the B-fields in the galaxy's disk but rather to the ISM conditions (i.e., radiation field). The $P - T_{\rm d}$ relation provides information about the polarization efficiency toward star-forming regions.

We now discuss the trends of each group based on the relative contribution of the ordered and random (i.e., turbulent and/or tangled) B-fields and dust grain alignment efficiency. We refer the reader to the summary of these trends shown in Figure 5.

5.1.1. Group 1: Compressed and/or Sheared B-fields

Group 1 has a flatter power law after the cutoff column density and dust temperature. This is a result of a faster increase

in PI than in total intensity (Figures 5 and 25). This result is interesting because, a priori, it may indicate that the relative contribution of turbulence and/or tangled B-fields along the LOS (i.e., random B-fields) is smaller in the regions associated with α_2 than in the regions with α_1 or that the relative contribution of an ordered B-field is larger. The regions associated with α_2 are spatially correlated with the central starburst of M82, the inner bar and the inflection regions between the inner bar and the spiral arms of M83, and the starburst ring of Circinus. These areas are typically associated with regions of higher turbulence and/or tangled B-fields along the LOS than those in the diffuse ISM of galaxies. This result indicates that another physical mechanism may be flattening the $P - N_{\rm HI+H2}$ and $P - T_{\rm d}$ relations.

For M82, Lopez-Rodriguez et al. (2021b) showed that the turbulent kinetic and magnetic energies are in close equipartition within the central ∼2 kpc radius of the starburst. Using 53 μm polarimetric observations, these authors estimated a median turbulent B-field strength of ∼300 μG. The B-field orientation is parallel to the galactic outflow with an angular dispersion of $17\overset{\circ}{.}1$. Although M82 may have small-scale random B-fields in the outflow within the beam of the observations, the dominant component is the ordered B-field driven by the turbulent kinetic energy of the galactic outflow. The ordered B-field has a coherence length ($\delta = 73.6 \pm 5.6$ pc, $3\overset{''}{.}99 \pm 0\overset{''}{.}30$) larger than the beam of the observations. The 53 μm polarimetric observations are sensitive to the compressed B-fields along the galactic outflow. For M83, Frick et al. (2016) showed that the measured B-fields may be dominated by the mean-field dynamo at a resolution of 520 pc (12″) using 6–13 cm polarimetric observations. These authors concluded that the measured B-fields are compressed and partially aligned with the material arms in the galaxy. Circinus has a starburst ringlike structure with a diameter of ∼350 pc (∼21″) in ^{12}CO(1–0) (Elmouttie et al. 1998) and ∼1 kpc (∼61″) in H I (Jones et al. 1999). A compressed B-field may be present within the central 1 kpc of Circinus driven by galactic shock dynamics in the inner bar and starburst ring. This environment may be similar to that found in the central 1 kpc of NGC 1097 using HAWC+ observations (Lopez-Rodriguez et al. 2021b).

We interpret the flatter α_2 found in group 1 as follows. After the cutoff column density, $\log_{10}(N^{\rm c}_{\rm H+H_2}[{\rm cm}^{-2}]) \geqslant 21.59 \pm 0.31$, and dust temperature, $T^{\rm c}_{\rm d} \geqslant 35.8 \pm 3.8$ K, the relative contribution of the ordered B-field of these galaxies increases faster than the random B-field component. This result is based on the fact that the B-field structure associated with α_2 has a dominant large-scale B-field with low angular dispersion from beam to beam. The enhancement of the ordered B-fields may be produced by compression or shear in high-density and high dust temperature regions of the galaxy associated with galactic outflows and starburst rings. This scenario drives a faster increase in PI than in *I*. The physical reason is that compressed B-fields produce a relative decrease of the isotropic B-fields (i.e., an increase in anisotropic B-fields), yielding an increment of PI.

The $P - T_{\rm d}$ relation may be explained as a change in the dust alignment efficiency based on RATs (Hoang & Lazarian 2016). The polarization fraction depends on the minimum size of the aligned dust grains, $a_{\rm align}$. Hoang (2021) provided an analytical function of $a_{\rm align}$ as a function of the volume density, $n_{\rm H}$, and dust temperature as $a_{\rm align} \propto n_{\rm H}^{2/7} T_{\rm d}^{-12/7}$. Higher polarization fractions are expected for smaller values of $a_{\rm align}$ due to the fact that the size distribution of aligned dust grains is broader. For the galaxies within this group, our results indicate that $\alpha_2^{T_{\rm d}}$ is flatter than $\alpha_1^{T_{\rm d}}$ after the cutoff dust temperature of $T^{\rm c}_{\rm d} = 37.8 \pm 3.8$ K. This behavior may indicate a faster increase of $T_{\rm d}$ than the column density, which increases the alignment size, $a_{\rm align}$. The increase in dust grain alignment efficiency produces a flatter $P - T_{\rm d}$ relation. An enhancement of the dust grain alignment efficiency may be spatially located along the compression and/or shear in high-density and high-temperature regions.

5.1.2. Group 2: Random B-fields and Dust Grain Alignment Efficiency

Group 2 has a steeper power law after the cutoff column density in $P - N_{\rm HI+H_2}$ and a single power law in the $P - T_{\rm d}$ relation. For the $P - N_{\rm HI+H_2}$ relation, this is a result of a faster increase in total intensity than in PI (Figures 5 and 26). We find that α_2 is spatially associated with the spiral arms of M51, the star-forming regions in NGC 6946, and the central ∼1 kpc starburst rings of NGC 1097, NGC 4736, and NGC 7331. For the $P - T_{\rm d}$ relation, a single power law is the result of a constant PI with increasing *I*.

A study of the FIR–radio correlation in NGC 6946 showed that the star formation rate surface density is correlated with the turbulent B-field, $B_{\rm tur} \propto \Sigma_{\rm SFR}^{0.16\pm0.01}$ (Tabatabaei et al. 2013). This result indicates that the increase of the gas turbulence associated with the star-forming regions is correlated with an increase of the isotropic random B-field. Supernova explosions increase turbulence in the ISM, which amplifies the B-field strength via fluctuation dynamo (Section 2.4). In addition, the synchrotron PI is spatially located in the interarm regions of M51 and NGC 6949 (Beck 2007; Fletcher et al. 2011). This result has been explained due to the fact that the B-fields in the arms are more turbulent when compared to those in the interarms. Borlaff et al. (2021) measured a relative increase of turbulent B-fields in the spiral arms of M51. The increase of turbulent B-fields is associated with regions of high column density and turbulent kinetic energy traced by the ^{12}CO(1–0) molecular gas. Furthermore, the star formation rate was found to be uncorrelated with the FIR polarized flux but correlated with the radio polarized flux. These authors suggested a fluctuation dynamo-driven B-field amplification scenario associated with the star-forming regions in the disk of M51.

For NGC 1097, the FIR PI is spatially located with the warmest areas of shock-driven galactic bar dynamics in the contact regions between the bar and the starburst ring within the central 1 kpc (Lopez-Rodriguez et al. 2021b). The radio polarization observations show a superposition of ordered spiral B-fields across the starburst ring toward the core (Beck 2007; Lopez-Rodriguez et al. 2021b). Tabatabaei et al. (2018) showed that the B-field strength decreases with the star formation efficiency, which is interpreted as a region dominated by the nonthermal pressure from the B-field, cosmic rays, and turbulence.

For NGC 4736, the radio polarimetric observations showed an ordered spiral B-field across the starburst ring toward the core (Chyży & Buta 2008). This B-field is not related to the star-forming activity but may be related to an evolutionary stage of the galaxy. Our FIR polarimetric observations also seem to show an ordered spiral B-field across the starburst ring (Figure 21).

NGC 7331 suffers from both strong Faraday depolarization due to its high inclination, $78\overset{\circ}{.}1 \pm 2\overset{\circ}{.}7$ (Table 1), and a high

rotation measure, -177 ± 7 rad m^{-2}, arising from the Galactic foreground (Heald et al. 2009). This situation makes the study of this galaxy at radio wavelengths very challenging. NGC 7331 has an axisymmetric gas inflow at the inner boundaries of the starburst ring with its ring rotating clockwise (Battaner et al. 2003). After a comparison of the UV, FIR, C II, and PAH emission, Sutter & Fadda (2022) showed a complex environment due to extinction and directly radiated gas within the central 1 kpc of this galaxy (similar FOV and angular resolution as those from HAWC+ were used). We did not find a detailed analysis of the B-field strength with the star formation rate in this galaxy anywhere in the literature. Further quantitative analysis across the galactic disk of NGC 7331 is required using the information summarized above.

For M51 and NGC 6946, we interpret the steeper α_2 as the result of the fact that the turbulent and/or tangled B-fields increase faster than the ordered B-fields in the star-forming regions and spiral arms. This scenario drives a faster increase in I than in PI. The physical reason is that the B-fields become more isotropic in the star-forming regions at the resolution of our FIR observations. The isotropic B-field is driven by an increase of turbulent and/or tangled B-fields, which increase the unpolarized total intensity associated with the star-forming regions in the galaxy's disk. The relative contribution of the fluctuation dynamo increases toward the regions of star formation in M51 and NGC 6946. Furthermore, group 1 has flatter slopes with higher column densities, dust temperatures, and star formation rates than group 2. These results invite the question of how the stages of star-forming regions as a function of galaxy types affect the fluctuation dynamo in galaxies.

The lack of a relation between the FIR polarized flux and the star-forming regions in NGC 1097, NGC 4736, and NGC 7331 indicates that another physical mechanism from that invoked in M51 and NGC 6946 may be playing a role in the $P - N_{\rm HI+H_2}$ relation. Although we find a median of $\alpha_2 = 0.99 \pm 0.04$ in the $P - N_{\rm HI+H_2}$ relation for all galaxies in group 2, this subset of galaxies (NGC 1097, NGC 4736, and NGC 7331) has a flatter $\alpha_1^{T_{\rm d}} = 4.98 \pm 1.59$ than that measured in M51 and NGC 6946, $\alpha_1^{T_{\rm d}} = 11.69 \pm 0.09$, in the $P - T_{\rm d}$ relation (Figure 5, Table 6). As PI remains constant with $T_{\rm d}$ for all galaxies in group 2, the flatter $\alpha_1^{T_{\rm d}}$ is driven by a flatter I across the full range of $T_{\rm d}$ when compared with M51 and NGC 6946 (Figure 5).

We provide an alternative scenario in terms of the dust grain alignment efficiency. For this subset of galaxies, our results indicate that $T_{\rm d}$ increases faster than $N_{\rm HI+H_2}$, which increases the alignment size, $a_{\rm align}$. The increase in dust grain alignment efficiency produces a flatter $P - T_{\rm d}$ relation for NGC 1097, NGC 4736, and NGC 7331. An enhancement of the dust grain alignment efficiency may be spatially located with the shock-driven regions of NGC 1097 and a large-scale ordered B-field associated with gas dynamics in an evolutionary stage of the galaxy NGC 4736. This interpretation may explain the ordered B-fields found in both objects. In addition, note that NGC 4736 has the flattest power law, $\alpha_1 = -0.06^{+0.04}_{-0.04}$, in the $P - N_{\rm HI+H_2}$ relation of our galaxy sample. This result implies that NGC 4736 has the largest relative contribution of an ordered B-field and/or highest dust grain alignment efficiency for a galactocentric radius of $\geqslant$1 kpc of any of the galaxies observed so far. These results require a detailed study of the B-RAT alignment mechanism (Section 3.1) under shock-driven conditions and galaxy evolution stages.

5.1.3. Group 3: Random B-fields

Group 3 has a single power law in both the $P - N_{\rm HI+H_2}$ and $P - T_{\rm d}$ relations. This is a result of a constant PI with increasing total intensity (Figures 5 and 27). We attribute this result to an increase of isotropic random B-fields with increasing column density and dust temperature. The enhancement of the random B-fields may be produced by star-forming regions in the galaxy's disk. The physical reason is due to the fact that the isotropic B-fields are driven by an increase of unpolarized total intensity associated with denser and hotter regions across the galaxy's disk.

We find several galaxies with a change in PI similar to that in I (Figure 5). These galaxies are Circinus and NGC 1068 at 89 μm, NGC 253 at 89 and 154 μm, and NGC 2146 at 53 and 89 μm. For these galaxies, the PI remains flat up to $\log_{10}(N_{\rm HI+H_2}[{\rm cm}^{-2}]) \sim 21.30$ for all galaxies except NGC 253, where the change in PI occurs at $\log_{10}(N_{\rm HI+H_2}[{\rm cm}^{-2}]) \sim 22.00$. These galaxies also show a broken power law in the $P - T_{\rm d}$ relation with a flatter $\alpha_2^{T_{\rm d}} = -1.49 \pm 0.80$ than those with a single power law, $\alpha_1^{T_{\rm d}} = -7.56 \pm 2.75$ (Figures 5 and 27). The flatter $\alpha_2^{T_{\rm d}}$ is driven by an increase in PI relative to I toward regions of higher dust temperatures. The regions with $\alpha_2^{T_{\rm d}}$ are associated with the starburst ring of Circinus at 89 μm, the central starburst of NGC 253 at 89 μm, and the hot environment affected by the radio jet of NGC 1068 at 89 μm. We speculate that these regions may have an enhancement of dust grain alignment efficiency and/or a relative increase of the ordered B-field driven by the central starburst and the galaxy–jet interaction.

5.2. Polarized Spectra of Starburst Galaxies

We find that the polarized spectra of starburst galaxies vary within the 50–220 μm wavelength range (Figure 4). Figure 9 shows the normalized spectrum, P_λ/P_{λ_0}, to the reference wavelength of $\lambda_0 = 89$ μm for individual starburst galaxies and the median spectrum of all starburst galaxies. The normalized spectrum minimizes depolarization effects (i.e., inclination, grain elongation, turbulence, and tangled B-fields), which work at all wavelengths equally well (Hildebrand et al. 1999). Variations in the polarized spectrum are due to physical variations (i.e., dust temperature, dust grain alignment efficiency, dust grain composition, and random B-fields) that affect each band differently. For individual starburst galaxies, the uncertainties in $\langle P^{\rm hist} \rangle$ are too large to provide any statistical trend, so we study $\langle P^{\rm hist}_{\rm starburst} \rangle$. We measure the median individual, $\langle P^{\rm hist}_{\rm starburst} \rangle$, and integrated, $\langle P^{\rm int}_{\rm starburst} \rangle$, polarization fractions in the range of [1.3, 2.3]% and [0.7, 1.6]%, respectively (Table 4). In both cases, the polarization fraction falls from 53 to a minimum in the 89–154 μm wavelength range and then increases to 214 μm.

There are no polarization spectrum models available that consider the physical conditions of a starburst galaxy. However, several models have been produced for the diffuse ISM and molecular clouds in the Milky Way and nearby galaxies. Draine & Fraisse (2009) generated the 2–3000 μm polarized spectrum using a mixture of spheroidal silicate and graphite grains. These authors produced four models: two of the models assumed that spherical graphite grains are incapable of being magnetically aligned and produce polarized emission. These models also assumed oblate spheroid graphite grains, which are magnetically aligned as a function of their grain size distribution. The other two models (models 2 and 4)

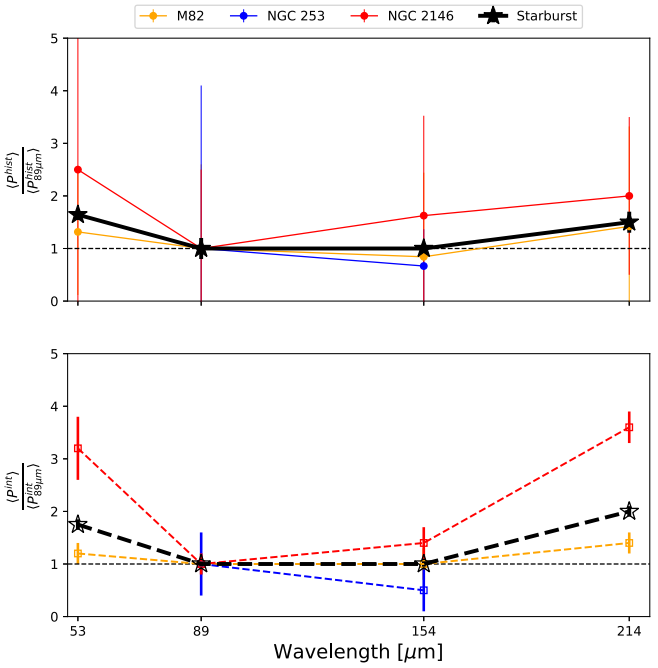

Figure 9. Polarized spectra of starburst galaxies. The normalized spectrum, P_λ/P_{λ_0}, to the reference wavelength of $\lambda_0 = 89$ μm for M82 (orange), NGC 253 (blue), NGC 2146 (red), and the median of the starburst galaxies (black stars) is shown. The individual $\langle P^{\rm hist}\rangle$ (top panel; circles with solid lines) and integrated $\langle P^{\rm int}\rangle$ (bottom panel; open squares with dashed lines) polarization fractions are shown. The horizontal black dashed line shows a flat normalized spectrum for comparison.

assumed both silicate and graphite grains to be oblate. For all models, the 50–220 μm polarized spectrum is flat and then increases with wavelength. For models 1 and 2, the polarized spectrum is ∼0% up to ∼60 μm and then increases to ∼7% at 220 μm. For models 2 and 4, the polarized spectrum is ∼1% at 50 μm and then increases to ∼7%–9% at ∼220 μm. The increase in the polarized spectrum is expected as the optical depth decreases with wavelength, producing an increase in thermal polarized emission. Interestingly, Vandenbroucke et al. (2021) showed a polarized spectrum with a dip in the 60–90 μm wavelength range. They assumed a linear mixture of perfectly aligned silicate dust grains and nonaligned graphite dust grains. Only dust grains with sizes >0.1 μm were assumed to be aligned. However, the authors did not use this mixture for the rest of their simulations, and the 60–90 μm polarization fraction dip is missing in their synthetic 50–220 μm polarimetric observations of a nearby galaxy. The synthetic observations were performed to simulate HAWC+ observations at all bands for a Milky Way–like galaxy at a distance of 10 Mpc.

The FIR polarized spectra of several molecular clouds and star-forming regions in the Milky Way have been measured using FIR polarimetric observations. Hildebrand et al. (1999) measured variations in the 60–350 μm polarized spectra normalized at 100 μm of Galactic clouds. Dense cloud cores (Orion BN/KL) have a rising polarization spectrum, while cloud envelopes (M17) have a falling spectrum. These authors argued that the falling spectra of cloud envelopes may be caused by a mix of dust grain composition, with their efficiencies changing as a function of dust temperature. The regions with warmer temperatures contain the aligned dust grains. For dense clouds, the rising polarized spectrum is in agreement with the expectation of an increasing polarization fraction as the optical depth decreases with increasing wavelength. Michail et al. (2021) measured a falling 50–220 μm polarized spectrum normalized at 214 μm in the OMC-1 (including BN/KL) star-forming region. These authors concluded that the falling polarized spectrum is produced by variations in dust grain alignment efficiency due to a mixture of dust grain populations and variations in dust temperatures along the LOS.

Our FIR polarized spectrum comprises all of the LOS within the central several kiloparsecs of the starburst galaxies. However, the starburst galaxies show several B-field structures: (a) parallel to the galactic outflow, (b) parallel to the galactic plane, and (c) potentially aligned with tidal tails (Figures 14, 16, and 19). These structures have different dust temperature variations as a function of wavelength (Section 5.1). Thus, our polarized spectrum is the result of all of these structures combined. Despite this effect, the polarized emission at 53 μm is dominated by the hot dust in the galactic outflow, at 214 μm it is dominated by the cold dust in the plane of the galaxy, and at 89–154 μm it is the result of a combination of both the galactic outflow and the galactic plane. With these caveats, it is plausible that the falling 53–154 μm polarized spectrum may be due to the hot dust temperature variations along the LOS in the galactic outflow. The rising 154–214 μm polarized spectrum may be due to the expected increase of the polarization fraction from cold dust and low optical depth in the galaxy plane. Any further analysis must be taken with caution, as it is required to physically separate the contributions of the galactic outflow and the galactic disk as a function of wavelength.

5.3. Inclination Effects

We analyze the dependence of the measured polarization fraction with the galaxy inclination, i. Figure 10 shows the median individual, $\langle P^{\rm hist}\rangle$, and integrated, $\langle P^{\rm int}\rangle$, polarization fractions (Table 5) as a function of the galaxy inclination (Table 1). We estimate that the median individual polarization fraction is mostly flat, $\langle P^{\rm hist}_{\rm all}\rangle = 3.1 \pm 0.3\%$, across the 22.°5–83.°0 range of galaxy inclinations. The uncertainties of the median polarization fractions of individual galaxies are too large to measure any potential variation across the galaxy inclination range (Figures 2 and 10; Table 5). The large uncertainties in $\langle P^{\rm hist}\rangle$ are due to the effect of the several physical components (i.e., galactic outflow, spiral arms, interarms, and star-forming regions) on the polarization fraction (Section 5.1). The median integrated polarization fraction is also mostly flat, $\langle P^{\rm int}_{\rm all}\rangle = 1.3 \pm 0.2\%$, across the 22.°5–83.°0 range of galaxy inclinations.

We estimate the expected variation of the polarization fraction as a function of the inclination and the B-field orientation in the POS using two approaches. The first approach uses analytical solutions assuming polarized emission in an optically thin medium, isothermal gas, and equilibrium between gas and dust grains. Under the perfect conditions of no dispersion along the LOS and a constant inclination, the tilt-corrected polarization fraction, $P_{\gamma 1}$, can be estimated as

$$P_{\gamma 1} = \frac{p_0 \cos^2\gamma}{1 - p_0(\frac{\cos^2\gamma}{2} - \frac{1}{3})} \quad (5)$$

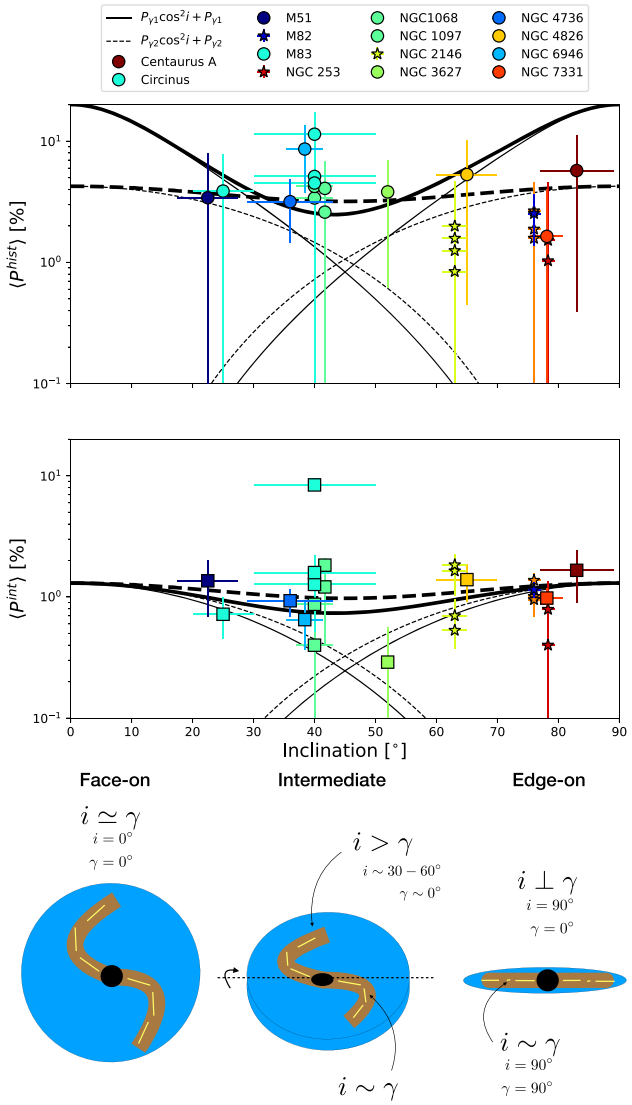

Figure 10. Median and integrated polarization fraction as a function of the galaxy inclination and illustration of results. The median individual, $\langle P^{\rm hist} \rangle$ (top panel), and integrated, $\langle P^{\rm int} \rangle$ (middle panel), polarization fractions for each galaxy are shown. Starburst galaxies are displayed as stars, while the other galaxies are displayed as circles for $\langle P^{\rm hist} \rangle$ and squares for $\langle P^{\rm int} \rangle$. The colors are sorted by the galaxy inclination. The expected polarization using the physical conditions of the environment in which the dust grains are embedded (thick solid line) and a pure geometrical model (thick dashed line) are shown. See Section 5.3 for details about the thin lines of each model. The illustration (bottom panel) shows the change of polarization fraction (yellow lines) as a function of the galaxy's inclination, i, and $B_{\rm POS}$ angle, γ, for face-on (left), intermediate (middle), and edge-on (right) views. For the intermediate view, the axis and direction of rotation in the POS (thin dashed line) are shown. The lower region of the galaxy is the near side of the galaxy, while the upper region is the far side.

(Fiege & Pudritz 2000; Chen et al. 2019; King et al. 2019), where p_0 is the polarization efficiency, which is related to the dust grain properties, and γ is the tilt angle between the ordered B-field and the POS. For a face-on view and assuming that the B-field orientation is in the POS, $\gamma = 0°$, the maximum polarization is then found to be $P_{\gamma 1,\rm max} = p_0/(1 - p_0/6)$ (Fiege & Pudritz 2000). Here p_0 is assumed to be the intrinsic polarization efficiency associated with the entire object with homogeneous alignment.

The second approach parameterizes the observed polarization as

$$P_{\gamma 2} = p_0' \mathcal{R} \mathcal{F} \cos^2 \gamma \quad (6)$$

(Lee & Draine 1985), where p_0' is the intrinsic polarization arising from aligned dust grains given a set of dust grain properties; $\mathcal{R}$ is the Rayleigh reduction factor, which characterizes the efficiency of grain alignment with the local B-field orientation; and $\mathcal{F}$ quantifies the effect of the tangled B-field along the LOS. Assuming no dispersion along the LOS and perfect alignment efficiency, $P_{\gamma 2} = p_0' \cos^2 \gamma$. For a face-on view and assuming that the B-field orientation is in the POS, $\gamma = 0°$, the maximum polarization is then obtained to be $P_{\gamma 2,\rm max} = p_0'$. Here $P_{\gamma 1}$ is a purely geometric definition of the observed polarization fraction, while $P_{\gamma 2}$ takes into account the physical conditions of the environment in which the dust grains are embedded.

Figure 10 shows the expected dependence of the polarization fraction as a function of γ and i using $P_{\gamma 1} \cos^2 i$ and $P_{\gamma 2} \cos^2 i$. For $\langle P^{\rm hist} \rangle$, we scaled $P_{\gamma 1,\rm max}$ to be equal to 20% given by the maximum polarization fraction (Planck Collaboration et al. 2015; our Section 5.4) allowed for an individual polarization measurement across the galaxy disk. We scaled $P_{\gamma 2} \cos^2 i$ to be equal to the measured median polarization fraction $\langle P^{\rm hist}_{\rm all} \rangle = 3.1 \pm 0.3\%$ at the median galaxy inclination of $\langle i \rangle = 46.^\circ 9$ from our sample. For $\langle P^{\rm int} \rangle$, we scale both $P_{\gamma 1,\rm max}$ and $P_{\gamma 2,\rm max}$ to be equal to the median integrated polarization fraction $\langle P^{\rm int}_{\rm all} \rangle = 1.3 \pm 0.2\%$.

Both $P_{\gamma 1} \cos^2 i$ and $P_{\gamma 2} \cos^2 i$ decrease with increasing γ and i; however, the measured polarization fraction remains mostly flat at all inclinations. This implies that, on average, the B-field orientation remains fairly constant with respect to the POS within the galaxies across the inclination range of $i = 22.^\circ 5$–$83.^\circ 0$. This result is due to the fact that the B-field is parallel to the plane of the galaxies at FIR wavelengths. As an example, for highly inclined ($i \sim 90°$) galaxies, the B-fields are expected to be parallel to the POS ($\gamma \sim 0°$), yielding a maximum polarization fraction. To account for this effect, we add the same $P_{\gamma 1}$ and $P_{\gamma 2}$ dependence but with decreasing inclination. We compute the total expected polarization fraction with inclination as the linear combination of $P_\gamma \cos^2 i$ and P_γ across the range of inclinations. We show the total expected polarization as a function of i and γ in Figure 10 (thick black lines). The total expected polarization fraction is the combination of (a) a decrease of the polarization fraction with inclination and tilt from low to intermediate inclinations and (b) an increase of the polarization fraction with tilt from intermediate to high inclinations. This variation may be more or less severe depending on the B-field morphology and galaxy type. We estimate the expected polarization fraction as a function of i and γ below.

For face-on views ($i = 0°$), taking into account that (a) the disk of the galaxy is at a constant inclination in our LOS and parallel to the POS and (b) the measured weighted-average column density B-field is parallel to the plane of the galaxy ($\gamma = 0°$), we find that $\gamma \simeq i$ (Figure 10). The effect caused by the tilt and inclination is the same across the galaxy disk. The expected polarization is close to its maximum given by $P_{\gamma 1,\rm max}$ and $P_{\gamma 2,\rm max}$. For low galaxy inclinations, tilt and inclination effects only displace the entire trend up or down in P without affecting the slope of the $P - N_{\rm H I+H_2}$ and $P - T_{\rm d}$ relations.

For edge-on views ($i = 90°$), taking that the B-field is parallel to the disks of spiral galaxies, $i \perp \gamma$, where $\gamma = 0°$ (Figure 10). The expected polarization fraction is close to its maximum at both face-on and edge-on views. Indeed, we measure this effect at the two edges of our inclination ranges: M51 ($i = 22.^{\circ}5 \pm 5°$) and Centaurus A ($i = 83° \pm 6°$). The measured polarization fractions along the several LOSs of the resolved disks may vary due to the dependence with $P - N_{\rm HI+H_2}$ and $P - T_{\rm d}$ driven by turbulence and/or tangled B-fields along the LOS. An exception may be when the spiral arms are along our LOS, yielding a B-field orientation perpendicular to the POS, $\gamma = 90°$. In this case, the polarization fraction may tend to zero. This example is displayed in Figure 10 (bottom right). Jones et al. (2020) observed tentative evidence of this behavior in NGC 891 using 154 μm polarimetric observations with HAWC+.

For intermediate inclinations ($i \sim 30°$–$60°$), the measured polarization is affected by both γ and i (Figure 10). This case creates a depolarization effect within the same galactocentric distance across the galaxy disk. Along the axis of rotation in the POS, the ordered B-field orientation and the inclination can be up to $\gamma \leqslant i$, yielding a decrease in the polarization fraction driven by both i and γ. Perpendicular to this axis, the ordered B-field is parallel to the POS but different from the inclination of the galaxy disk, i.e., $i > \gamma$, yielding the maximum polarization fraction in the galaxy disk. As the inclination is the same across the galaxy disk, the depolarization is driven by the change of γ (Appendix D). This effect causes the dip in polarization at intermediate inclinations $i \sim 30°$–$60°$ shown in Figure 10.

We provide an estimation of the depolarization effect due to the change of γ across the disk for a constant inclination in Appendix D and Figure 28. As an example, we use the galaxies in our sample within an inclination of 30°–60°. These galaxies have a median $i_{30°–60°} = 40.^{\circ}0 \pm 2.^{\circ}8$ and $\langle P^{\rm hist}_{30°–60°} \rangle = 4.3 \pm 2.8\%$. We assume that the angular difference between the B-field orientation and the POS can be as large as the galaxy inclination, i.e., $\Delta\gamma \leqslant i$. Finally, we estimate that the regions of the galaxy along the axis of rotation in the POS with $\Delta\gamma \sim i$ can suffer a depolarization of up to a factor of 2.5 assuming a maximum polarization fraction of $p_{\gamma 1,\rm max} = \langle P^{\rm hist}_{30°–60°} \rangle = 4.3 \pm 2.8\%$ for our first approach ($P_{\gamma 1}$) and up to a factor of 1.7 for the pure geometrical approach ($P_{\gamma 2}$). Under these conditions, the depolarized regions in the galaxy disk would have an expected polarization of $\langle P^{\rm hist}_{30°–60°} \rangle / 2.5 \geqslant 1.7\%$ produced by γ and i, which can still be measured using our observations. Note that this depolarization effect is different from the trends shown in $P - N_{\rm HI+H_2}$ and $P - T_{\rm d}$. These relations are driven by turbulence and/or tangled B-fields along the LOS and dust grain alignment efficiency.

5.4. Comparison with Planck Observations of the Milky Way

We compare our results in spiral galaxies with those from Planck in the Milky Way. The $P - N_{\rm H\,I}$ relation in the Milky Way shows a maximum polarization fraction of $P \sim 20\%$ at 353 GHz within the column density range of $\log_{10}(N_{\rm HI}[{\rm cm}^{-2}]) = [20.30, 21.30]$ and a sharp drop of polarization at $\log_{10}(N_{\rm HI}[{\rm cm}^{-2}]) = 22.18$ (Planck Collaboration et al. 2015, see Figure 19). Note that the maximum polarization by Planck is measured for diffuse sight lines with very ordered B-fields (e.g., Panopoulou et al. 2019). When polarization measurements within the Galactic plane are included, a flatter $P - N_{\rm H\,I}$ relation is found at $\log_{10}(N_{\rm HI}[{\rm cm}^{-2}]) \geqslant 22.47$. Thus, an increase of $\sim$0.3 dex in $\log_{10}(N_{\rm HI}[{\rm cm}^{-2}])$ and a flatter slope in the $P - N_{\rm H\,I}$ relation are found when a high column density, dust temperature, and star formation rate are included. These values are shown in Figure 7.

Using our observations, we measure a maximum polarization fraction of 15% (Figure 2) within the range of column densities of $\log_{10}(N_{\rm HI}[{\rm cm}^{-2}]) = [20.00, 21.83]$. After correcting by inclination, the maximum polarization fraction reached $\sim$18% for column densities $\log_{10}(N_{\rm HI+H_2}[{\rm cm}^{-2}]) \leqslant 21.19$ in the interarms of the outskirts of NGC 6946. We estimate a difference of 0.73 dex between the measured cutoff column densities of $\log_{10}(N^{\rm c}_{\rm HI+H_2}[{\rm cm}^{-2}]) = 21.59 \pm 0.31$, which includes starburst galaxies, and $\log_{10}(N^{\rm c}_{\rm HI+H_2}[{\rm cm}^{-2}]) = 20.86 \pm 0.26$, which includes spiral galaxies. These cutoff densities are associated with flatter and steeper slopes, respectively (Figure 5). These results show that an increase in the cutoff column density and star formation activity flattens the $P - N_{\rm H\,I}$ relation. This result is similar to that found in the Milky Way by Planck, considering the large uncertainties in the Planck measurements (which are dominated by zero-point uncertainty in Stokes I).

Using Planck data (Planck Collaboration et al. 2015, see Figure 19), we estimate an average polarization fraction of $\sim$4% with a range of [0, 20]% for our estimated median cutoff column density of $\log_{10}(N^{\rm c}_{\rm HI+H_2}[{\rm cm}^{-2}]) = 20.86 \pm 0.29$ in spiral galaxies (i.e., M51, M83, NGC 4736, NGC 6946, and NGC 7331). Using HAWC+ data, the median polarization fraction is estimated to be $\langle P^{\rm hist}_{\rm spirals,154\mu m} \rangle = 3.3 \pm 0.9\%$ (Section 4.1) with individual polarization fractions in the range of [0, 15]% across the disks of these spiral galaxies. Figure 7 shows that the FIR polarization measurements within the disks of spiral galaxies fall within the range of column densities associated with the maximum polarization fraction by means of magnetically aligned dust grains in the Milky Way. Our measured maximum polarization fraction and the trends in $P - N_{\rm HI+H_2}$ are similar to those found in the Milky Way by Planck. These results also show that the emissive polarization from these spiral galaxies may arise from a similar ISM composition to those in the Milky Way.

6. Conclusions

We have presented SALSA, the first FIR polarimetric survey of nearby galaxies using HAWC+/SOFIA. We have provided a brief background on extragalactic magnetism (Section 2) with the goal of introducing to the reader the definitions (Sections 2.3 and 3.1) and the most current results. The main scientific goals of this program are to (Section 3.2)

1. characterize the dependence of the large-scale ordered B-fields on the probed ISM phase and provide measurements for galactic dynamo theories,
2. quantify the relative contributions of the mean-field and fluctuation dynamos across a range of galaxy types and dynamical states,
3. measure the effect of galactic outflows on the galactic B-field in starburst galaxies and quantify how the B-field is transported to the CGM, and
4. measure the B-field structures of interacting galaxies.

We summarize the first data release of the program (Sections 3.3 and 3.4) as follows.

1. The first data release comprises 33% (51.34 out of 155.70 hr) of the awarded total exposure time of the SOFIA Legacy Program taken from 2020 January to 2021 November.
2. All observations in this program were and will be performed using the newly implemented OTFMAP polarization mode with HAWC+ (Section 3.4). A full characterization of the OTFMAP polarimetric mode is described in Paper III (Lopez-Rodriguez et al. 2022).
3. The final data products of 14 galaxies (Table 3) in the wavelength range of 53–214 μm ready for scientific analysis, as well as tabulated figures and codes, are available on the Legacy Program website (http://galmagfields.com/).

The main results of this data release focused on the polarization fraction of galaxies (Section 4.1) are as follows.

1. Polarization fractions across the galaxy disks range from 0% to 15% (Figure 2).
2. The lowest median polarization fraction measurements are found in the starburst galaxies M82, NGC 253, and NGC 2146 (Figure 2 and Table 5). The lowest polarization fractions are colocated with star-forming regions across the disk of spiral galaxies. The highest polarization fraction measurements are found in the interarms and outskirts of spiral galaxies.
3. We report the first polarized spectrum of starburst galaxies (Figure 4). The polarized spectrum varies as a function of wavelength with a minimum located in the range of 89–154 μm. The polarized emission at 53 μm is dominated by the hot dust in the galactic outflow; at 214 μm, it is dominated by the cold dust in the plane of the galaxy; and at 89–154 μm, it is the result of a combination of both the galactic outflow and the galactic plane (Figure 14). It is plausible that the falling 53–154 μm polarized spectrum may be due to the hot dust temperature variations along the LOS in the galactic outflow. The rising 154–214 μm polarized spectrum may be due to the expected increase of the polarization fraction from cold dust and low optical depth in the galaxy plane (Section 5.2).

The main results focused on the polarization fraction of galaxies with the column density and dust temperature are (Sections 4.2 and 4.3) as follows.

1. For all galaxies, the polarization fraction decreases across the column density range of $\log_{10}(N_{\rm HI+H_2}[{\rm cm}^{-2}])=[19.96, 22.91]$ and dust temperatures of $T_{\rm d}=[19, 48]$ K.
2. The highest polarization fractions, $\geqslant$10%, are found at the lowest column density ranges, $\log_{10}(N_{\rm HI+H_2}[{\rm cm}^{-2}])\leqslant 21$, and dust temperature ranges, $T_{\rm d}\leqslant 30$ K, typically located in the outskirts of galaxies.
3. The spiral galaxies show a median polarization fraction of $3.3\%\pm0.9\%$ at 154 μm using the individual measurements across the galaxy disk (Figure 4 and Table 4) and an integrated polarization fraction of $\langle P^{\rm int}_{\rm spiral,154\mu m}\rangle=0.8\%\pm0.1\%$.

Based on the trends of the $P-N_{\rm HI+H_2}$ and $P-T_{\rm d}$ relations, we found that 50% (seven out of 14) of the galaxies require a broken power law in the $P-N_{\rm HI+H2}$ relation. As described in Section 3.1, a maximum polarization is measured in the absence of tangled B-fields along the LOS, turbulence, and/or inclination effects. Under these "perfect" conditions, the polarization fraction should be expected to be constant with column density due to a dominant ordered B-field within the beam of the observations. Assuming that the galaxy disk is at a constant inclination, a decrease in polarization fraction with increasing column density is attributed to an increase in turbulent and/or tangled B-fields along the LOS (i.e., random B-fields) within the beam of the observations. The inclination effects on the polarization fraction are discussed in Section 5.3. We use the $P-N_{\rm HI+H_2}$ plots as a proxy for the relative contribution of the random-to-ordered B-fields within the beam of the observations. The $P-T_{\rm d}$ relation is not sensitive to the physical conditions of the B-fields in the galaxy's disk but rather to the ISM conditions (i.e., radiation field). The $P-T_{\rm d}$ relation provides information about the polarization efficiency toward star-forming regions.

We identified three main groups (Figure 5 and Section 5.1) and interpret them in terms of the B-field structure.

Group 1.
The $P-N_{\rm HI+H_2}$ and $P-T_{\rm d}$ relations have a flatter power law, $\alpha_2>\alpha_1$, after the cutoff column density and dust temperature, respectively. The galaxies in this group are Circinus at 214 μm, M83 at 154 μm, and M82 at all bands (Figure 25). We found that the second power law is associated with the central starburst of M82, the inner bar and the inflection regions between the inner bar and the spiral arms of M83, and the starburst ring of Circinus. After the cutoff column density, $\log_{10}(N^{\rm c}_{\rm HI+H_2}[{\rm cm}^{-2}])\geqslant 21.59\pm0.31$, and dust temperature, $T^{\rm c}_{\rm d}\geqslant 35.8\pm3.8$ K, the ordered B-fields in these galaxies increase at a higher rate than the random B-fields. The physical reason is that compressed B-fields produce a relative decrease of the isotropic B-fields (i.e., an increase in anisotropic B-fields), yielding flatter slopes.

Group 2.
The $P-N_{\rm HI+H_2}$ relation has a steeper power law, $\alpha_2<\alpha_1$, after the cutoff column density, while a single power law is found in the $P-N_{\rm HI+H_2}$ relation. The galaxies in this group are M51, NGC 4736, NGC 6946, and NGC 7331 at 154 μm and NGC 1097 at 89 and 154 μm (Figure 26). We found that a second power law is required for the central regions of galaxies associated with the galaxy's core and star-forming regions across the galaxy's disk. We interpret the steeper α_2 as being due to a relatively faster increase of the turbulent and/or tangled B-fields than the ordered B-fields in the star-forming regions and spiral arms. The physical reason is that the B-fields become more isotropic in the star-forming regions at the resolution of our FIR observations. The isotropic B-field is driven by an increase of turbulent and/or tangled B-fields, which increases the unpolarized total intensity associated with the star-forming regions in the galaxy's disk.

Group 3.
The $P-N_{\rm HI+H_2}$ and $P-T_{\rm d}$ relations have a single power law. The galaxies associated with this group are shown in Figure 27. This result is due to an increase of isotropic random B-fields with increasing column density and dust

temperature. The enhancement of the random B-fields may be produced by star-forming regions in the galaxy's disk. The physical reason is that the isotropic B-fields are driven by an increase of unpolarized total intensity associated with denser and hotter regions across the galaxy's disk.

We have also compared our FIR polarimetric observations of spiral galaxies to those in the Milky Way by Planck (Planck Collaboration et al. 2015). The main results are (Figure 7 and Section 5.4) as follows.

1. Using our observations, we found that an increase in the cutoff column density and star formation activity flattens the $P - N_{\rm H\ I}$ relation. This result is similar to the trends found in the $P - N_{\rm H\ I}$ relation with and without the Galactic center by Planck.
2. The FIR polarization measurements within the disk of spiral galaxies fall within the range of column densities associated with the maximum polarization fraction by means of magnetically aligned dust grains in the Milky Way by Planck.

From 2021 November to 2022 September (the end of SOFIA operations), SOFIA was prioritizing the observations associated with SALSA while maximizing the scientific output from multiple Legacy and high-priority programs. Regardless of the SOFIA output, this data release already conveys the power and potential of FIR polarimetric observations on extragalactic magnetism. Without SOFIA, the next opportunity for FIR polarimetry will arise somewhere between decades from now and infinity; no such capability is even being contemplated, as far as we know. To continue to push the boundaries of our understanding of extragalactic magnetism, FIR polarimetric observations must be included in the next NASA FIR probe mission class.

We are grateful to the anonymous referee, whose comments greatly helped to clarify and improve the manuscript. Based on observations made with the NASA/DLR Stratospheric Observatory for Infrared Astronomy (SOFIA) under the 07_0034, 08_0012 Program. SOFIA is jointly operated by the Universities Space Research Association (USRA), Inc., under NASA contract NNA17BF53C and the Deutsches SOFIA Institut (DSI) under DLR contract 50 OK 0901 to the University of Stuttgart. K.T. has received funding from the European Research Council (ERC) under the European Union's Horizon 2020 research and innovation program under grant agreement No. 771282. E.N. acknowledges funding from the Hellenic Foundation for Research and Innovation (project No. 224) and the ERC grant "Interstellar" (grant agreement 740120).

Facilities: SOFIA (HAWC+), Herschel (PACS, SPIRE).

Software: ASTROPY (Astropy Collaboration et al. 2013), APLPY (Robitaille & Bressert 2012), MATPLOTLIB (Hunter 2007), PYMC3 (Salvatier et al. 2016).

Appendix A
Polarization, Column Density, and Dust Temperature Maps

This appendix shows the individual polarization maps of the HAWC+ observations for each galaxy and wavelength. In Figures 11–24, the first and second columns show the total and polarized surface brightness with overlaid polarization

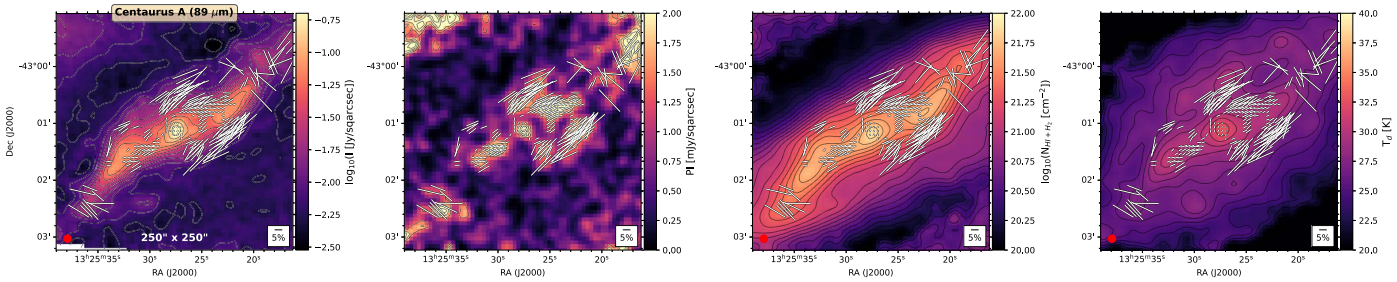

Figure 11. Centaurus A at 89 μm (group 3). First column: total intensity (color scale) in logarithmic scale with contours starting at 8σ increasing in steps of $2^n\sigma$, with $n = 3, 3.5, 4, ...$ The polarization fraction measurements (white lines) with a legend of 5% (bottom right) are shown. The polarization fraction measurements with PI/$\sigma_{\rm PI} \geqslant 3$, $P \leqslant 20\%$, and $I/\sigma_I \geqslant 10$ were selected. The beam size (red circle) is shown. Second column: polarization map over the PI (color scale) in linear scale with contours starting at 3σ increasing in steps of 1σ. Third column: polarization map over the column density (color scale) in logarithmic scale with contours starting at $\log_{10}(N_{\rm HI+H_2}[{\rm cm}^{-2}]) = 20$ increasing in steps of $\log_{10} N_{\rm HI+H_2}[{\rm cm}^{-2}] = 0.1$. Fourth column: polarization map over the dust temperature (color scale) in linear scale with contours starting at 20 K increasing in steps of 1 K.

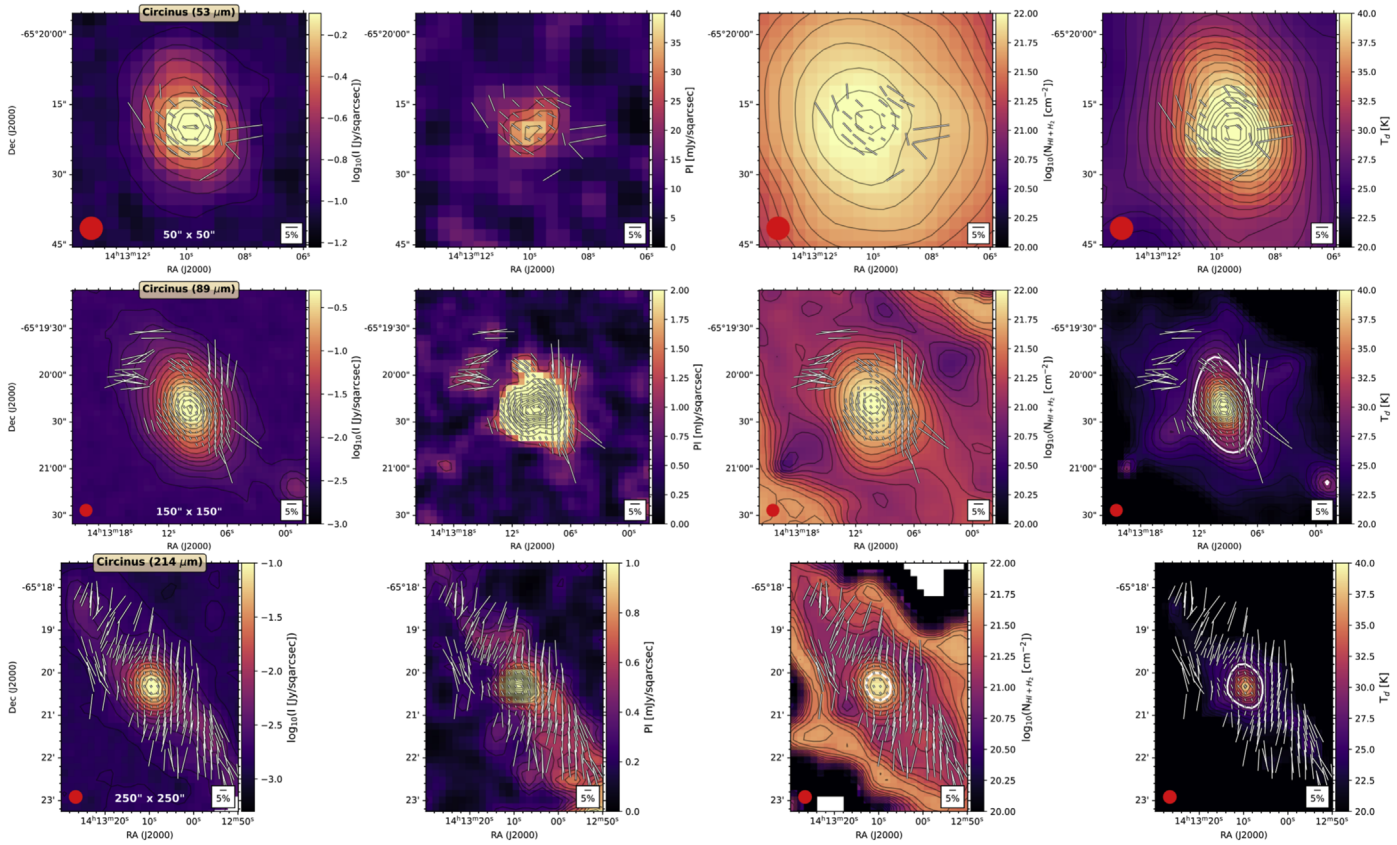

Figure 12. Circinus at 53 (top) and 89 μm (middle) in group 3 and 214 μm (bottom) in group 1. First column: total intensity (color scale) in logarithmic scale with contours starting at 8σ increasing in steps of $2^n\sigma$, with $n = 3, 3.5, 4, ...$ The polarization fraction measurements (white lines) with a legend of 5% (bottom right) are shown. The polarization fraction measurements with $\mathrm{PI}/\sigma_{\mathrm{PI}} \geqslant 3$, $P \leqslant 20\%$, and $I/\sigma_I \geqslant 10$ were selected. The beam size (red circle) is shown. Second column: polarization map over the PI (color scale) in linear scale with contours starting at 3σ increasing in steps of 1σ at 53 and 214 μm and 5σ at 89 μm. Third column: polarization map over the column density (color scale) in logarithmic scale with contours starting at $\log_{10}(N_{\mathrm{HI+H_2}}[\mathrm{cm}^{-2}]) = 20$ increasing in steps of $\log_{10} N_{\mathrm{HI+H_2}}[\mathrm{cm}^{-2}] = 0.1$. Fourth column: polarization map over the dust temperature (color scale) in linear scale with contours starting at 20 K increasing in steps of 1 K. The white contours in the $N_{\mathrm{HI+H_2}}$ (at 214 μm) and T_{d} (at 89 and 214 μm) maps show the cutoff column density and dust temperature values shown in Table 6 and described in Sections 4.2 and 4.3, respectively.

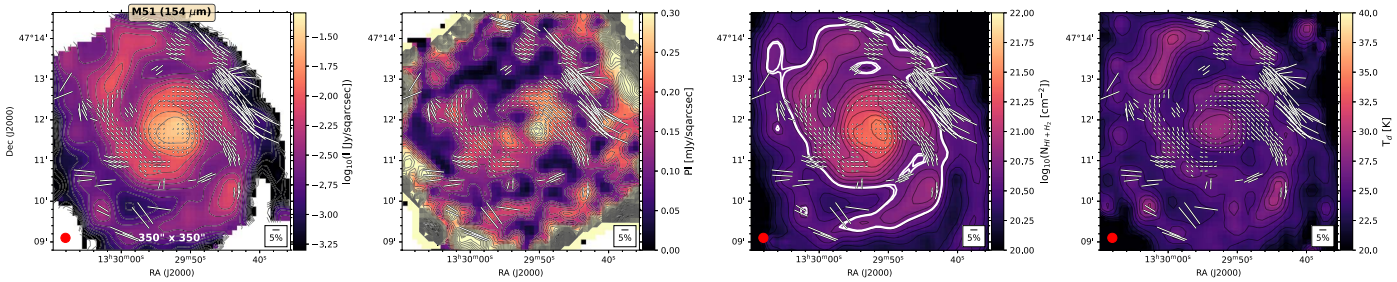

Figure 13. Object M51 at 154 μm (group 2). First column: total intensity (color scale) in logarithmic scale with contours starting at 8σ increasing in steps of $2^n\sigma$, with $n = 3, 3.5, 4, ...$ The polarization fraction measurements (white lines) with a legend of 5% (bottom right) are shown. The polarization fraction measurements with $\mathrm{PI}/\sigma_{\mathrm{PI}} \geqslant 3$, $P \leqslant 20\%$, and $I/\sigma_I \geqslant 10$ were selected. The beam size (red circle) is shown. Second column: polarization map over the PI (color scale) in linear scale with contours starting at 3σ increasing in steps of 1σ. Third column: polarization map over the column density (color scale) in logarithmic scale with contours starting at $\log_{10}(N_{\mathrm{HI+H_2}}[\mathrm{cm}^{-2}]) = 20$ increasing in steps of $\log_{10} N_{\mathrm{HI+H_2}}[\mathrm{cm}^{-2}] = 0.1$. Fourth column: polarization map over the dust temperature (color scale) in linear scale with contours starting at 20 K increasing in steps of 1 K. The white contours in the $N_{\mathrm{HI+H_2}}$ maps show the cutoff column density and dust temperature values shown in Table 6 and described in Sections 4.2 and 4.3, respectively.

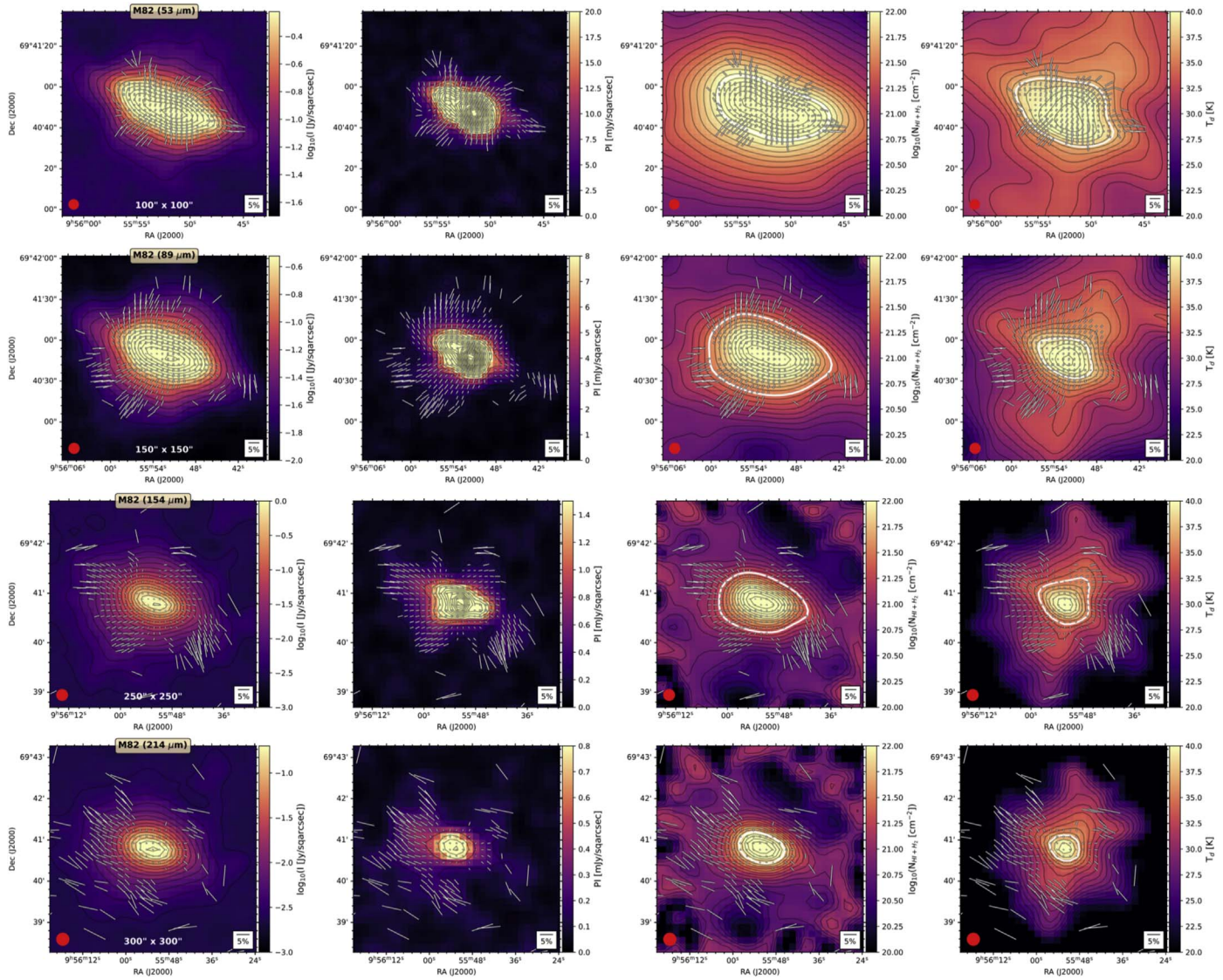

Figure 14. Object M82 at 53 (first row), 89 (second row), 154 (third row), and 214 (fourth row) μm (group 1). First column: total intensity (color scale) in logarithmic scale with contours starting at 8σ increasing in steps of $2^n\sigma$, with $n = 3, 3.5, 4, ...$ The polarization fraction measurements (white lines) with a legend of 5% (bottom right) are shown. The polarization fraction measurements with $\mathrm{PI}/\sigma_{\mathrm{PI}} \geqslant 3$, $P \leqslant 20\%$, and $I/\sigma_I \geqslant 80$ were selected. The beam size (red circle) is shown. Second column: polarization map over the PI (color scale) in linear scale with contours starting at 3σ increasing in steps of 5σ. Third column: polarization map over the column density (color scale) in logarithmic scale with contours starting at $\log_{10}(N_{\mathrm{HI+H_2}}[\mathrm{cm}^{-2}]) = 20$ increasing in steps of $\log_{10} N_{\mathrm{HI+H_2}}[\mathrm{cm}^{-2}] = 0.1$. Fourth column: polarization map over the dust temperature (color scale) in linear scale with contours starting at 20 K increasing in steps of 1 K. The white contours in the $N_{\mathrm{HI+H_2}}$ (at all wavelengths) and T_{d} (at all wavelengths) maps show the cutoff column density and dust temperature values shown in Table 6 and described in Sections 4.2 and 4.3, respectively.

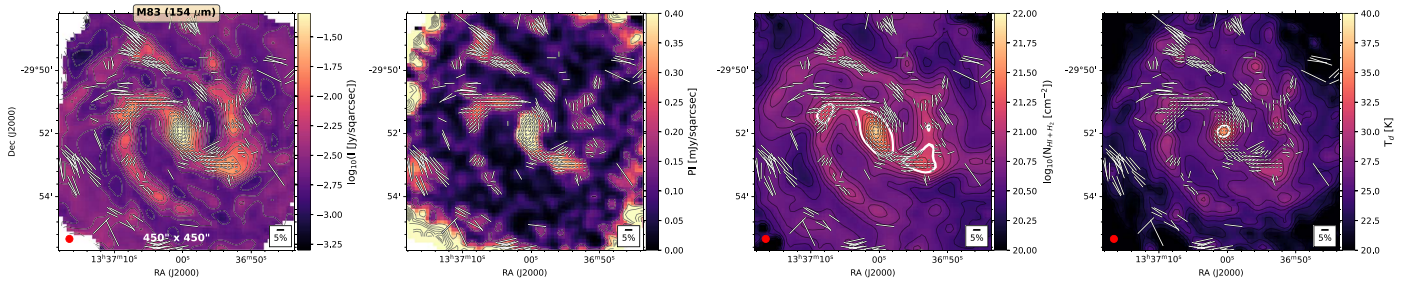

Figure 15. Object M83 at 154 μm (group 1). First column: total intensity (color scale) in logarithmic scale with contours starting at 8σ increasing in steps of $2^n\sigma$, with $n = 3, 3.5, 4, ...$ The polarization fraction measurements (white lines) with a legend of 5% (bottom right) are shown. The polarization fraction measurements with $\mathrm{PI}/\sigma_{\mathrm{PI}} \geqslant 3$, $P \leqslant 20\%$, and $I/\sigma_I \geqslant 10$ were selected. The beam size (red circle) is shown. Second column: polarization map over the PI (color scale) in linear scale with contours starting at 3σ increasing in steps of 5σ. Third column: polarization map over the column density (color scale) in logarithmic scale with contours starting at $\log_{10}(N_{\mathrm{HI+H_2}}[\mathrm{cm}^{-2}]) = 20$ increasing in steps of $\log_{10} N_{\mathrm{HI+H_2}}[\mathrm{cm}^{-2}] = 0.1$. Fourth column: polarization map over the dust temperature (color scale) in linear scale with contours starting at 20 K increasing in steps of 1 K. The white contours in the $N_{\mathrm{HI+H_2}}$ and T_{d} maps show the cutoff column density and dust temperature values shown in Table 6 and described in Sections 4.2 and 4.3, respectively.

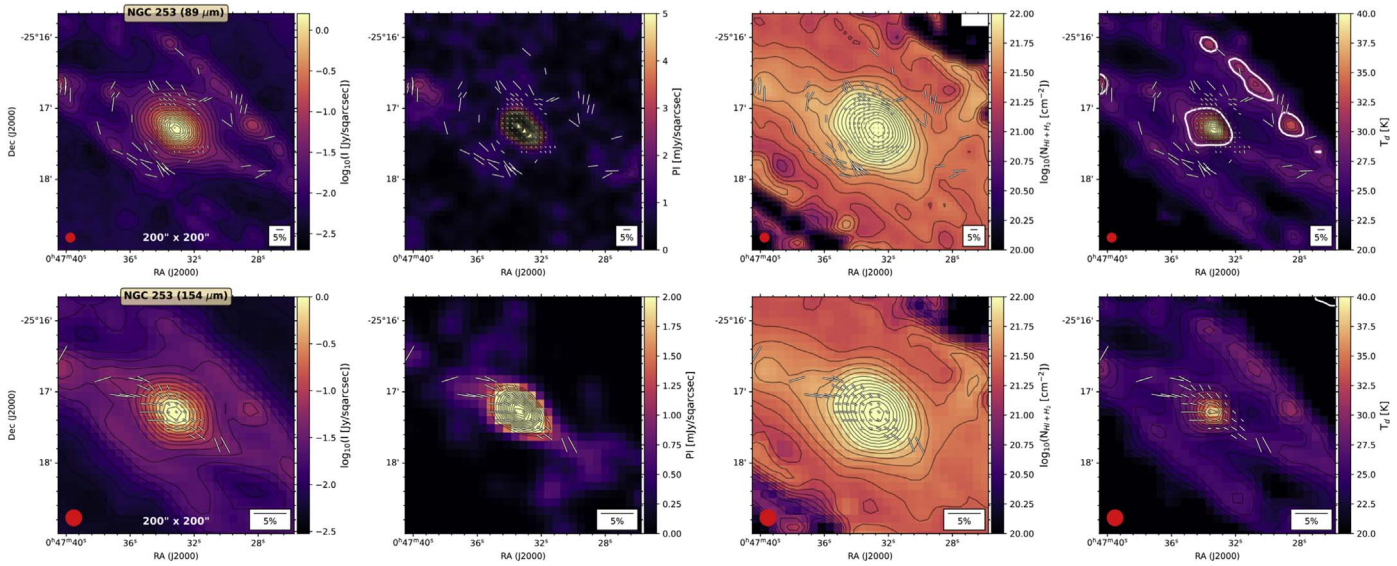

Figure 16. Object NGC 253 at 89 (top) and 154 (bottom) μm (group 3). First column: total intensity (color scale) in logarithmic scale with contours starting at 8σ increasing in steps of $2^n\sigma$, with $n = 3, 3.5, 4, ...$ The polarization fraction measurements (white lines) with a legend of 5% (bottom right) are shown. The polarization fraction measurements with $\mathrm{PI}/\sigma_{\mathrm{PI}} \geqslant 3$, $P \leqslant 20\%$, and $I/\sigma_I \geqslant 10$ were selected. The beam size (red circle) is shown. Second column: polarization map over the PI (color scale) in linear scale with contours starting at 3σ increasing in steps of 5σ at 89 μm and 2σ at 154 μm. Third column: polarization map over the column density (color scale) in logarithmic scale with contours starting at $\log_{10}(N_{\mathrm{HI+H_2}}[\mathrm{cm}^{-2}]) = 20$ increasing in steps of $\log_{10} N_{\mathrm{HI+H_2}}[\mathrm{cm}^{-2}] = 0.1$. Fourth column: polarization map over the dust temperature (color scale) in linear scale with contours starting at 20 K increasing in steps of 1 K. The white contours in the T_{d} (at 89 μm) maps show the cutoff column density and dust temperature values shown in Table 6 and described in Sections 4.2 and 4.3, respectively.

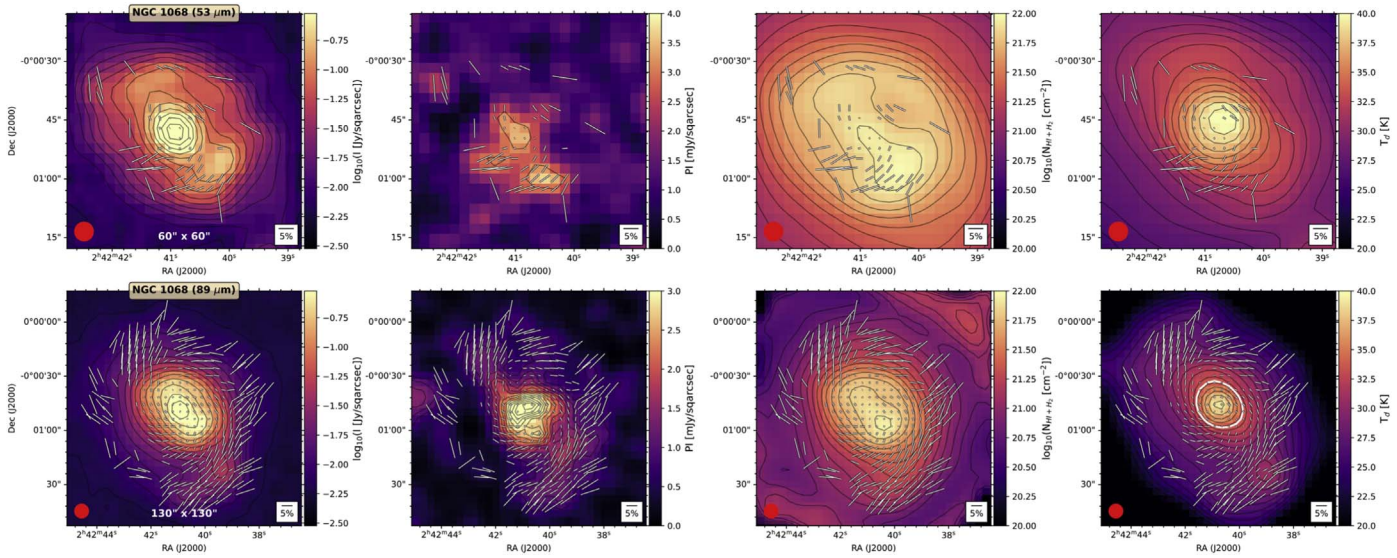

Figure 17. Object NGC 1068 at 53 (top) and 89 (bottom) μm (group 3). First column: total intensity (color scale) in logarithmic scale with contours starting at 8σ increasing in steps of $2^n\sigma$, with $n = 3, 3.5, 4, ...$ The polarization fraction measurements (white lines) with a legend of 5% (bottom right) are shown. The polarization fraction measurements with $\mathrm{PI}/\sigma_{\mathrm{PI}} \geqslant 3$, $P \leqslant 20\%$, and $I/\sigma_I \geqslant 10$ were selected. The beam size (red circle) is shown. Second column: polarization map over the PI (color scale) in linear scale with contours starting at 3σ increasing in steps of 1σ. Third column: polarization map over the column density (color scale) in logarithmic scale with contours starting at $\log_{10}(N_{\mathrm{HI+H_2}}[\mathrm{cm}^{-2}]) = 20$ increasing in steps of $\log_{10} N_{\mathrm{HI+H_2}}[\mathrm{cm}^{-2}] = 0.1$. Fourth column: polarization map over the dust temperature (color scale) in linear scale with contours starting at 20 K increasing in steps of 1 K. The white contours in the T_{d} (at 89 μm) maps show the cutoff column density and dust temperature values shown in Table 6 and described in Sections 4.2 and 4.3, respectively.

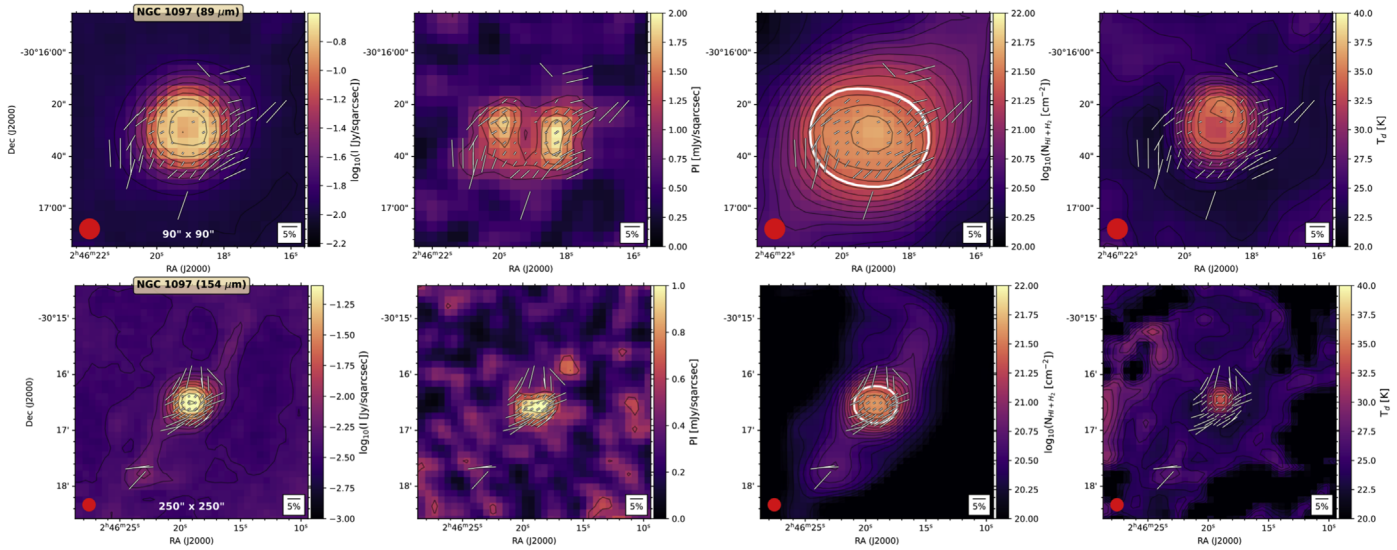

Figure 18. Objects NGC 1097 at 89 (top) and 154 (bottom) μm (group 2). First column: total intensity (color scale) in logarithmic scale with contours starting at 8σ increasing in steps of $2^n\sigma$, with $n = 3, 3.5, 4, ...$ The polarization fraction measurements (white lines) with a legend of 5% (bottom right) are shown. The polarization fraction measurements with $\mathrm{PI}/\sigma_{\mathrm{PI}} \geqslant 3$, $P \leqslant 20\%$, and $I/\sigma_I \geqslant 10$ were selected. The beam size (red circle) is shown. Second column: polarization map over the PI (color scale) in linear scale with contours starting at 3σ increasing in steps of 1σ. Third column: polarization map over the column density (color scale) in logarithmic scale with contours starting at $\log_{10}(N_{\mathrm{HI+H_2}}[\mathrm{cm}^{-2}]) = 20$ increasing in steps of $\log_{10} N_{\mathrm{HI+H_2}}[\mathrm{cm}^{-2}] = 0.1$. Fourth column: polarization map over the dust temperature (color scale) in linear scale with contours starting at 20 K increasing in steps of 1 K. The white contours in the $N_{\mathrm{HI+H_2}}$ (at 89 and 154 μm) maps show the cutoff column density and dust temperature values shown in Table 6 and described in Sections 4.2 and 4.3, respectively.

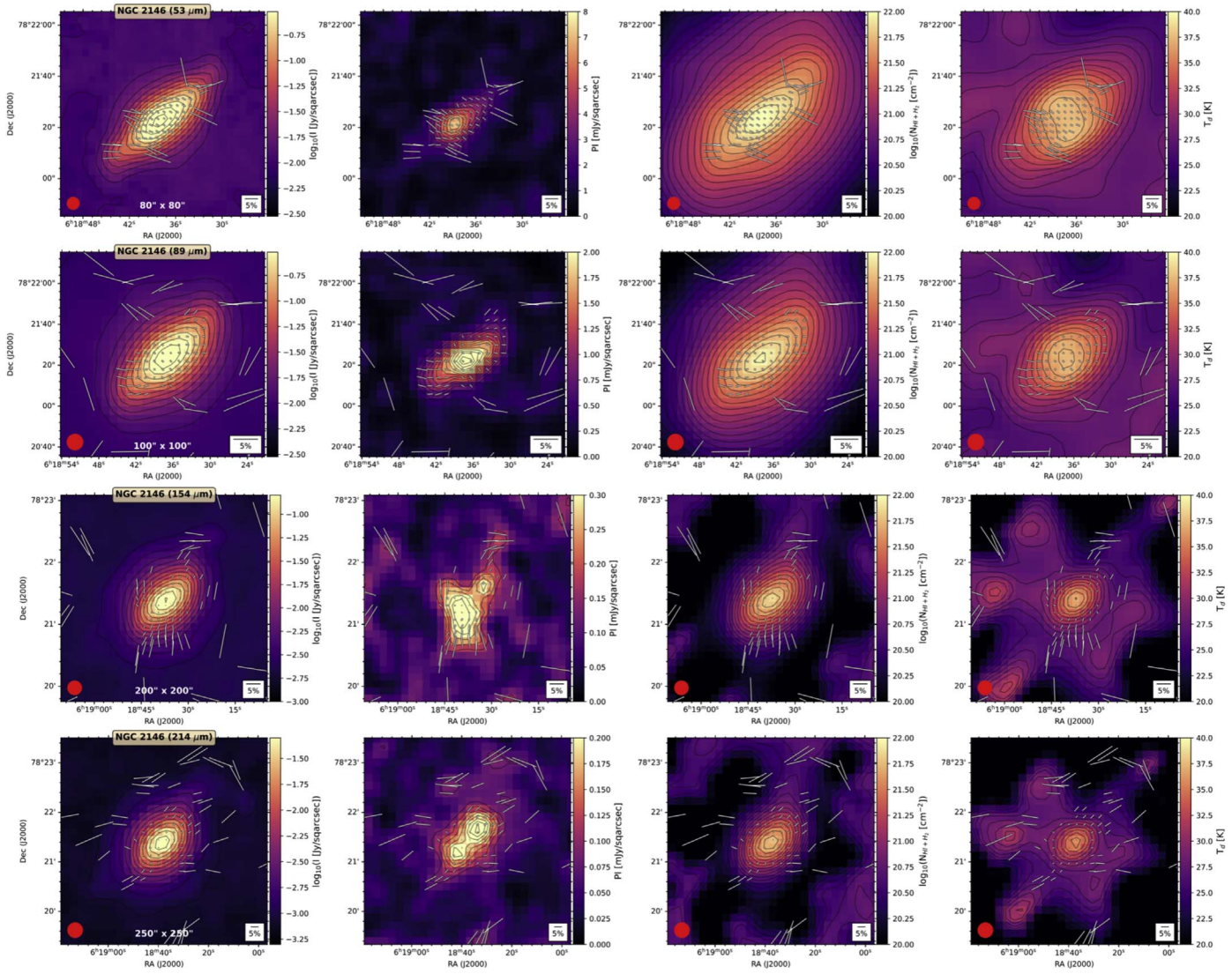

Figure 19. Object NGC 2146 at 53 (first row), 89 (second row), 154 (third row), and 214 (fourth row) μm (group 3). First column: total intensity (color scale) in logarithmic scale with contours starting at 8σ increasing in steps of $2^n\sigma$, with $n = 3, 3.5, 4, ...$ The polarization fraction measurements (white lines) with a legend of 5% (bottom right) are shown. The polarization fraction measurements with $\mathrm{PI}/\sigma_{\mathrm{PI}} \geqslant 3$, $P \leqslant 20\%$, and $I/\sigma_I \geqslant 20$ were selected. The beam size (red circle) is shown. Second column: polarization map over the PI (color scale) in linear scale with contours starting at 3σ increasing in steps of 1σ. Third column: polarization map over the column density (color scale) in logarithmic scale with contours starting at $\log_{10}(N_{\mathrm{HI+H_2}}[\mathrm{cm}^{-2}]) = 20$ increasing in steps of $\log_{10} N_{\mathrm{HI+H_2}}[\mathrm{cm}^{-2}] = 0.1$. Fourth column: polarization map over the dust temperature (color scale) in linear scale with contours starting at 20 K increasing in steps of 1 K.

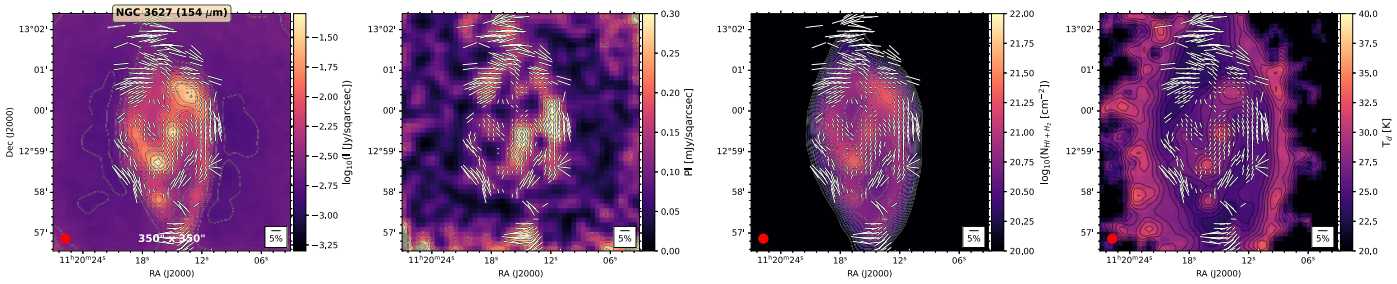

Figure 20. Object NGC 3627 at 154 μm (group 3). First column: total intensity (color scale) in logarithmic scale with contours starting at 8σ increasing in steps of $2^n\sigma$, with $n = 3, 3.5, 4, ...$ The polarization fraction measurements (white lines) with a legend of 5% (bottom right) are shown. The polarization fraction measurements with $\mathrm{PI}/\sigma_{\mathrm{PI}} \geqslant 3$, $P \leqslant 20\%$, and $I/\sigma_I \geqslant 40$ were selected. The beam size (red circle) is shown. Second column: polarization map over the PI (color scale) in linear scale with contours starting at 3σ increasing in steps of 1σ. Third column: polarization map over the column density (color scale) in logarithmic scale with contours starting at $\log_{10}(N_{\mathrm{HI+H_2}}[\mathrm{cm}^{-2}]) = 20$ increasing in steps of $\log_{10} N_{\mathrm{HI+H_2}}[\mathrm{cm}^{-2}] = 0.1$. Fourth column: polarization map over the dust temperature (color scale) in linear scale with contours starting at 20 K increasing in steps of 1 K.

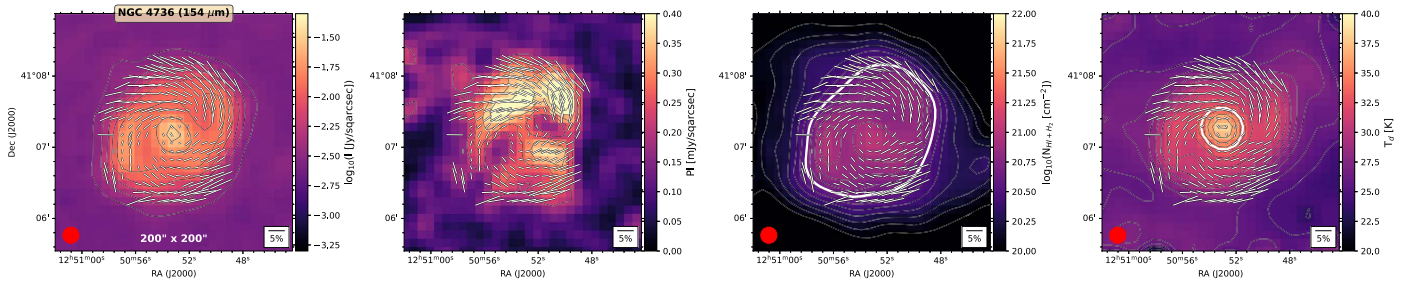

Figure 21. Object NGC 4736 at 154 μm (group 2). First column: total intensity (color scale) in logarithmic scale with contours starting at 8σ increasing in steps of $2^n\sigma$, with $n = 3, 3.5, 4, ...$ The polarization fraction measurements (white lines) with a legend of 5% (bottom right) are shown. The polarization fraction measurements with $\mathrm{PI}/\sigma_{\mathrm{PI}} \geqslant 3$, $P \leqslant 20\%$, and $I/\sigma_I \geqslant 20$ were selected. The beam size (red circle) is shown. Second column: polarization map over the PI (color scale) in linear scale with contours starting at 3σ increasing in steps of 1σ. Third column: polarization map over the column density (color scale) in logarithmic scale with contours starting at $\log_{10}(N_{\mathrm{HI+H_2}}[\mathrm{cm}^{-2}]) = 20$ increasing in steps of $\log_{10} N_{\mathrm{HI+H_2}}[\mathrm{cm}^{-2}] = 0.1$. Fourth column: polarization map over the dust temperature (color scale) in linear scale with contours starting at 20 K increasing in steps of 1 K. The white contours in the $N_{\mathrm{HI+H_2}}$ maps show the cutoff column density and dust temperature values shown in Table 6 and described in Sections 4.2 and 4.3, respectively.

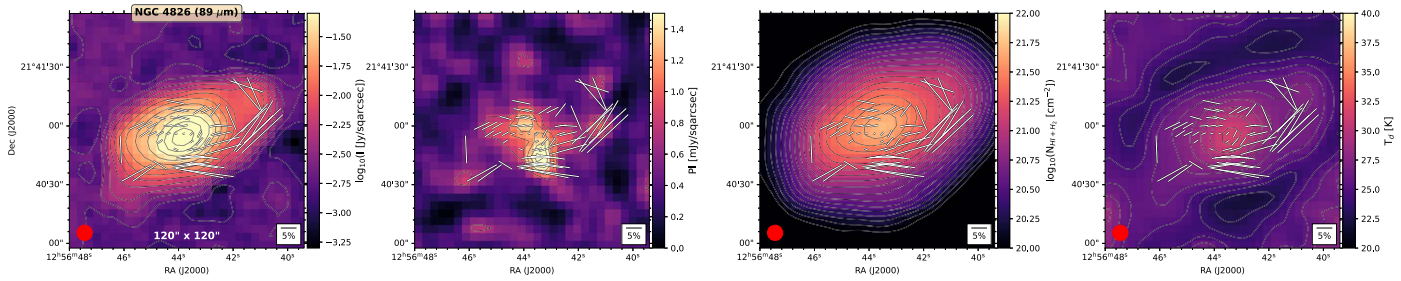

Figure 22. Object NGC 4826 at 154 μm (group 3). First column: total intensity (color scale) in logarithmic scale with contours starting at 8σ increasing in steps of $2^n\sigma$, with $n = 3, 3.5, 4, ...$ The polarization fraction measurements (white lines) with a legend of 5% (bottom right) are shown. The polarization fraction measurements with $\mathrm{PI}/\sigma_{\mathrm{PI}} \geqslant 3$, $P \leqslant 20\%$, and $I/\sigma_I \geqslant 20$ were selected. The beam size (red circle) is shown. Second column: polarization map over the PI (color scale) in linear scale with contours starting at 3σ increasing in steps of 1σ. Third column: polarization map over the column density (color scale) in logarithmic scale with contours starting at $\log_{10}(N_{\mathrm{HI+H_2}}[\mathrm{cm}^{-2}]) = 20$ increasing in steps of $\log_{10} N_{\mathrm{HI+H_2}}[\mathrm{cm}^{-2}] = 0.1$. Fourth column: polarization map over the dust temperature (color scale) in linear scale with contours starting at 20 K increasing in steps of 1 K.

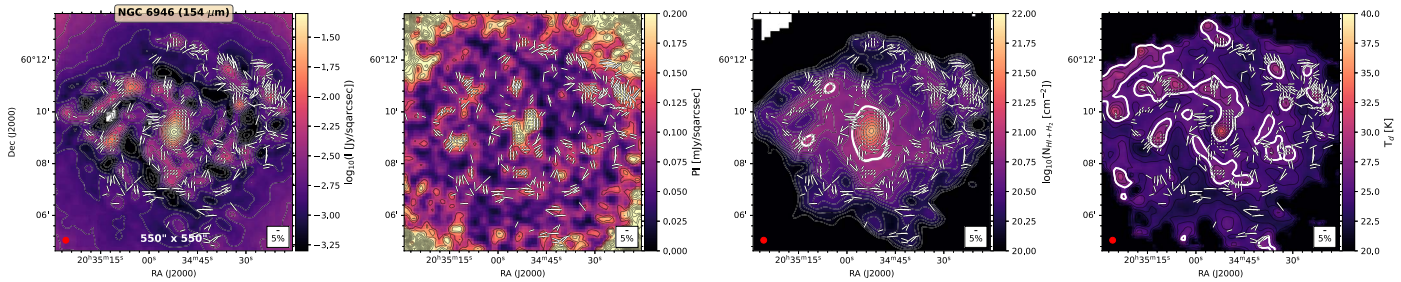

Figure 23. Object NGC 6946 at 154 μm (group 2). First column: total intensity (color scale) in logarithmic scale with contours starting at 8σ increasing in steps of $2^n\sigma$, with $n = 3, 3.5, 4, ...$ The polarization fraction measurements (white lines) with a legend of 5% (bottom right) are shown. The polarization fraction measurements with $\mathrm{PI}/\sigma_{\mathrm{PI}} \geqslant 3$, $P \leqslant 20\%$, and $I/\sigma_I \geqslant 20$ were selected. The beam size (red circle) is shown. Second column: polarization map over the PI (color scale) in linear scale with contours starting at 3σ increasing in steps of 1σ. Third column: polarization map over the column density (color scale) in logarithmic scale with contours starting at $\log_{10}(N_{\mathrm{HI+H_2}}[\mathrm{cm}^{-2}]) = 20$ increasing in steps of $\log_{10} N_{\mathrm{HI+H_2}}[\mathrm{cm}^{-2}] = 0.1$. Fourth column: polarization map over the dust temperature (color scale) in linear scale with contours starting at 20 K increasing in steps of 1 K. The white contours in the $N_{\mathrm{HI+H_2}}$ and T_{d} maps show the cutoff column density and dust temperature values shown in Table 6 and described in Sections 4.2 and 4.3, respectively.

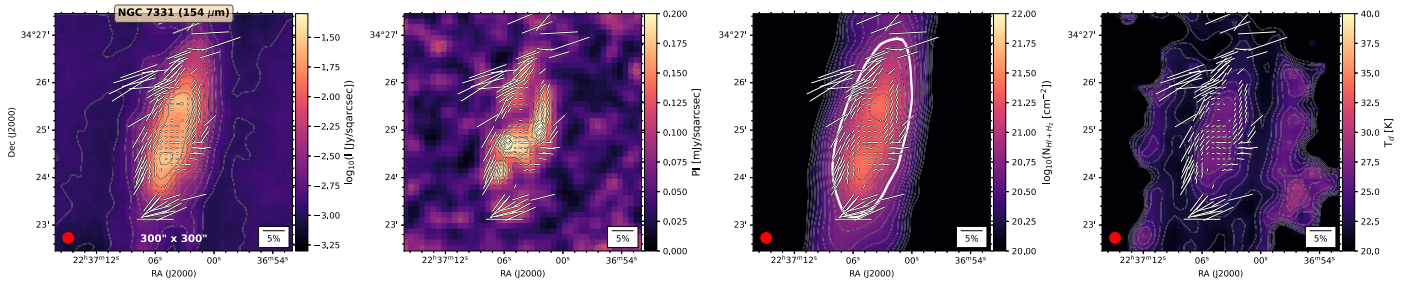

Figure 24. Object NGC 7331 at 154 μm (group 2). First column: total intensity (color scale) in logarithmic scale with contours starting at 8σ increasing in steps of $2^n\sigma$, with $n = 3, 3.5, 4, ...$ The polarization fraction measurements (white lines) with a legend of 5% (bottom right) are shown. The polarization fraction measurements with $\mathrm{PI}/\sigma_{\mathrm{PI}} \geqslant 3$, $P \leqslant 20\%$, and $I/\sigma_I \geqslant 45$ were selected. The beam size (red circle) is shown. Second column: polarization map over the PI (color scale) in linear scale with contours starting at 3σ increasing in steps of 1σ. Third column: polarization map over the column density (color scale) in logarithmic scale with contours starting at $\log_{10}(N_{\mathrm{HI+H_2}}[\mathrm{cm}^{-2}]) = 20$ increasing in steps of $\log_{10} N_{\mathrm{HI+H_2}}[\mathrm{cm}^{-2}] = 0.1$. Fourth column: polarization map over the dust temperature (color scale) in linear scale with contours starting at 20 K increasing in steps of 1 K. The white contours in the $N_{\mathrm{HI+H_2}}$ maps show the cutoff column density and dust temperature values shown in Table 6 and described in Sections 4.2 and 4.3, respectively.

measurements, respectively. The length of each polarization measurement is proportional to the polarization fraction, where a legend of 5% polarization fraction is shown in each panel. The third and fourth columns show the column density, $N_{\mathrm{HI+H_2}}$, and dust temperatures, T_{d}, within the same FOV and pixel scale as the total and polarized surface brightness observations.

To compute the temperature and column density maps, we registered and binned 70–160 μm Herschel observations taken with PACS to the pixel scales of the HAWC+ observations. This approach ensures that images at all wavelengths have the same pixel scale and array dimensions. Then, for every pixel, we fit an emissivity modified blackbody function,

$$B(\tau, T) = \frac{2hc}{\lambda^3} \frac{1 - e^{-\tau_{250}\left(\frac{\lambda}{\lambda_{250}}\right)^{\beta}}}{e^{\frac{hc}{\lambda kT}} - 1}, \tag{A1}$$

with a constant dust emissivity index $\beta = 1.5$. A dust emissivity index of 1.5 has typically been used (Hildebrand 1983; see also Dale & Helou 2002; Galametz et al. 2014). A value of $\beta = 1.60 \pm 0.38$ has been estimated to describe 65 local luminous IR galaxies (Casey 2012). We derived the molecular hydrogen optical depth as $N_{\mathrm{HI+H_2}} = \tau_{250}/(k_{250}\mu m_{\mathrm{H}})$, with a dust opacity $k_{250} = 0.1$ cm^2 g^{-1} at 250 μm and a mean molecular weight per hydrogen atom $\mu = 2.8$ (Hildebrand 1983). The τ_{250} is a free parameter estimated at a reference wavelength of 250 μm using Equation (A1).

Appendix B
Tables

This section contains the tabulated measurements from the main body of the article (Tables 5 and 6).

Table 5
Median and Integrated Polarization Fraction of Galaxies

Galaxy	Band (μm)	$\langle P^{\mathrm{hist}} \rangle$ (%)	$\langle P^{\mathrm{int}} \rangle$ (%)
(1)	(2)	(3)	(4)
Centaurus A	89	5.7 ± 5.3	1.7 ± 0.8
Circinus	53	5.1 ± 3.6	1.3 ± 0.8
	89	4.5 ± 4.8	1.6 ± 0.6
	214	11.4 ± 5.8	8.4 ± 0.8
M51	154	3.4 ± 4.5	1.4 ± 0.7
M82	53	2.5 ± 1.1	1.2 ± 0.2
	89	1.9 ± 1.6	1.0 ± 0.2
	154	1.6 ± 1.6	1.0 ± 0.3
	214	2.7 ± 1.9	1.4 ± 0.2
M83	154	3.9 ± 4.0	0.7 ± 0.3
NGC 253	89	1.5 ± 3.1	0.8 ± 0.6
	154	1.0 ± 0.7	0.4 ± 0.4
NGC 1068	53	3.4 ± 2.6	0.4 ± 0.4
	89	4.2 ± 2.8	0.9 ± 0.3
NGC 1097	89	2.6 ± 2.8	1.8 ± 0.3
	154	4.1 ± 2.7	1.2 ± 0.8
NGC 2146	53	2.0 ± 2.7	1.6 ± 0.6
	89	0.8 ± 1.5	0.5 ± 0.2
	154	1.2 ± 1.9	0.7 ± 0.3
	214	1.6 ± 1.5	1.8 ± 0.3
NGC 3627	154	3.3 ± 2.4	0.3 ± 0.3
NGC 4736	154	3.2 ± 1.7	0.9 ± 0.2
NGC 4826	89	5.3 ± 4.9	1.4 ± 0.5
NGC 6946	154	8.6 ± 4.8	0.7 ± 0.3
NGC 7331	154	1.6 ± 2.4	1.0 ± 0.2

Note: The columns are as follows: (1) galaxy name, (2) central wavelength of the band, (3) median polarization fraction based on individual measurements from Equation (1), and (4) median polarization fraction based on the integrated Stokes *IQU* of the full galaxy from Equation (2).

Table 6
Power-law Fitting Parameters of the $P - N_{\rm HI+H2}$ and $P - T_{\rm d}$ Relations

Object	Band	$P - N_{\rm HI+H2}$				$P - T_{\rm d}$			
		P_0 (%)	α_1	$\log_{10}(N^{\rm c}_{\rm HI+H2})$ ($\rm cm^{-2}$)	α_2	$P_0^{T_{\rm d}}$ (%)	$\alpha_1^{T_{\rm d}}$	$T^{\rm c}_{\rm d}$ (K)	$\alpha_2^{T_{\rm d}}$
(1)	(2)	(3)	(4)	(5)	(6)	(7)	(8)	(9)	(10)
Centaurus A	89	$1.5^{+0.3}_{-0.3}$	$-0.99^{+0.01}_{-0.01}$	⋯	⋯	$0.6^{+0.1}_{-0.1}$	$-11.32^{+0.68}_{-0.61}$	⋯	⋯
Circinus	53	$3.0^{+0.1}_{-0.1}$	$-0.81^{+0.01}_{-0.01}$	⋯	⋯	$1.2^{+0.5}_{-0.5}$	$-6.83^{+3.37}_{-3.13}$	⋯	⋯
	89	$3.3^{+0.2}_{-0.1}$	$-0.93^{+0.03}_{-0.03}$	⋯	⋯	$3.7^{+0.2}_{-0.2}$	$-7.49^{+1.38}_{-1.65}$	$28.5^{+0.5}_{-0.4}$	$-1.49^{+0.10}_{-0.10}$
	214	$2.4^{+0.3}_{-0.2}$	$-0.97^{+0.03}_{-0.03}$	$21.69^{+0.05}_{-0.05}$	$-0.34^{+0.16}_{-0.18}$	$2.9^{+0.3}_{-0.3}$	$-7.78^{+0.77}_{-0.65}$	$27.4^{+0.4}_{-0.4}$	$-1.36^{+0.43}_{-0.42}$
M51	154	$7.7^{+0.5}_{-0.5}$	$-0.28^{+0.21}_{-0.22}$	$20.62^{+0.02}_{-0.02}$	$-0.99^{+0.01}_{-0.02}$	$0.4^{+0.1}_{-0.1}$	$-11.78^{+0.22}_{-0.21}$	⋯	⋯
M82	53	$2.6^{+0.2}_{-0.1}$	$-0.86^{+0.16}_{-0.14}$	$22.04^{+0.05}_{-0.06}$	$-0.26^{+0.04}_{-0.03}$	$2.0^{+0.1}_{-0.1}$	$-7.24^{+1.28}_{-1.40}$	$37.6^{+0.4}_{-0.2}$	$-0.01^{+0.01}_{-0.01}$
	89	$2.3^{+0.2}_{-0.2}$	$-0.65^{+0.09}_{-0.10}$	$21.48^{+0.07}_{-0.10}$	$-0.35^{+0.01}_{-0.01}$	$1.0^{+0.1}_{-0.1}$	$-4.81^{+0.37}_{-0.94}$	$38.4^{+0.2}_{-0.8}$	$-0.00^{+0.01}_{-0.01}$
	154	$1.0^{+0.1}_{-0.1}$	$-0.99^{+0.01}_{-0.01}$	$21.30^{+0.01}_{-0.01}$	$-0.32^{+0.01}_{-0.01}$	$0.8^{+0.1}_{-0.1}$	$-5.74^{+0.20}_{-0.19}$	$34.9^{+0.1}_{-0.1}$	$-3.89^{+0.10}_{-0.10}$
	214	$0.6^{+0.1}_{-0.1}$	$-0.78^{+0.05}_{-0.05}$	$21.79^{+0.06}_{-0.07}$	$-0.13^{+0.07}_{-0.07}$	$0.5^{+0.1}_{-0.1}$	$-6.17^{+0.37}_{-0.34}$	$36.7^{+0.7}_{-0.7}$	$-0.44^{+0.44}_{-0.49}$
M83	154	$2.3^{+0.3}_{-0.3}$	$-0.96^{+0.05}_{-0.04}$	$21.09^{+0.06}_{-0.07}$	$-0.51^{+0.04}_{-0.04}$	$1.2^{+0.1}_{-0.1}$	$-4.35^{+0.26}_{-0.24}$	$33.0^{+0.5}_{-0.5}$	$-2.78^{+0.31}_{-0.22}$
NGC 253	89	$0.2^{+0.1}_{-0.1}$	$-1.00^{+0.01}_{-0.01}$	⋯	⋯	$3.0^{+0.1}_{-0.1}$	$-8.00^{+0.01}_{-0.01}$	$28.0^{+0.1}_{-0.1}$	$-3.00^{+0.01}_{-0.01}$
	154	$0.4^{+0.1}_{-0.1}$	$-0.43^{+0.13}_{-0.12}$	⋯	⋯	$0.5^{+0.1}_{-0.1}$	$-0.95^{+0.41}_{-0.43}$	⋯	⋯
NGC 1068	53	$4.0^{+0.1}_{-0.1}$	$-0.56^{+0.06}_{-0.11}$	⋯	⋯	$0.3^{+0.1}_{-0.1}$	$-11.08^{+0.89}_{-0.80}$	⋯	⋯
	89	$0.9^{+0.1}_{-0.1}$	$-1.00^{+0.01}_{-0.01}$	⋯	⋯	$0.9^{+0.1}_{-0.1}$	$-9.16^{+0.48}_{-0.45}$	$33.7^{+0.3}_{-0.3}$	$-1.16^{+0.69}_{-0.68}$
NGC 1097	89	$5.3^{+0.3}_{-0.7}$	$-0.37^{+0.13}_{-0.12}$	$21.33^{+0.04}_{-0.03}$	$-0.96^{+0.07}_{-0.04}$	$0.7^{+0.1}_{-0.1}$	$-4.87^{+0.34}_{-0.37}$	⋯	⋯
	154	$5.9^{+0.9}_{-0.1}$	$-0.45^{+0.06}_{-0.05}$	$21.28^{+0.03}_{-0.03}$	$-0.88^{+0.13}_{-0.12}$	$0.8^{+0.2}_{-0.2}$	$-4.85^{+0.77}_{-0.78}$	⋯	⋯
NGC 2146	53	$0.6^{+0.1}_{-0.1}$	$-0.93^{+0.09}_{-0.07}$	⋯	⋯	$0.6^{+0.1}_{-0.2}$	$-9.58^{+1.43}_{-1.48}$	⋯	⋯
	89	$0.3^{+0.1}_{-0.1}$	$-0.74^{+0.04}_{-0.04}$	⋯	⋯	$0.3^{+0.1}_{-0.1}$	$-5.11^{+0.61}_{-0.65}$	⋯	⋯
	154	$0.2^{+0.1}_{-0.1}$	$-0.99^{+0.02}_{-0.01}$	⋯	⋯	$0.1^{+0.1}_{-0.1}$	$-7.56^{+0.32}_{-0.30}$	⋯	⋯
	214	$0.3^{+0.1}_{-0.1}$	$-0.84^{+0.06}_{-0.06}$	⋯	⋯	$0.2^{+0.1}_{-0.1}$	$-6.13^{+0.43}_{-0.46}$	⋯	⋯
NGC 3627	154	$0.8^{+0.1}_{-0.1}$	$-0.97^{+0.03}_{-0.03}$	⋯	⋯	$1.2^{+0.2}_{-0.2}$	$-7.24^{+0.66}_{-0.63}$	⋯	⋯
NGC 4736	154	$4.4^{+0.2}_{-0.2}$	$-0.06^{+0.04}_{-0.04}$	$20.61^{+0.01}_{-0.01}$	$-0.98^{+0.03}_{-0.02}$	$2.0^{+0.4}_{-0.4}$	$-5.08^{+0.62}_{-0.61}$	⋯	⋯
NGC 4826	89	$1.8^{+0.2}_{-0.2}$	$-0.96^{+0.05}_{-0.04}$	⋯	⋯	$1.3^{+0.4}_{-0.4}$	$-11.21^{+1.04}_{-0.79}$	⋯	⋯
NGC 6946	154	$3.1^{+0.1}_{-0.1}$	$-0.49^{+0.01}_{-0.01}$	$20.91^{+0.01}_{-0.01}$	$-1.00^{+0.01}_{-0.01}$	$3.2^{+0.2}_{-0.2}$	$-11.60^{+0.42}_{-0.40}$	⋯	⋯
NGC 7331	154	$6.0^{+0.7}_{-0.3}$	$-0.41^{+0.13}_{-0.09}$	$20.81^{+0.04}_{-0.03}$	$-0.99^{+0.02}_{-0.01}$	$1.0^{+0.1}_{-0.1}$	$-8.60^{+0.72}_{-0.73}$	⋯	⋯

Note. The columns are as follows: (1) galaxy name, (2) central wavelength of the band, (3) scale factor, (4) power-law index before the cutoff column density $N^{\rm c}_{\rm HI+H2}$, (5) cutoff column density in units of $\rm cm^{-2}$ in logarithmic scale, (6) power-law index after the cutoff column density $N^{\rm c}_{\rm HI+H2}$, (7) scale factor, (8) power-law index before the cutoff dust temperature $T^{\rm c}_{\rm d}$, (9) cutoff dust temperature in units of K, and (10) power-law index after the cutoff dust temperature $T^{\rm c}_{\rm d}$.

Appendix C
Figures of the Polarization Fraction with Column Density and Dust Temperature

Figures 25–27 show the $P - N_{\rm HI+H_2}$ and $P - T_{\rm d}$ relations for all galaxies associated with groups 1, 2, and 3 described in Sections 4.2 and 4.3.

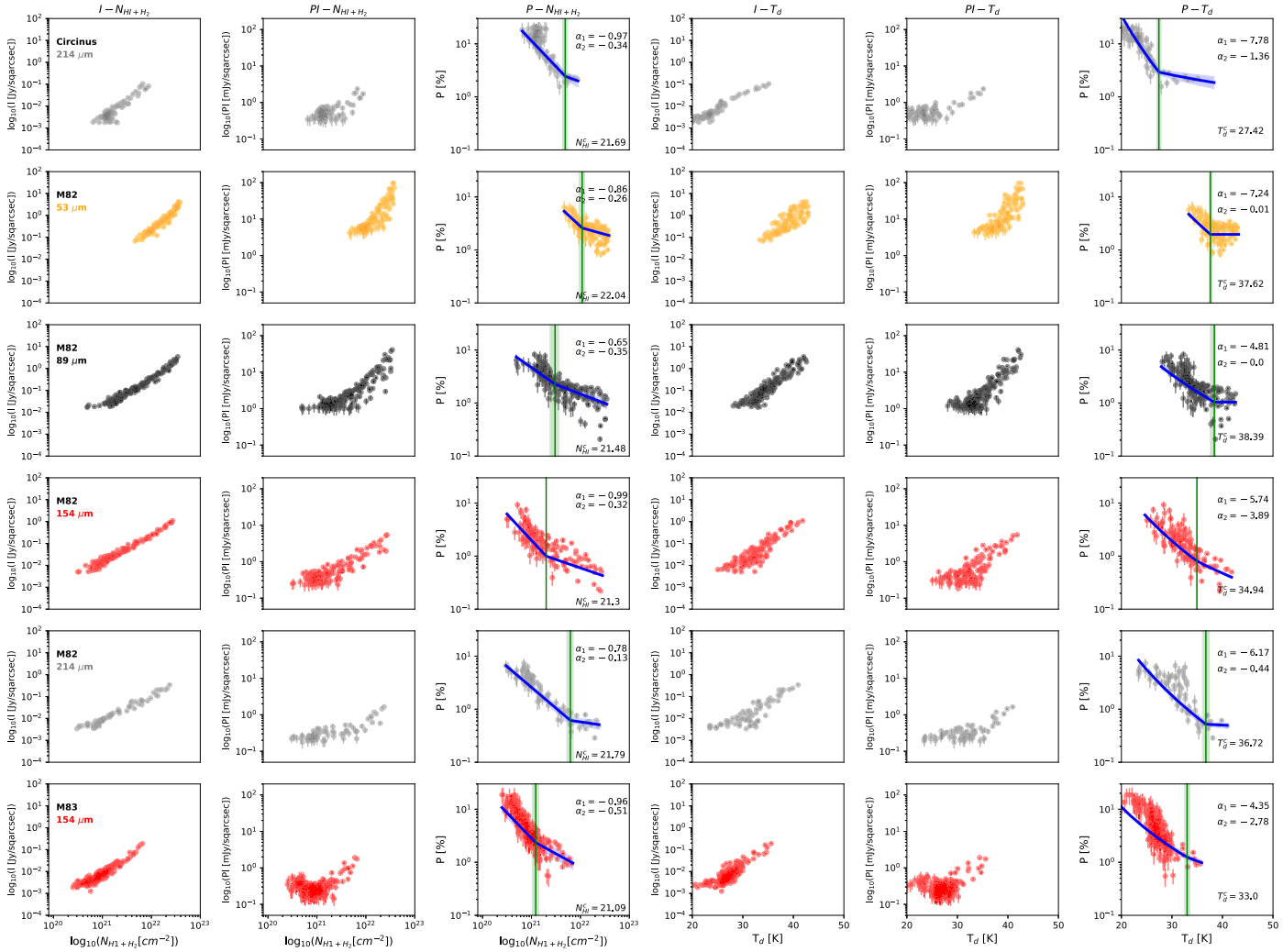

Figure 25. Polarization fraction vs. $N_{\rm HI+H_2}$ and $T_{\rm d}$ for the galaxies associated with group 1 shown in Figures 5 and 6. The same polarization fraction measurements shown in Figure 1 are used.

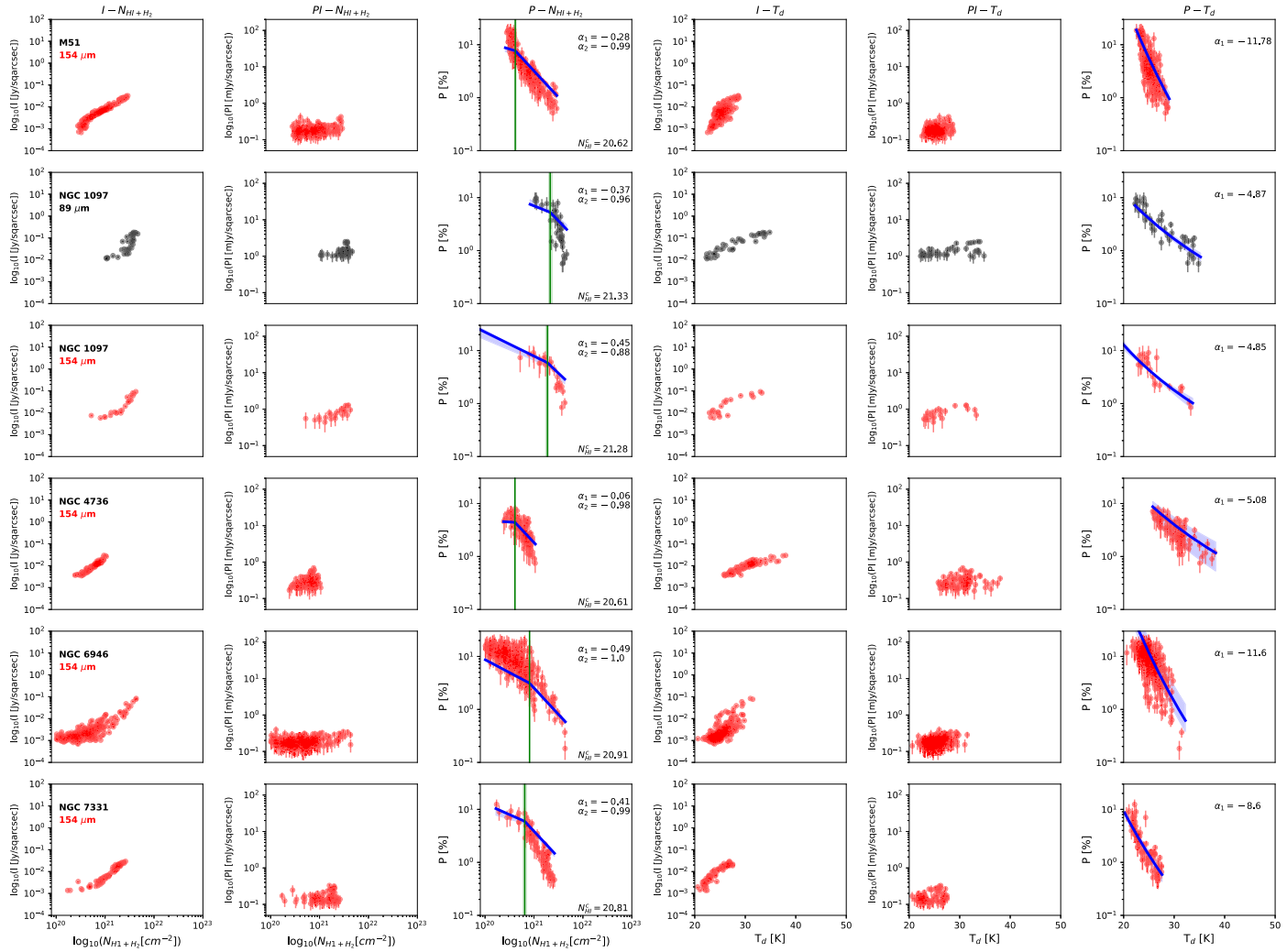

Figure 26. Polarization fraction vs. $N_{\rm HI+H_2}$ and $T_{\rm d}$ for the galaxies associated with group 2 shown in Figures 5 and 6. The same polarization fraction measurements shown in Figure 1 are used.

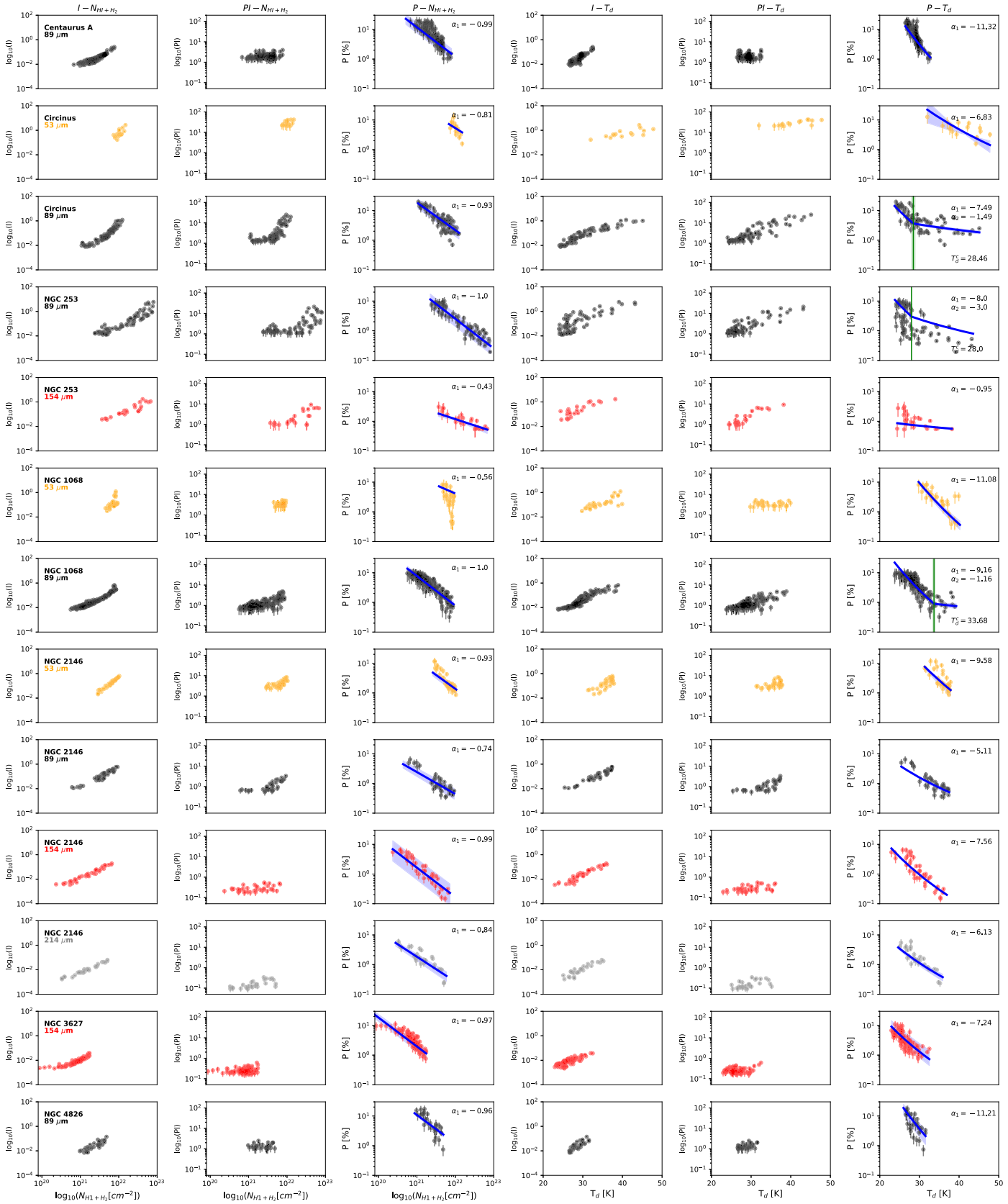

Figure 27. Polarization fraction versus $N_{\rm HI+H_2}$ and $T_{\rm d}$ for the galaxies associated with group 3 shown in Figures 5 and 6. The same polarization fraction measurements shown in Figure 1 are used.

Appendix D
Depolarization Effect due to the Effect of γ for Intermediate Inclinations

Section 5.3 shows that the polarization fraction may change across the galaxy disks for intermediate inclinations. The depolarization effect is caused by a change of the B-field orientation in the POS across the galaxy disk.

Taking the first approach from Section 5.3, we have that the polarization fraction varies as

$$P(\gamma, i) = \frac{p_0 \cos^2\gamma \cos^2 i}{1 - p_0(\frac{\cos^2\gamma}{2} - \frac{1}{3})}. \quad \text{(B1)}$$

Taking that the inclination is constant across the galaxy disk, the ratio between the polarization fractions across the disk due to a change in γ can be defined as

$$\Delta P_1 = \frac{P_{\gamma 1}(\gamma = 0)}{P_{\gamma 1}(\gamma')} = P_{\gamma 1,\max}\left[\frac{1}{p_o} - \left(\frac{\cos^2\gamma'}{2} - \frac{1}{3}\right)\right], \quad \text{(B2)}$$

where γ' is the B-field orientation with respect to the POS.

Using the second approach from Section 5.3, the change in polarization fraction is

$$\Delta P_2 = \frac{P_{\gamma 2}(\gamma = 0)}{P_{\gamma 2}(\gamma')} = \frac{1}{\cos^2\gamma'}. \quad \text{(B3)}$$

In Figure 28 we show the ratio of the polarization fraction (ΔP_1 and ΔP_2) as a function of $\Delta\gamma = \gamma' - \gamma = \gamma'$ ($\gamma = 0°$) for three values of the maximum polarization efficiency, $p_{\gamma 1,\max}$=1%, 4.3%, and 20%. As an example, for a galaxy with inclination $i = 40°$ and assuming that $\gamma \sim i$, the regions of the galaxy along the axis of rotation in the POS can suffer a depolarization of up to a factor of 1.2–5.1 within the maximum polarization ranges of of $p_{\gamma 1,\max}$=1%–20% for ΔP_1 and up to a factor of 1.7 for the pure geometrical approach (ΔP_2).

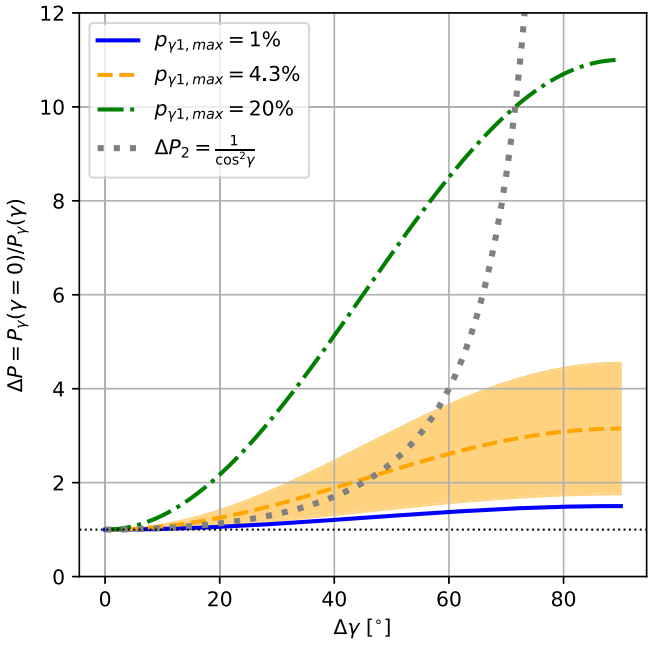

Figure 28. Variation of the polarization fraction with γ assuming a galaxy with constant inclination (Section 5.3). The ratio of the polarization fraction (ΔP_1; Equation (B2)) as a function of γ for three values of the maximum polarization fraction, $p_{\gamma 1,\max}$ = 1% (blue solid line), 4.3% (orange dashed line), and 20% (green dashed–dotted line), is shown. The median polarization of $\langle P^{\rm hist}\rangle = 4.3\% \pm 2.8\%$ for the galaxies with intermediate inclinations, 30°–60°, is displayed as the maximum polarization fraction in orange with the uncertainty shown as an orange shaded area. The ratio of the polarization fraction assuming a galaxy with constant inclination for ΔP_2 (gray dotted line; Equation (B3)) is shown.

ORCID iDs

Enrique Lopez-Rodriguez https://orcid.org/0000-0001-5357-6538
Sui Ann Mao https://orcid.org/0000-0001-8906-7866
Alejandro S. Borlaff https://orcid.org/0000-0003-3249-4431
Evangelia Ntormousi https://orcid.org/0000-0002-4324-0034
Konstantinos Tassis https://orcid.org/0000-0002-8831-2038
Daniel A. Dale https://orcid.org/0000-0002-5782-9093
Julia Roman-Duval https://orcid.org/0000-0001-6326-7069
Kandaswamy Subramanian https://orcid.org/0000-0002-4210-3513
Sergio Martin-Alvarez https://orcid.org/0000-0002-4059-9850
Susan E. Clark https://orcid.org/0000-0002-7633-3376
William T. Reach https://orcid.org/0000-0001-8362-4094
Ellen G. Zweibel https://orcid.org/0000-0003-4821-713X

References

Adebahr, B., Krause, M., Klein, U., Heald, G., & Dettmar, R. J. 2017, A&A, 608, A29
Adebahr, B., Krause, M., Klein, U., et al. 2013, A&A, 555, A23
Amram, P., Marcelin, M., Boulesteix, J., & Le Coarer, E. 1992, A&A, 266, 106
Andersson, B. G., Lazarian, A., & Vaillancourt, J. E. 2015, ARA&A, 53, 501
Arshakian, T. G., Beck, R., Krause, M., & Sokoloff, D. 2009, A&A, 494, 21
Astropy Collaboration, Robitaille, T. P., Tollerud, E. J., et al. 2013, A&A, 558, A33
Bambic, C. J., Morsony, B. J., & Reynolds, C. S. 2018, ApJ, 857, 84
Basu, A., Mao, S. A., Kepley, A. A., et al. 2017, MNRAS, 464, 1003
Battaner, E., Mediavilla, E., Guijarro, A., Arribas, S., & Florido, E. 2003, A&A, 401, 67
Beck, R. 2007, A&A, 470, 539
Beck, R. 2015, A&ARv, 24, 4
Beck, R., Chamandy, L., Elson, E., & Blackman, E. G. 2019, Galax, 8, 4
Beck, R., Ehle, M., Shoutenkov, V., Shukurov, A., & Sokoloff, D. 1999, Natur, 397, 324
Beck, R., Fletcher, A., Shukurov, A., et al. 2005, A&A, 444, 739
Beck, R., Klein, U., & Wielebinski, R. 1987, A&A, 186, 95
Beck, R., & Wielebinski, R. 2013, Planets, Stars and Stellar Systems. Volume 5: Galactic Structure and Stellar Populations, ed. T. D. Oswalt & G. Gilmore,, 641
Bernet, M. L., Miniati, F., Lilly, S. J., Kronberg, P. P., & Dessauges-Zavadsky, M. 2008, Natur, 454, 302
Berry, D. S. 1985, PhD thesis, Univ. Durham
Bertin, G., Lin, C. C., Lowe, S. A., & Thurstans, R. P. 1989, ApJ, 338, 104
Bertone, S., Vogt, C., & Enßlin, T. 2006, MNRAS, 370, 319
Birnboim, Y., Balberg, S., & Teyssier, R. 2015, MNRAS, 447, 3678
Bland-Hawthorn, J., Gallimore, J. F., Tacconi, L. J., et al. 1997, Ap&SS, 248, 9
Borlaff, A. S., Lopez-Rodriguez, E., Beck, R., et al. 2021, ApJ, 921, 128
Brandenburg, A., & Subramanian, K. 2005, PhR, 417, 1
Braun, R., Walterbos, R. A. M., Kennicutt, R. C. J., & Tacconi, L. J. 1994, ApJ, 420, 558
Brinks, E., Skillman, E. D., Terlevich, R. J., & Terlevich, E. 1997, Ap&SS, 248, 23
Caldwell, N., Rose, J. A., & Dendy, K. 1999, AJ, 117, 140
Casey, C. M. 2012, MNRAS, 425, 3094
Chandrasekhar, S., & Fermi, E. 1953, ApJ, 118, 113
Chen, C.-Y., King, P. K., Li, Z.-Y., Fissel, L. M., & Mazzei, R. R. 2019, MNRAS, 485, 3499
Chyży, K. T., & Beck, R. 2004, A&A, 417, 541
Chyży, K. T., Beck, R., Kohle, S., Klein, U., & Urbanik, M. 2000, A&A, 355, 128

Chyży, K. T., & Buta, R. J. 2008, ApJL, 677, L17
Chyży, K. T., Drzazga, R. T., Beck, R., et al. 2016, ApJ, 819, 39
Chyży, K. T., Knapik, J., Bomans, D. J., et al. 2003, A&A, 405, 513
Chyży, K. T., Sridhar, S. S., & Jurusik, W. 2017, A&A, 603, A121
Colombo, D., Meidt, S. E., Schinnerer, E., et al. 2014, ApJ, 784, 4
Crosthwaite, L. P., Turner, J. L., Buchholz, L., Ho, P. T. P., & Martin, R. N. 2002, AJ, 123, 1892
Daigle, O., Carignan, C., Amram, P., et al. 2006, MNRAS, 367, 469
Dale, D. A., & Helou, G. 2002, ApJ, 576, 159
Davis, L., & Greenstein, J. L. 1951, ApJ, 114, 206
Di Gennaro, G., van Weeren, R. J., Brunetti, G., et al. 2021, NatAs, 5, 268
Dicaire, I., Carignan, C., Amram, P., et al. 2008, MNRAS, 385, 553
Dowell, C. D., Cook, B. T., Harper, D. A., et al. 2010, Proc. SPIE, 7735, 77356H
Draine, B. T., & Fraisse, A. A. 2009, ApJ, 696, 1
Draine, B. T., & Weingartner, J. C. 1996, ApJ, 470, 551
Drzazga, R. T., Chyży, K. T., Jurusik, W., & Wiórkiewicz, K. 2011, A&A, 533, A22
Elbaz, D., & Cesarsky, C. J. 2003, Sci, 300, 270
Elmegreen, B. G., & Thomasson, M. 1993, A&A, 272, 37
Elmegreen, D. M., Sundin, M., Elmegreen, B., & Sundelius, B. 1991, A&A, 244, 52
Elmouttie, M., Krause, M., Haynes, R. F., & Jones, K. L. 1998, MNRAS, 300, 1119
Elvius, A. 1962, LowOB, 5, 281
Elvius, A., & Hall, J. S. 1964, LowOB, 6, 123
Emsellem, E., Fathi, K., Wozniak, H., et al. 2006, MNRAS, 365, 367
Falgarone, E., Zwaan, M. A., Godard, B., et al. 2017, Natur, 548, 430
Fendt, C., Beck, R., Lesch, H., & Neininger, N. 1996, A&A, 308, 713
Fendt, C., Beck, R., & Neininger, N. 1998, A&A, 335, 123
Ferrarese, L., Mould, J. R., Stetson, P. B., et al. 2007, ApJ, 654, 186
Fiege, J. D., & Pudritz, R. E. 2000, ApJ, 544, 830
Fletcher, A. 2010, in ASP Conf. Ser. 438, The Dynamic Interstellar Medium: A Celebration of the Canadian Galactic Plane Survey, ed. R. Kothes, T. L. Landecker, & A. G. Willis (San Francisco, CA: ASP), 197
Fletcher, A., Beck, R., Shukurov, A., Berkhuijsen, E. M., & Horellou, C. 2011, MNRAS, 412, 2396
French, K. D., Smercina, A., Rowlands, K., et al. 2022, arXiv:2204.07465
Frick, P., Stepanov, R., Beck, R., et al. 2016, A&A, 585, A21
Galametz, M., Albrecht, M., Kennicutt, R., et al. 2014, MNRAS, 439, 2542
Gent, F. A., Mac Low, M.-M., Käpylä, M. J., & Singh, N. K. 2021, ApJL, 910, L15
Gordon, M. S., Lopez-Rodriguez, E., Andersson, B. G., et al. 2018, arXiv:1811.03100
Hall, J. S., & Mikesell, A. H. 1949, AJ, 54, 187
Han, J. L., Beck, R., Ehle, M., Haynes, R. F., & Wielebinski, R. 1999, A&A, 348, 405
Harper, D. A., Runyan, M. C., Dowell, C. D., et al. 2018, JAI, 7, 1840008
Haverkorn, M., Brown, J. C., Gaensler, B. M., & McClure-Griffiths, N. M. 2008, ApJ, 680, 362
Heald, G., Braun, R., & Edmonds, R. 2009, A&A, 503, 409
Heavens, A., Panter, B., Jimenez, R., & Dunlop, J. 2004, Natur, 428, 625
Heesen, V., Beck, R., Krause, M., & Dettmar, R. J. 2011, A&A, 535, A79
Hennebelle, P., & Inutsuka, S.-i 2019, FrASS, 6, 5
Hildebrand, R. H. 1983, QJRAS, 24, 267
Hildebrand, R. H., Dotson, J. L., Dowell, C. D., Schleuning, D. A., & Vaillancourt, J. E. 1999, ApJ, 516, 834
Hiltner, W. A. 1949, ApJ, 109, 471
Hoang, T. 2021, ApJ, 907, 37
Hoang, T., & Lazarian, A. 2016, ApJ, 831, 159
Hsieh, P.-Y., Matsushita, S., Liu, G., et al. 2011, ApJ, 736, 129
Hughes, T. M., Baes, M., Fritz, J., et al. 2014, A&A, 565, A4
Hummel, E., Beck, R., & Dahlem, M. 1991, A&A, 248, 23
Hummel, E., Lesch, H., Wielebinski, R., & Schlickeiser, R. 1988, A&A, 197, L29
Hunter, J. D. 2007, CSE, 9, 90
Jaffe, T. R. 2019, Galax, 7, 52
Jones, K. L., Koribalski, B. S., Elmouttie, M., & Haynes, R. F. 1999, MNRAS, 302, 649
Jones, T. J. 2000, AJ, 120, 2920
Jones, T. J., Klebe, D., & Dickey, J. M. 1992, ApJ, 389, 602
Jones, T. J., & Whittet, D. C. B. 2015, Polarimetry of Stars and Planetary Systems (Cambridge: Cambridge Univ. Press), 147
Jones, T. J., Dowell, C. D., Lopez Rodriguez, E., et al. 2019, ApJL, 870, L9
Jones, T. J., Kim, J.-A., Dowell, C. D., et al. 2020, AJ, 160, 167
Karachentsev, I. D., Sharina, M. E., & Huchtmeier, W. K. 2000, A&A, 362, 544
Kennicutt, R. C. J., Armus, L., Bendo, G., et al. 2003, PASP, 115, 928
Kepley, A. A., Mühle, S., Everett, J., et al. 2010, ApJ, 712, 536
Kereš, D., Katz, N., Fardal, M., Davé, R., & Weinberg, D. H. 2009, MNRAS, 395, 160
King, D. J. 1986, MNRAS, 220, 485
King, P. K., Chen, C.-Y., Fissel, L. M., & Li, Z.-Y. 2019, MNRAS, 490, 2760
Kitchatinov, L. L., & Rüdiger, G. 2004, A&A, 424, 565
Klein, U., Beck, R., Buczilowski, U. R., & Wielebinski, R. 1982, A&A, 108, 176
Klein, U., Haynes, R. F., Wielebinski, R., & Meinert, D. 1993, A&A, 271, 402
Kotarba, H., Lesch, H., Dolag, K., et al. 2011, MNRAS, 415, 3189
Krasheninnikova, I., Shukurov, A., Ruzmaikin, A., & Sokolov, D. 1989, A&A, 213, 19
Krause, M., Irwin, J., Schmidt, P., et al. 2020, A&A, 639, A112
Kronberg, P. P., Lesch, H., & Hopp, U. 1999, ApJ, 511, 56
Kuno, N., Sato, N., Nakanishi, H., et al. 2007, PASJ, 59, 117
Lacki, B. C., & Beck, R. 2013, MNRAS, 430, 3171
Lacki, B. C., Thompson, T. A., & Quataert, E. 2010, ApJ, 717, 1
Lee, H. M., & Draine, B. T. 1985, ApJ, 290, 211
Leroy, A. K., Schinnerer, E., Hughes, A., et al. 2021, ApJS, 257, 43
Livingston, J. D., McClure-Griffiths, N. M., Mao, S. A., et al. 2022, MNRAS, 510, 260
Locatelli, N., Vazza, F., Bonafede, A., et al. 2021, A&A, 652, A80
Lopez-Rodriguez, E. 2021, NatAs, 5, 604
Lopez-Rodriguez, E., Antonucci, R., Chary, R.-R., & Kishimoto, M. 2018, ApJL, 861, L23
Lopez-Rodriguez, E., Guerra, J. A., Asgari-Targhi, M., & Schmelz, J. T. 2021a, ApJ, 914, 24
Lopez-Rodriguez, E., Beck, R., Clark, S. E., et al. 2021b, ApJ, 923, 150
Lopez-Rodriguez, E., Dowell, C. D., Jones, T. J., et al. 2020, ApJ, 888, 66
Lopez-Rodriguez, E., Clarke, M., Shenoy, S., et al. 2022, ApJ, 936, 65
Lucero, D. M., Carignan, C., Elson, E. C., et al. 2015, MNRAS, 450, 3935
Mao, S. A., Gaensler, B. M., Stanimirović, S., et al. 2008, ApJ, 688, 1029
Mao, S. A., McClure-Griffiths, N. M., Gaensler, B. M., et al. 2012, ApJ, 759, 25
Mao, S. A., Carilli, C., Gaensler, B. M., et al. 2017, NatAs, 1, 621
Martin-Alvarez, S., Devriendt, J., Slyz, A., et al. 2022, MNRAS, 513, 3326
Martin-Alvarez, S., Katz, H., Sijacki, D., Devriendt, J., & Slyz, A. 2021, MNRAS, 504, 2517
Martin-Alvarez, S., Devriendt, J., Slyz, A., & Teyssier, R. 2018, MNRAS, 479, 3343
Martin-Alvarez, S., Slyz, A., Devriendt, J., & Gómez-Guijarro, C. 2020, MNRAS, 495, 4475
Mayya, Y. D., Carrasco, L., & Luna, A. 2005, ApJL, 628, L33
McQuinn, K. B. W., Skillman, E. D., Dolphin, A. E., Berg, D., & Kennicutt, R. 2017, AJ, 154, 51
Michail, J. M., Ashton, P. C., Berthoud, M. G., et al. 2021, ApJ, 907, 46
Michikoshi, S., & Kokubo, E. 2016, ApJ, 821, 35
Mora-Partiarroyo, S. C., Krause, M., Basu, A., et al. 2019, A&A, 632, A11
Mouschovias, T. C., Tassis, K., & Kunz, M. W. 2006, ApJ, 646, 1043
Murphy, E. J. 2009, ApJ, 706, 482
Ntormousi, E. 2018, A&A, 619, L5
Ntormousi, E., Tassis, K., Del Sordo, F., Fragkoudi, F., & Pakmor, R. 2020, A&A, 641, A165
Pakmor, R., Marinacci, F., & Springel, V. 2014, ApJL, 783, L20
Pakmor, R., van de Voort, F., Bieri, R., et al. 2020, MNRAS, 498, 3125
Panopoulou, G. V., Hensley, B. S., Skalidis, R., Blinov, D., & Tassis, K. 2019, A&A, 624, L8
Patrikeev, I., Fletcher, A., Stepanov, R., et al. 2006, A&A, 458, 441
Pattle, K., Fissel, L., Tahani, M., Liu, T., & Ntormousi, E. 2022, arXiv:2203.11179
Pattle, K., Gear, W., Redman, M., Smith, M. W. L., & Greaves, J. 2021, MNRAS, 505, 684
Pavel, M. D., & Clemens, D. P. 2012, ApJL, 761, L28
Pearson, W. J., Wang, L., Alpaslan, M., et al. 2019, A&A, 631, A51
Pettitt, A. R., Tasker, E. J., Wadsley, J. W., Keller, B. W., & Benincasa, S. M. 2017, MNRAS, 468, 4189
Planck Collaboration, Ade, P. A. R., Aghanim, N., et al. 2015, A&A, 576, A104
Planck Collaboration, Aghanim, N., Alves, M. I. R., et al. 2016, A&A, 596, A105
Planesas, P., Scoville, N., & Myers, S. T. 1991, ApJ, 369, 364
Quillen, A. C., Neumayer, N., Oosterloo, T., & Espada, D. 2010, PASA, 27, 396

Radburn-Smith, D. J., de Jong, R. S., Seth, A. C., et al. 2011, ApJS, 195, 18
Rand, R. J., Kulkarni, S. R., & Hester, J. J. 1990, ApJL, 352, L1
Reach, W. T., Fadda, D., Rand, R. J., & Stacey, G. J. 2020, ApJ, 902, 28
Rieder, M., & Teyssier, R. 2016, MNRAS, 457, 1722
Robishaw, T., Quataert, E., & Heiles, C. 2008, ApJ, 680, 981
Robitaille, T., & Bressert, E. 2012, APLpy: Astronomical Plotting Library in Python, Astrophysics Source Code Library, ascl:1208.017
Ruzmaikin, A., Sokolov, D., & Shukurov, A. 1988, Natur, 336, 341
Ryu, D., Kang, H., Cho, J., & Das, S. 2008, Sci, 320, 909
Salvatier, J., Wiecki, T. V., & Fonnesbeck, C. 2016, PeerJ Comput. Sci., 2, e55
Samui, S., Subramanian, K., & Srianand, R. 2018, MNRAS, 476, 1680
Scarrott, S. M. 1996, QJRAS, 37, 297
Scarrott, S. M., Draper, P. W., Stockdale, D. P., & Wolstencroft, R. D. 1993, MNRAS, 264, L7
Scarrott, S. M., Foley, N. B., Gledhill, T. M., & Wolstencroft, R. D. 1996, MNRAS, 282, 252
Scarrott, S. M., Ward-Thompson, D., & Warren-Smith, R. F. 1987, MNRAS, 224, 299
Schleicher, D. R. G., & Beck, R. 2013, A&A, 556, A142
Schober, J., Schleicher, D. R. G., & Klessen, R. S. 2013, A&A, 560, A87
Schober, J., Schleicher, D. R. G., & Klessen, R. S. 2016, ApJ, 827, 109
Schweizer, F., Burns, C. R., Madore, B. F., et al. 2008, AJ, 136, 1482
Sellwood, J. A., & Carlberg, R. G. 1984, ApJ, 282, 61
Seth, A. C., Dalcanton, J. J., & de Jong, R. S. 2005, AJ, 130, 1574
Seymour, N., Dwelly, T., Moss, D., et al. 2008, MNRAS, 386, 1695
Shinn, J.-H., & Seon, K.-I. 2015, ApJ, 815, 133
Shu, F. H. 2016, ARA&A, 54, 667
Shukurov, A., & Subramanian, K. 2021, Astrophysical Magnetic Fields: From Galaxies to the Early Universe (Cambridge: Cambridge Univ. Press)
Sorai, K., Kuno, N., Muraoka, K., et al. 2019, PASJ, 71, S14
Steinwandel, U. P., Beck, M. C., Arth, A., et al. 2019, MNRAS, 483, 1008
Subramanian, K. 1998, MNRAS, 294, 718
Subramanian, K. 2019, Galax, 7, 47
Suess, K. A., Kriek, M., Bezanson, R., et al. 2022, ApJ, 926, 89
Sutter, J., & Fadda, D. 2022, ApJ, 926, 82
Tabatabaei, F. S., Martinsson, T. P. K., Knapen, J. H., et al. 2016, ApJL, 818, L10
Tabatabaei, F. S., Minguez, P., Prieto, M. A., & Fernández-Ontiveros, J. A. 2018, NatAs, 2, 83
Tabatabaei, F. S., Schinnerer, E., Murphy, E. J., et al. 2013, A&A, 552, A19
Tacconi, L. J., Genzel, R., Neri, R., et al. 2010, Natur, 463, 781
Tarchi, A., Greve, A., Peck, A. B., et al. 2004, MNRAS, 351, 339
Thompson, T. A., Quataert, E., Waxman, E., Murray, N., & Martin, C. L. 2006, ApJ, 645, 186
Toomre, A., & Toomre, J. 1972, ApJ, 178, 623
Tully, R. B. 1988, Nearby Galaxies Catalog (Cambridge: Cambridge Univ. Press)
Tully, R. B., Rizzi, L., Shaya, E. J., et al. 2009, AJ, 138, 323
Tully, R. B., Courtois, H. M., Dolphin, A. E., et al. 2013, AJ, 146, 86
Vacca, W. D., Hamilton, R. T., Savage, M., et al. 2015, ApJ, 804, 66
Vaillancourt, J. E., Chuss, D. T., Crutcher, R. M., et al. 2007, Proc. SPIE, 6678, 66780D
van de Voort, F., Bieri, R., Pakmor, R., et al. 2021, MNRAS, 501, 4888
Van Eck, C. L., Brown, J. C., Shukurov, A., & Fletcher, A. 2015, ApJ, 799, 35
Vandenbroucke, B., Baes, M., Camps, P., et al. 2021, A&A, 653, A34
Vazza, F., Brüggen, M., Gheller, C., & Wang, P. 2014, MNRAS, 445, 3706
Vazza, F., Brunetti, G., Brüggen, M., & Bonafede, A. 2018, MNRAS, 474, 1672
Verstappen, J., Fritz, J., Baes, M., et al. 2013, A&A, 556, A54
Vollmer, B., Soida, M., Beck, R., et al. 2007, A&A, 464, L37
Walter, F., Brinks, E., de Blok, W. J. G., et al. 2008, AJ, 136, 2563
Wang, P., & Abel, T. 2009, ApJ, 696, 96
Whittingham, J., Sparre, M., Pfrommer, C., & Pakmor, R. 2021, MNRAS, 506, 229
Widrow, L. M. 2002, RvMP, 74, 775
Wiegert, T., Irwin, J., Miskolczi, A., et al. 2015, AJ, 150, 81
Wild, V., Taj Aldeen, L., Carnall, A., et al. 2020, MNRAS, 494, 529
Willick, J. A., Courteau, S., Faber, S. M., et al. 1997, ApJS, 109, 333
Zeldovich, Y. B., Ruzmaikin, A. A., & Sokoloff, D. D. 1990, The Almighty Chance (Singapore: World Scientific)